Optical Forces from Periodic Adiabatic Rapid Passage Sequences on Metastable Helium Atoms

A Dissertation Presented

by

Daniel Thomas Stack

to

The Graduate School

in Partial Fulfillment of the Requirements

for the Degree of

Doctor of Philosophy

in

Physics

Stony Brook University

August 2012

Stony Brook University

The Graduate School

Daniel Thomas Stack

We, the dissertation committee for the above candidate for the Doctor of Philosophy degree, hereby recommend acceptance of this dissertation.

Harold Metcalf – Dissertation Advisor
Distinguished Teaching Professor, Department of Physics and Astronomy

Stanimir Metchev – Chairperson of Defense
Assistant Professor, Department of Physics and Astronomy

Jacobus Verbaarschot
Professor, Department of Physics and Astronomy

Sean J. Bentley
Associate Professor, Department of Physics
Adelphi University

This dissertation is accepted by the Graduate School.

Charles Taber
Interim Dean of the Graduate School

Abstract of the Dissertation

Optical Forces from Periodic Adiabatic Rapid Passage Sequences on Metastable Helium Atoms

by

Daniel Thomas Stack

Doctor of Philosophy

in

Physics

Stony Brook University

2012

Over the past 30 years, optical manipulation of neutral atoms has been primarily performed with a monochromatic laser beam. The simplest tool for the control of atomic motion is the radiative force exerted by a monochromatic laser on a two-level atom. The radiative force arises from absorption followed by spontaneous emission, and its magnitude is limited by the atom's excited state lifetime. The coherent momentum exchanges between light fields and atoms can be exploited to produce long-range optical forces much greater than the radiative force through the use of absorption-stimulated emission processes.

Adiabatic Rapid Passage (ARP) is a long-existing method to invert the population of a two-level nuclear spin system. Its extension to the optical domain

necessitates a frequency chirped light pulse to interact with a two-level atom via the dipole interaction. I will first present a numerical study of the properties of optical forces on moving atoms derived from purely stimulated processes produced by multiple ARP sequences. This will be followed by experimental observations of long-range ARP forces much larger than the radiative force in metastable helium. Sequences of properly timed laser pulses may be used for rapid deceleration of neutral atomic (or molecular) beams.

For my family and friends

Contents

List of Tables

List of Figures

Chapter 1

Introduction

The field of laser cooling and trapping has progressed tremendously since its inception more than 30 years ago [1–3]. Laser cooling and trapping refer to the experimental techniques that use the force exerted by laser light for the purposes of slowing and manipulation of atomic motion. The original motivation for laser cooling and trapping was to improve precision measurements of trapped ions for high resolution spectroscopy and atomic clocks [1, 4]. These measurements required means to suppress Doppler effects associated with ion motion.

Around this time it was also suggested that the same principles could be applied to neutral atoms [2]. The first observation of the laser cooling of neutral atoms was made in 1981 [5]. In the early days of atom trapping neutral atoms had to be cooled before they were captured. From there, improvements in the experimental techniques of laser cooling, magnetic trapping, and evaporative cooling led to the first observation of Bose-Einstein Condensation (BEC) in a dilute atomic gas in 1995 [6, 7]. Adiabatic rapid passage could be an additional tool to those interested in the slowing of atomic beams. Cold atomic gases have provided a new venue for the study of nonlinear optical effects, atomic collisions, and

basic quantum mechanical phenomena.

The magnitude of traditional optical forces used for laser cooling and slowing are fundamentally limited by the inherent properties of the atom and fundamental constants. This is only true for optical forces that rely on spontaneous emission to return an atom to its ground state. Much greater forces can be achieved with use of absorption and stimulated emission. Very large optical forces have been demonstrated for the bichromatic [8] and adiabatic rapid passage (ARP) force [9]. It is also very important to consider how the optical force depends on the atomic velocity for the purposes of slowing and cooling an atomic beam. Again, the utility of traditional optical forces are very much limited by the properties of the atom in question. It has been suggested that the ARP force may be effective over a much larger velocity range than traditional optical forces [10]. The properties of the ARP force, especially its velocity dependence, are the subject of this thesis. The ARP force requires a sequence of optical pulses, whose frequency is swept through an atomic resonance. This thesis will motivate why the ARP force is important and report results of an experimental realization of this strong, long-range force.

In this chapter I will give a brief introduction to the treatment of the interactions of light with neutral atoms, as well as traditional optical forces and the bichromatic force. Chapter 2 delves into the theoretical description of ARP and numerical calculations. Numerical simulations of the ARP force on atomic ensembles is the subject of Chapter 3. This is followed by Chapters 4 and 5, which describe the experimental setup to measure the velocity dependence of ARP. Chapter 6 will show the results of these experiments.

1.1 Two-Level Atom

The fundamental picture most commonly used in describing optical forces on neutral atoms is the two-level atom moving in a monochromatic light field. The following are the necessary tools to describe the optical forces to be discussed later in this chapter as well as the ARP force to be described in Chapter 2. The choice of variables and derivation of the Optical Bloch Equations (OBE's) closely follows Ref. [11] with certain choices motivated by Ref. [12].

1.1.1 Schrödinger Equation and Rabi-Oscillations

The time evolution of a two level atom (denoted $|g\rangle$, and $|e\rangle$ for ground and excited state) in the presence of a monochromatic light field is governed by the time-dependent Schrödinger equation

$$\imath\hbar\frac{\partial\psi}{\partial t} = H\psi \tag{1.1}$$

When the spatial extent of the atom is much smaller than the wavelength of an applied field, one can treat the field as spatially constant $\mathbf{E}(\mathbf{r},t) \rightarrow \mathbf{E}(t)$. In this electric dipole approximation an external electromagnetic field interacts with an electron via the time dependent potential

$$V(\mathbf{r},t) = -e\mathbf{r}\cdot\mathbf{E}(t) \tag{1.2}$$

where $\mathbf{r}$ is the relative electron-nuclear distance and the electric field $\mathbf{E}$ is a monochromatic plane wave of the form

$$\mathbf{E}(t) = \frac{1}{2}\hat{\boldsymbol{\epsilon}}E_0 e^{-i\omega_l t} + c.c. \tag{1.3}$$

where $\hat{\boldsymbol{\epsilon}}$ refers to the polarization of the field and ω_l is the angular frequency of the wave.

In the limit of a two level system ($\psi = a_g\phi_g + a_e\phi_e$ with $|a_g|^2 + |a_e|^2 = 1$) it can be shown

that the Schrödinger equation (1.1) reduces to

$$\imath\hbar\dot{a}_g(t) = E_g a_g(t) + V a_e(t) \tag{1.4a}$$

$$\imath\hbar\dot{a}_e(t) = E_e a_e(t) + V^* a_g(t) \tag{1.4b}$$

where E_n is the energy and a_n is the complex amplitude associated with the atomic state wavefunction ϕ_n. This approximation is valid when there is a negligible probability of the atom being in any state other than ϕ_g or ϕ_e.

At this point is convenient to define

$$\omega_a = \frac{E_e - E_g}{\hbar} \tag{1.5}$$

and

$$\Omega = \frac{-eE_0}{\hbar}\hat{\boldsymbol{\epsilon}} \cdot \langle \phi_g | \mathbf{r} | \phi_e \rangle \tag{1.6}$$

as the atomic transition frequency, and the complex, resonant Rabi frequency respectively. We may also set the zero-point energy of the system to E_g and perform the Rotating Frame Transformation by substituting

$$a_g(t) = c_g(t) \tag{1.7a}$$

$$a_e(t) = c_e(t) e^{-\imath\omega_a t} \tag{1.7b}$$

This particular transformation at ω_a leads to the interaction picture.

Neglecting the rapidly oscillating terms (Rotating Wave Approximation) and substituting

Eq. 1.5, 1.6,and 1.7 into Eq. 1.4 leads to

$$\imath\dot{c}_g = c_e(t)\frac{\Omega}{2} \tag{1.8a}$$

$$\imath\dot{c}_e = c_g(t)\frac{\Omega^*}{2} - c_e(\omega_l - \omega_a) \tag{1.8b}$$

The solutions to Eq. 1.8 are found to be

$$c_g(t) = \left(\cos\frac{\Omega' t}{2} + i\frac{\delta}{\Omega'}\sin\frac{\Omega' t}{2}\right)e^{\imath\delta t/2} \tag{1.9a}$$

$$c_e(t) = \left(i\frac{\Omega}{\Omega'}\sin\frac{\Omega' t}{2}\right)e^{\imath\delta t/2} \tag{1.9b}$$

where we have defined the laser detuning as $\delta = \omega_l - \omega_a$ and introduced the generalized Rabi frequency $\Omega' \equiv (\Omega^2 + \delta^2)^{1/2}$. The corresponding evolution of the state populations, $\rho_{gg}(t) = |a_g(t)|^2$ and $\rho_{ee}(t) = |a_e(t)|^2$ are

$$\rho_{gg}(t) = \frac{1}{2}\left[1 + \left(\frac{\delta}{\Omega'}\right)^2\right] + \frac{1}{2}\left(\frac{\Omega}{\Omega'}\right)^2\cos\Omega' t \tag{1.10a}$$

$$\rho_{ee}(t) = \frac{1}{2}\left(\frac{\Omega}{\Omega'}\right)^2[1 - \cos\Omega' t] \tag{1.10b}$$

It is clear from these equations that the excited state population oscillates at an angular frequency of Ω' with an amplitude of $(\Omega/\Omega')^2$. According to Eq. 1.10 it is not possible to achieve complete population inversion with a nonzero, fixed laser detuning. Fig. 1.1 shows how the population of the excited state varies in time, and with choice of Ω and δ, according to Eq. 1.10. To tackle more complex light fields and spontaneous emission it is useful to introduce a new approach that is discussed in the following section.

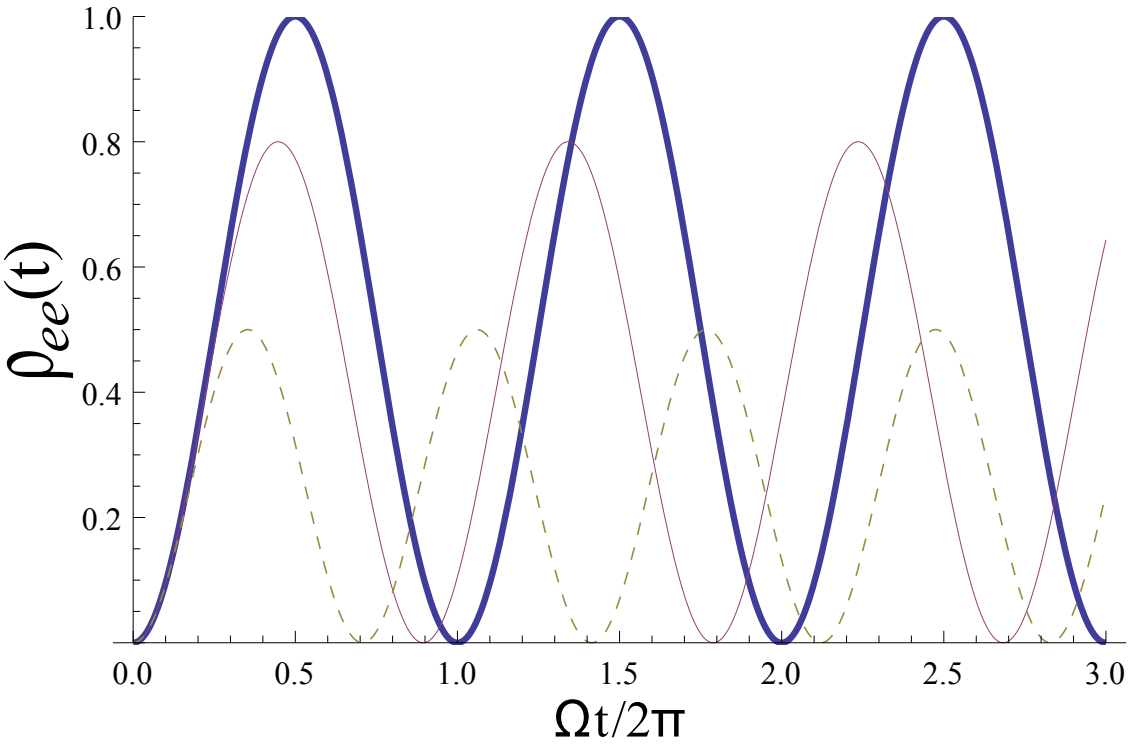

Figure 1.1: Oscillations of the excited state population for fixed Ω and varying δ. The thick, thin, and dashed lines correspond to $\delta = 0$, $\Omega/2$, and Ω respectively. The excited state population oscillates at an angular frequency of Ω' with an amplitude of $(\Omega/\Omega')^2$.

1.1.2 Optical Bloch Equations

The density matrix is a powerful formalism that has many distinct advantages to the wavefunction approach summarized in the previous subsection. It enables the treatment of states with partial coherence, important when dealing with spontaneous emission, and it provides a more direct connection with physical quantities.

A usual treatment of the density matrix, ρ, begins by relating it to the complex amplitudes, c_g and c_e, defined in Sec. 1.1.1

$$\rho = |\psi\rangle\langle\psi| = \begin{pmatrix} |c_g|^2 & c_g c_e^* \\ c_e c_g^* & |c_e|^2 \end{pmatrix} \tag{1.11}$$

The diagonal elements represent the atomic state populations while the off-diagonal elements represent the "coherences" of the interaction.

Repeated use of Eq. 1.8 can be used to derive the time dependence of the density matrix elements with the relations defined in Eq. 1.11. After a convenient change of variables

$$u = \quad \rho_{eg} + \rho_{ge} \tag{1.12a}$$

$$v = \quad \imath\,(\rho_{ge} - \rho_{eg}) \tag{1.12b}$$

$$w = \quad \rho_{ee} - \rho_{gg} \tag{1.12c}$$

one is left with the Optical Bloch Equations (OBE's)

$$\dot{u} = \Omega_{\mathrm{i}} w - \delta v \tag{1.13a}$$

$$\dot{v} = -\Omega_{\mathrm{r}} w + \delta u \tag{1.13b}$$

$$\dot{w} = \Omega_{\mathrm{r}} v - \Omega_{\mathrm{i}} u \tag{1.13c}$$

where $\Omega_{r,i}$ refer to the real and imaginary parts respectively of the Rabi frequency defined in Eq. 1.6.

The evolution of the atomic system can be visualized on a unit sphere, the Bloch sphere. The Bloch vector, defined as $\mathbf{R} = [u, v, w]$, is confined to the surface of the Bloch sphere by conservation of atomic probability, $|c_e|^2 + |c_g|^2 = 1$ (see Fig. 1.2). The south pole of the Bloch sphere represents the ground state of the atom, the north pole corresponds to the excited state. All other points on the sphere represent various superposition states. It is a versatile tool and very useful as a geometrical representation of the Optical Bloch Equations.

The Optical Bloch Equations still require some modification to better represent the true dynamics of a two level system. In most problems relaxation processes such as collisions and spontaneous emission are present. Collisions are unlikely in the experiments described in this dissertation and as such will be neglected, but spontaneous emission can be thought of as a special type of inelastic collision where the atom may change internal energy states. These "collisions" also have the effect of dephasing or decreasing the coherence of the interaction. Proper treatment of spontaneous emission [14] leads to the new equations

$$\dot{u} = \Omega_i w - \delta v - (\gamma/2)u \tag{1.14a}$$

$$\dot{v} = -\Omega_r w + \delta u - (\gamma/2)v \tag{1.14b}$$

$$\dot{w} = \Omega_r v - \Omega_i u - \gamma(w + 1) \tag{1.14c}$$

where γ is the spontaneous emission rate for the excited state $|e\rangle$ of the two-level atom.

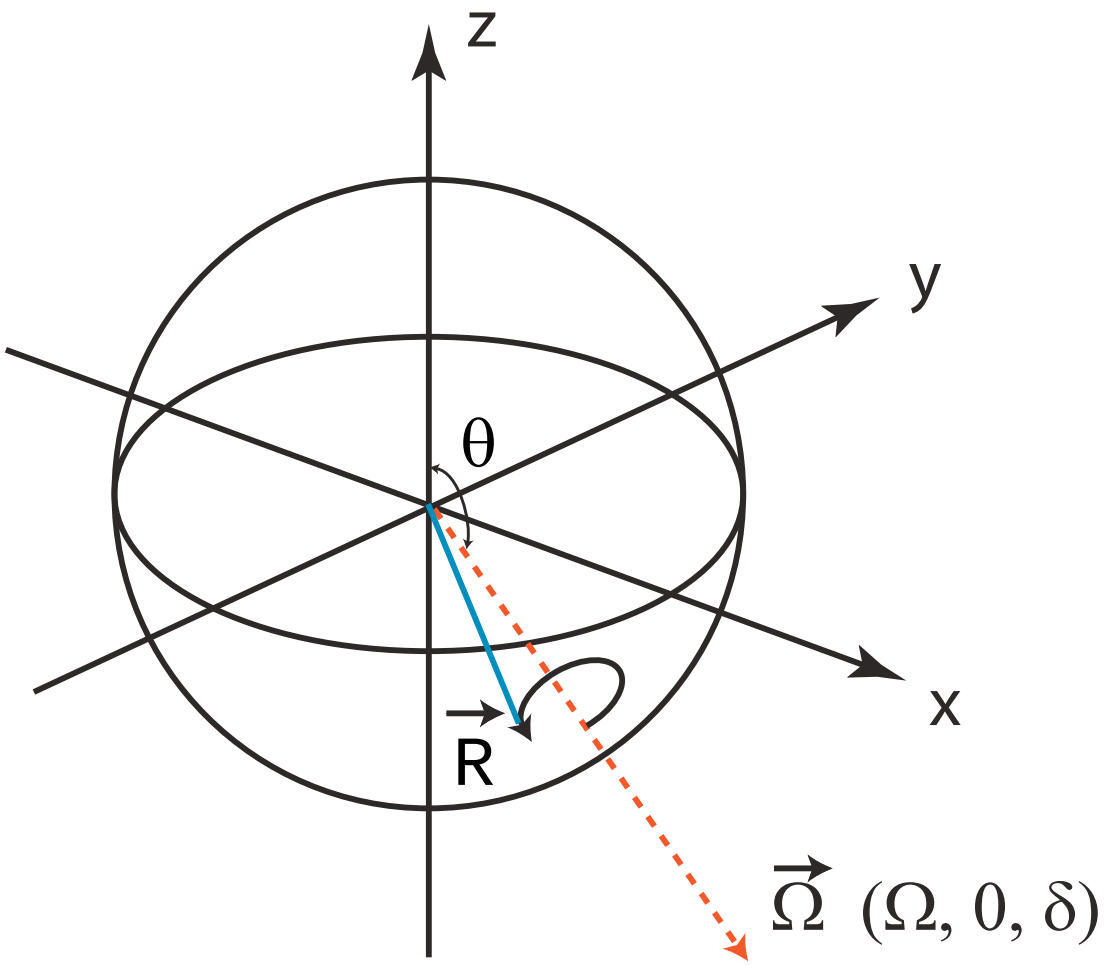

Figure 1.2: Projections of the Bloch and torque Vectors on the Bloch sphere. The solid line represents the Bloch vector **R** precessing about the torque vector **Ω**, represented by the dashed line. Taken from [13]

1.2 Optical Forces on Atoms

The notion of optical forces, derived from linear momentum conservation during atomic absorption of light, dates back to the 19^{th} century. When an atom of mass M absorbs light, the light's energy $\hbar\omega_\ell$ goes mostly into the excitation of the atom, its angular momentum $\hbar$ goes into the orbital motion of the electrons, but its linear momentum $\hbar\omega_\ell/c \equiv \hbar k$ can go only into the overall translational motion of the atom. The atomic velocity changes by $\hbar k/M \sim$ few cm/s. The magnitude of the resulting force is limited by how quickly this momentum exchange can be repeated and thus by the rate of the atom's return to the ground state. Many sophisticated schemes have been developed using the special properties of the atom-light interaction. To begin with, we consider the simplest optical force, the radiative force.

1.2.1 Radiative Force on Stationary Atoms

The radiative force is the response of an atom interacting with a monochromatic light field [12]. The momentum transfer via absorption is always in the direction of the laser beam propagation. The decay of an atom from the excited state to the ground state via spontaneous emission of a photon results in a force that is random in direction, so the force from decay averages to zero over many cycles. This results in a net force from this process each time the atom absorbs and then spontaneously emits a photon. A single absorption and spontaneous emission event is illustrated in Fig. 1.3. Over very many cycles there will be a net force in the direction of laser propagation.

The net force from this process is proportional to the momentum absorbed from the light

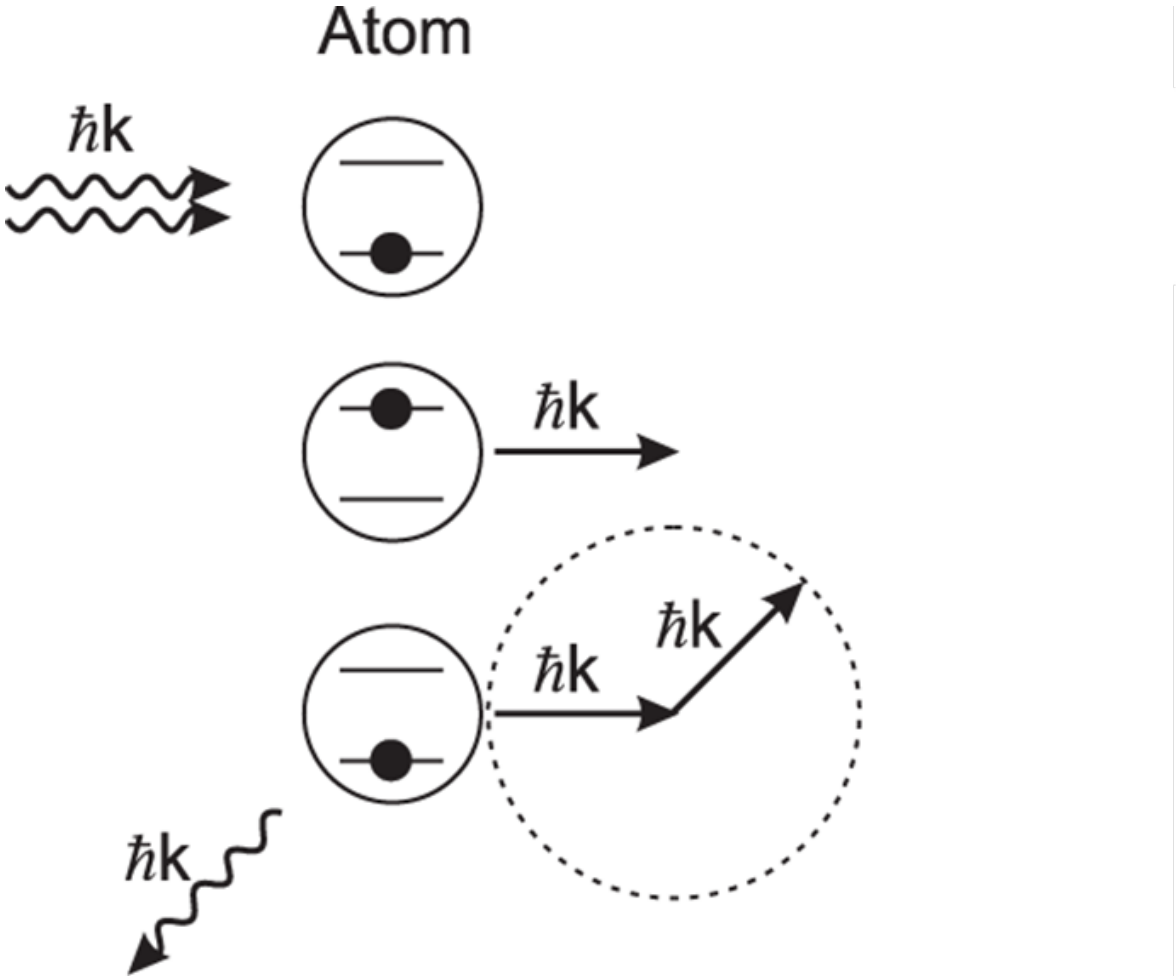

Figure 1.3: Cycle that produces the radiative force. Light is absorbed by an atom and consequently receives a momentum kick in the direction of the light propagation. After some time, the atom may spontaneously emit light in a random direction. The associated momentum transfer from spontaneous emission averages to zero over many cycles. This leads to a net momentum transfer in the direction of light propagation.

field and the scattering rate of the process

$$\vec{F} = \gamma_p \hbar \mathbf{k} \tag{1.15}$$

where $\gamma_p = \gamma \rho_{ee}$ is the scattering rate, consisting of the decay rate γ and time average population probability of the excited state

$$\gamma_p = \frac{s_0 \gamma/2}{1 + s_0 + (2\delta/\gamma)^2} \tag{1.16}$$

Here s_0 is ratio of the laser field intensity to the saturation intensity defined by

$$s_0 \equiv 2\frac{|\Omega^2|}{\gamma^2} = \frac{I}{I_S} \tag{1.17}$$

with $I_S \equiv \pi hc/(3\lambda^3\tau)$ (λ and τ are the wavelength and lifetime of the atomic transition respectively). Since the two-level atom in a monochromatic light field can only stay at most half the time in the excited state, the radiative force saturates at $\hbar k\gamma/2$. This can be seen in Eq. 1.16, for the case of $\delta = 0$ and $s_0 \gg 1$ or when $s_0 \gg 2\delta/\gamma,\ 1$.

1.2.2 Radiative Force on Moving Atoms

To cool and trap atoms, it is necessary to consider the consequences of atomic motion. Atoms moving with velocity $\mathbf{v}$ in the laboratory frame see a Doppler shift. The Doppler shift refers to the frequency shift of the light field seen by the moving atom $\omega_D = -\mathbf{k} \cdot \mathbf{v}$. This results in a modification of the radiative force on moving atoms given by

$$\mathbf{F}_{rad} = \hbar \mathbf{k} \frac{s_0 \gamma/2}{1 + s_0 + \Big(2\big(\delta - \mathbf{k} \cdot \mathbf{v}\big)/\gamma\Big)^2} \tag{1.18}$$

For moving atoms δ has been replaced by an effective detuning, $\delta - \mathbf{k} \cdot \mathbf{v}$. This force is maximum for zero-velocity atoms and on-resonance light. For off-resonant light, the force is maximum for atoms moving with the velocity $\mathbf{v} = \delta\mathbf{k}/k^2$.

It can be seen from Eq. 1.18 that the radiative force opposes atomic motion when the incident light travels opposite to the atomic velocity. The radiative force is a very useful tool for the slowing of atomic beams. However, as the atomic beam slows, the resonance condition changes due to the Doppler effect. The Zeeman shift can be used to compensate for this effect and may be done with a spatially varying magnetic field applied along the atomic beam path [15]. The Zeeman shift compensates for the Doppler effect and keeps the laser on resonance with the atomic beam until the beam is slowed sufficiently. Other methods for compensating for the Doppler effect are: sweeping the laser frequency, spatially-dependent electric field, diffuse light, and broadband light. See Ref. [12] for more details.

The radiative force is able to cool atoms in a standing wave configuration under the correct conditions. In the low intensity limit, the forces from the two counter-propagating beams can be added together. This results in the expression for the force of

$$\begin{aligned} \mathbf{F} &= \hbar\mathbf{k}\frac{\gamma s_0/2}{1+s+(2(\delta-\mathbf{k}\cdot\mathbf{v}))/\gamma)^2} - \hbar\mathbf{k}\frac{\gamma s_0/2}{1+s+(2(\delta+\mathbf{k}\cdot\mathbf{v}))/\gamma)^2} \\ &\approx \frac{8\hbar k^2\delta s_0\mathbf{v}}{\gamma(1+s_0+(2\delta/\gamma)^2)^2} \equiv -\beta\mathbf{v} \end{aligned} \tag{1.19}$$

Terms of the order $(kv/\gamma)^4$ and higher have been neglected in the second line. The optical force as a function of atomic velocity is plotted in Figure 1.4 with $s_0 = 2$ and $\delta = -\gamma$. When the laser is tuned below atomic resonance ($\delta < 0$) the force opposes atomic motion. This scheme was given the name optical molasses due to the viscous drag it exerts on the atoms. Atoms with $v > \pm\gamma/k$ will only weakly interact with the light field and so the velocity capture range of this force is defined to be γ/k. It should be noted that the atomic ensemble

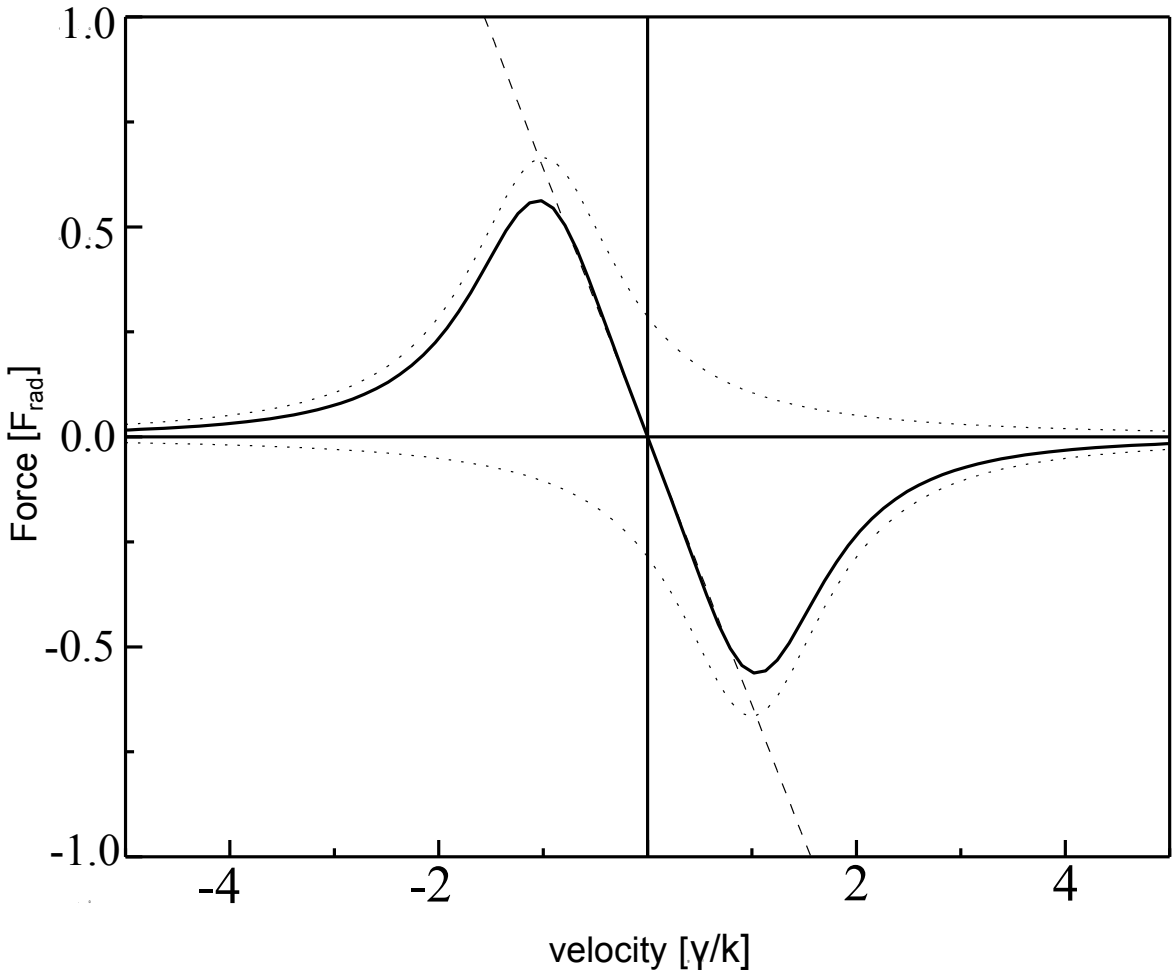

Figure 1.4: Force vs. velocity for optical molasses with $s_0 = 2$ and $\delta = -\gamma$. The x-axis is scaled by γ/k (units of m/s) and the y-axis is scaled in units of the maximum radiative force $\hbar k\gamma/2$. The dotted lines represent the force from each individual beam. The solid line is just the summation of these two forces, which is valid in the low intensity regime. The linear dashed line is an approximation of the optical force at small velocities and has a slope $-\beta$. Modified from [13].

does not reach $T = 0$ due to the heating effects from the random nature of absorption and emission even though the mean velocity is zero. For the typical atoms used in laser cooling experiments, alkali and metastable noble gases, this temperature limit is on the order of 100 μK [3].

1.2.3 Dipole Force

There are other optical forces whose force is not limited by the properties of the atomic transition as in the radiative force. Forces derived from cycles of absorption and stimulated emission may have magnitudes much greater than forces that rely on spontaneous emission. One example of a force that relies on stimulated emission to excite an atom is the dipole force.

Atoms present in a standing wave light field may also experience a force that derives from the spatial gradient of their light shifts [12]. The dipole force arises from the coherent exchange of momentum through absorption from one light field and stimulated emission into the opposing light field. The magnitude of this dipole force F_{dip} is limited only by the intensity of the light field driving these coherent processes

$$F_{dip} = \frac{2\hbar\delta s_0 \sin 2kz}{1 + 4s_0 \cos^2 kz + (2\delta/\gamma)^2} \tag{1.20}$$

where z is the position of the atom. However, according to Eq. 1.20, the spatial dependence of the force is oscillatory and goes to zero when averaged over a wavelength. Over a large ensemble there is no preferred direction for absorption or emission. It is also evident from Eq. 1.20 that the sign of the laser detuning, δ, determines if the atom will seek the nodes or anti-nodes of the standing wave. The dipole force can be used to trap atoms but it is unable to cool atoms due to its conservative nature. A mechanism is required to break the

symmetry of the standing wave.

High intensity blue-detuned molasses uses spontaneous emission to break this symmetry. In the presence of a blue detuned standing wave, the dressed atom eigenstates vary spatially with the light field intensity. Spontaneous emission provides a directional force and the irreversibility required for cooling of atoms. This was confirmed both numerically [16] and experimentally [17].

There are other more complex schemes that use non-monochromatic light to make use of the dipole force [18, 19]. The rectified dipole force refers to a scheme where a second, high intensity, far detuned standing wave is used to modulate the atomic transition frequency on the wavelength scale. In this case the dipole force is "rectified" to have a nonzero spatial average and has been investigated by many groups [20–22]. The force is much larger than the radiative force but the rectification mechanism is very sensitive to Doppler shifts. Such sensitivity necessarily leads to a small range of velocities for which the force is effective.

1.2.4 Bichromatic Force

In contrast to the rectified dipole force described above, choosing different beam parameters for the two frequencies of light can produce a force appropriate for cooling a thermal beam. The bichromatic force is described in great detail in Ref. [23–25] but a short discussion will be given here. Consider two counter-propagating beams with each containing two frequencies, $\omega_l \pm \delta$ with $\delta \gg \gamma$. Each beam can be thought of as an amplitude modulated field with the carrier frequency at the atomic resonance, and the modulation period π/δ. If each frequency component were to have the correct Rabi frequency, $\Omega = \pi\delta/4$, then each pulse would satisfy the π-pulse condition (complete population inversion as in Fig. 1.1). That is, a single pulse would cause an atom in the ground state to be excited and an atom in the

excited state to be deexcited. On average, if the phase of the two envelopes is set correctly, one beam will cause absorption, while the other beam will cause stimulated emission. This leads to a momentum change of $2\hbar k$ over a time period of δ/π or an optimum force of $2\hbar k\delta/\pi$. See Fig. 1.5 for a simple diagram of the bichromatic force setup. The bichromatic force is much larger than the radiative force $\hbar k\gamma/2$ given by Eq. 1.16.

The forces described in this section are usually only valid in the two level approximation and neutral atoms may have many magnetic sub-levels that are nearly degenerate. However there are techniques to suppress transitions to these other sub-levels in certain atoms. One of these techniques is optical pumping, described in the following section.

Two effects that need to be discussed, however, are spontaneous emission and the Doppler shift. Spontaneous emission may occur, thereby reversing the atomic response to the light fields. Proper choice of the envelope phase leads to more absorption by one beam and more stimulated emission by the other so that the average force is now $\hbar k\delta/\pi$ [23, 24]. The explicit velocity dependence of the bichromatic force is more complicated. A simple picture says the force should be constant in the limit of $kv \ll \delta$. A more detailed analysis in the doubly-dressed atom picture and numerical calculations show the bichromatic force has an effective velocity range of $\pm\delta/2k$ [23]. The bichromatic force as a function of velocity is plotted in Fig. 1.6.

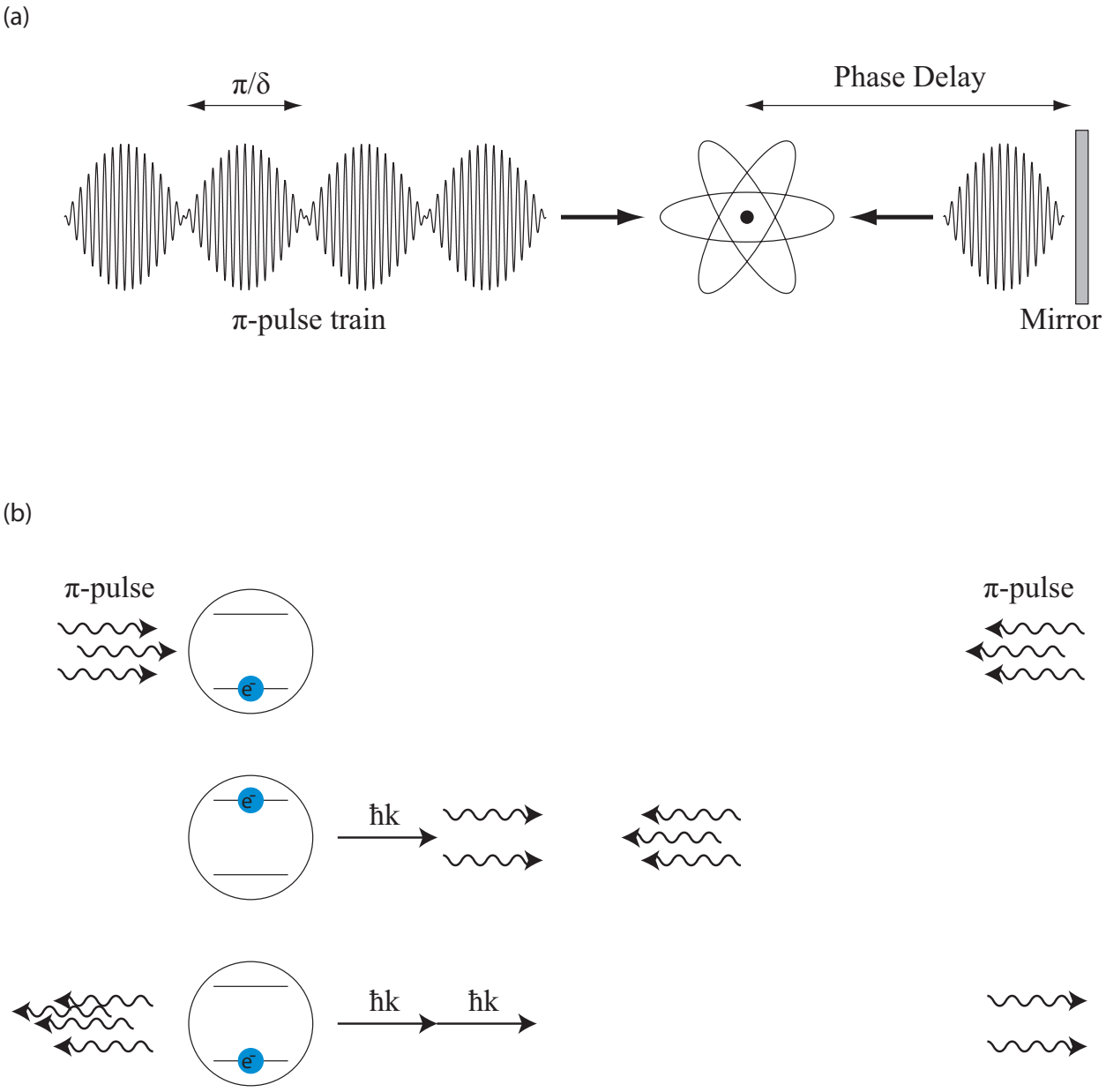

Figure 1.5: The two frequencies in the bichromatic laser beam create a series of π-pulses from the beat frequency. Each π-pulse excites or de-excites the atom in a time of π/δ leading to a force $(\hbar k\delta/\pi)$ much larger than F_{rad}. Taken from [26].

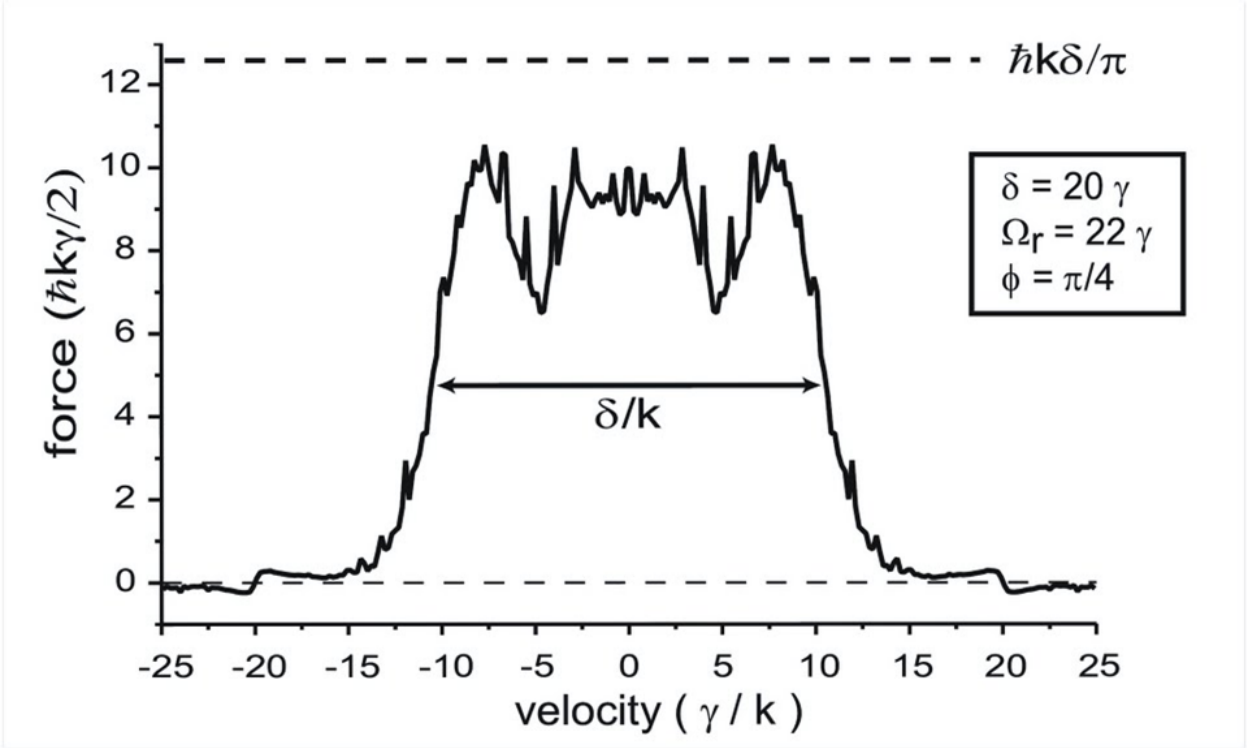

Figure 1.6: Bichromatic Force as a function of velocity for a fixed detuning, Rabi frequency, and relative phase. For this numerical calculation the parameters are chosen to be $\delta = 20\gamma$, $\Omega_r = 22\gamma$, and $\phi = \pi/4$. The force and velocity axes are in units of the radiative force and γ/k respectively. The strength and velocity range of the bichromatic force are an order of magnitude larger than the radiative force.

1.3 Optical Pumping

Optical pumping is a process by which atoms in many different magnetic sublevels can be transferred into the same magnetic sublevel. The relevant transition in this experiment is the $2^3S_1 \rightarrow 2^3P_2$ in He. Without the presence of an external magnetic field the magnetic sublevels of the ground state are degenerate and equally populated. The 2^3S_1 state has three magnetic sublevels ($m_j = -1,\ 0,\ +1$) and the 2^3P_2 state has five magnetic sublevels ($m_j = -2,\ -1,\ 0,\ +1,\ +2$). With the application of an external magnetic field, the energy associated with each sublevel shifts as

$$\Delta E_{m_j} = m_j g_j \mu_B B \tag{1.21}$$

where $\mu_B = e\hbar/2m_e$ is the Bohr magneton, B is the applied magnetic field, and g_j is the Landé g-factor given by $g_j = 1 + \frac{j(j+1)+s(s+1)-l(l+1)}{2(j+1)}$. The resulting energy shifts are generally less than those associated with spin-orbit coupling for weak magnetic fields [27]. If the energy shifts of these levels is larger than the natural linewidth of the transition, $\hbar\gamma$, then the states are no longer degenerate.

Atoms can only undergo transitions in the presence of external fields when $\langle\phi_g|\mathbf{r}|\phi_e\rangle$ (to a first order approximation) is nonzero. There are certain selection rules that govern these E1 or electric-dipole transitions. Important selection rules to keep in mind are $\Delta J = 0, \pm 1$ [without $J = 0 \rightarrow J = 0$], $\Delta S = 0$, $\Delta L = 0, \pm 1$, and $\Delta m_j = 0 \pm 1$ [without $m_j = 0 \rightarrow m_j = 0$ when $\Delta J = 0$].

In the presence of linearly (π) polarized light only stimulated transitions of $\Delta m_j = 0$ are allowed. Spontaneously emitted light is randomly polarized so the atom is allowed to decay with $\Delta m_j = 0 \pm 1$. The probability of the atom to decay to these different sublevels is

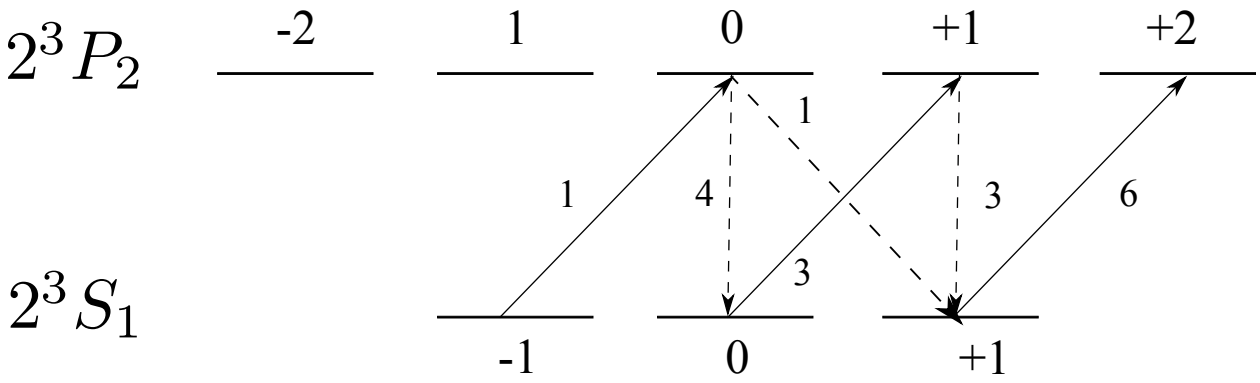

Figure 1.7: Transition probabilities for the optical pumping process in the presence of σ^+-polarized (left-handed) light and spontaneous decay for the $2^3S_1 \rightarrow 2^3P_2$ transition in metastable helium. Solid lines are the allowed E1 transitions for σ^+-polarized light and are labeled by their relative transition probabilities. The dashed lines represent the allowed transitions for the randomly-polarized spontaneous decays. Over time the population in the $m_j = +1$ ground state will increase at the expense of the $m_j = -1,\ 0$ ground states.

based on the wavefunction overlap of the states in question. Relative transition rates may be found by calculating the Clebsh-Gordon coefficients of each transition. For a $J = 1 \rightarrow J = 2$ transition with π-polarized light there is a preference to decay to the $m_j = 0$ ground state. Based on Clebsh-Gordon coefficients in the presence of CW, resonant, π-polarized light, and a magnetic field, there will be 4 atoms in the $m_j = 0$ ground state for every 3 atoms in $m_j = -1$ or $m_j = +1$ ground state on average over many cycles.

In laser cooling it is often favorable to use a "closed" transition. In a closed transition the atom may only traverse between a single ground and excited state. Left-handed (right-handed) circularly polarized light will cause excitation to a state with $\Delta m_j = +1$ ($\Delta m_j = -1$). Due to the Clebsh-Gordon coefficients, atoms illuminated by left-handed (σ^+), circularly-polarized, near resonant light will tend to the $m_j = +1$ ground state over many cycles of absorption and spontaneous emission (see Fig. 1.7). Once an atom is in the $m_j = +1$ ground state it can be excited only to the $m_j = +2$ state followed by stimulated emission or spontaneous decay back to the $m_j = +1$ ground state. In this sense all of the

atoms are optically pumped to the $m_j = +1$ ground state. The relative populations of the allowed σ^+ transitions are plotted in Figure 1.8 as a function of time in the presence of on-resonance light with $\Omega = 10\gamma$ ($\gamma \equiv 1/\tau$ where τ is the lifetime of the excited state).

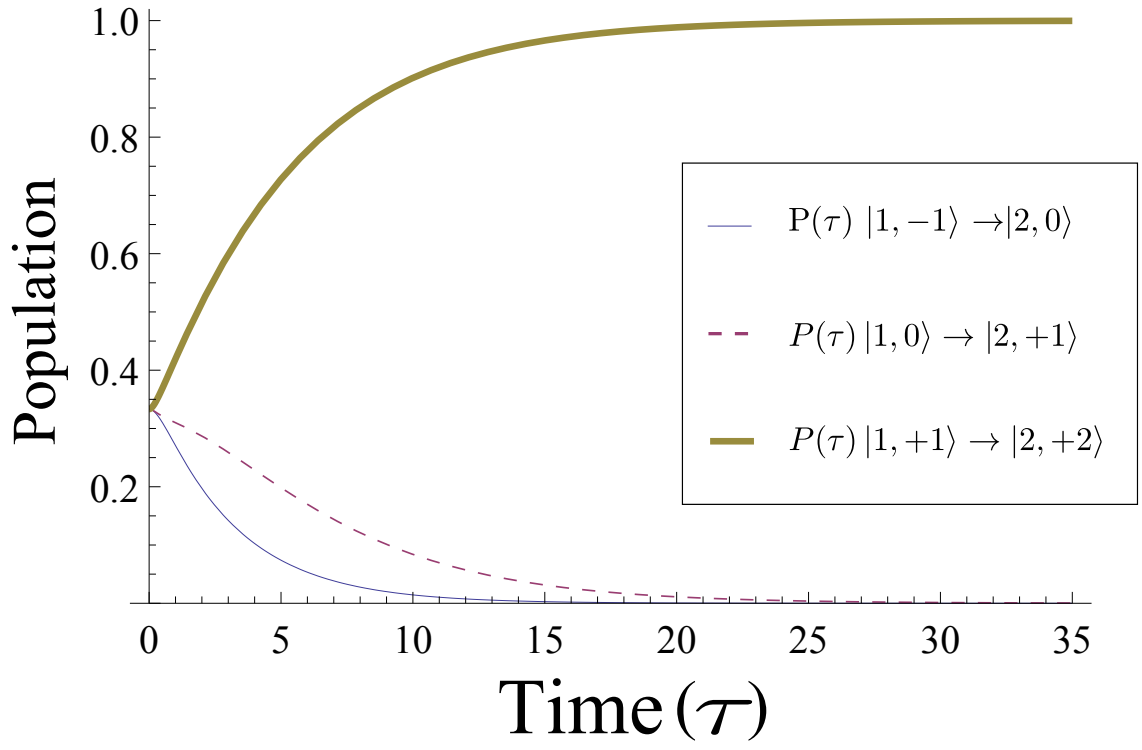

Figure 1.8: Relative populations of the states connected by the 3 possible σ^+ transitions for the $2^3S_1 \rightarrow 2^3P_2$ transition in metastable helium in the presence of CW σ^+-polarized light with $\Omega = 10\gamma$. The calculation begins with equal populations in the ground state magnetic sublevels (3 for J=1). After 20 lifetimes nearly 99% of the atoms are in a single cycling transition.

Chapter 2

Theory of Adiabatic Rapid Passage

The focus of this dissertation is the study of the optical force on two-level atoms in the presence of periodic adiabatic rapid passage (ARP) sequences. ARP in the optical regime requires a light pulse to be swept through the resonance of a two level system in a time much shorter than the lifetime of the excited state $\tau = 1/\gamma$. A series of properly tailored, counterpropagating pulses can produce a strong unidirectional force through cycles of absorption and stimulated emission. The magnitude of such a force is limited by the repetition rate of these cycles. In the ideal case, a momentum transfer of $2\hbar k$ in a time T leads to a force $F_{ARP} = 2\hbar k/T$ which can be much greater than the radiative force, $F_{rad} = \hbar k\gamma/2$. The work in this chapter has been published in Reference [10].

2.1 Adiabatic Rapid Passage

ARP, a well known method to invert the population of a two-level system in the magnetic resonance community [28], is best visualized by observing the path of the Bloch Vector $\mathbf{R} = [u, v, w]$ on the Bloch sphere [10]. The south pole of the Bloch sphere, $\mathbf{R} = [0, 0, -1]$,

represents the ground state $|g\rangle$, while the north pole, $\mathbf{R} = [0, 0, 1]$, represent the excited state $|e\rangle$.

The Schrödinger equation can be reformulated to show how the time-dependence of the Bloch vector depends on an artificial "torque" vector, $\mathbf{\Omega}(t) \equiv [\Omega_r(t), \Omega_i(t), -\delta(t)]$, by the equation $d\mathbf{R}(t)/dt = \mathbf{\Omega}(t) \times \mathbf{R}(t)$. Here $\Omega_{r,i}$ are the real and imaginary parts of the Rabi frequency given by $\hbar\Omega(t) \equiv \langle g|e\mathcal{E}(t)\cdot\mathbf{r}\,|e\rangle$, and $\delta(t) \equiv \omega_\ell(t) - \omega_a$ is the detuning of the optical frequency $\omega_\ell(t)$ from the atomic frequency ω_a.

In the usual case of ARP, the torque vector begins near the south pole, nearly parallel to $\mathbf{R}$, and is slowly, and continuously swept towards the north pole by sweeping the detuning from one side of atomic resonance to the other side symmetrically. The Rabi frequency begins at 0, increases to its maximum at $\delta = 0$, and then decreases to zero once again. To illustrate this process, consider a sweep profile characterized by $\delta(t) = \delta_0 \cos(\omega_m t)$ and $\Omega(t) = \Omega_0 |\sin(\omega_m t)|$ that can start at $t = 0$ and last for time π/ω_m with a frequency sweep range of $2\delta_0$ and a maximum Rabi frequency Ω_0.

ARP is most robust when the parameters satisfy both the "adiabatic" and "rapid" condition summarized by the inequality:

$$\delta_0 \sim \Omega_0 \gg \omega_m \gg \gamma \tag{2.1}$$

When this inequality is satisfied, the trajectory of the Bloch vector, $\mathbf{R}$ on the Bloch sphere adiabatically tracks $\mathbf{\Omega}$ in a nearby spiral path long before the excited state decays back to the ground state. This process may take an atom initially in the ground state, $\mathbf{R} = [0, 0, -1]$, and put it into the excited state, $\mathbf{R} = [0, 0, 1]$, with very high probability as shown in Fig. 2.1(a).

It has been shown in Ref [29], however, that $\mathbf{\Omega}$ orbits like that shown in Fig 2.1(b) can also produce robust population inversion. The parameters of this $\mathbf{\Omega}$ are characterized

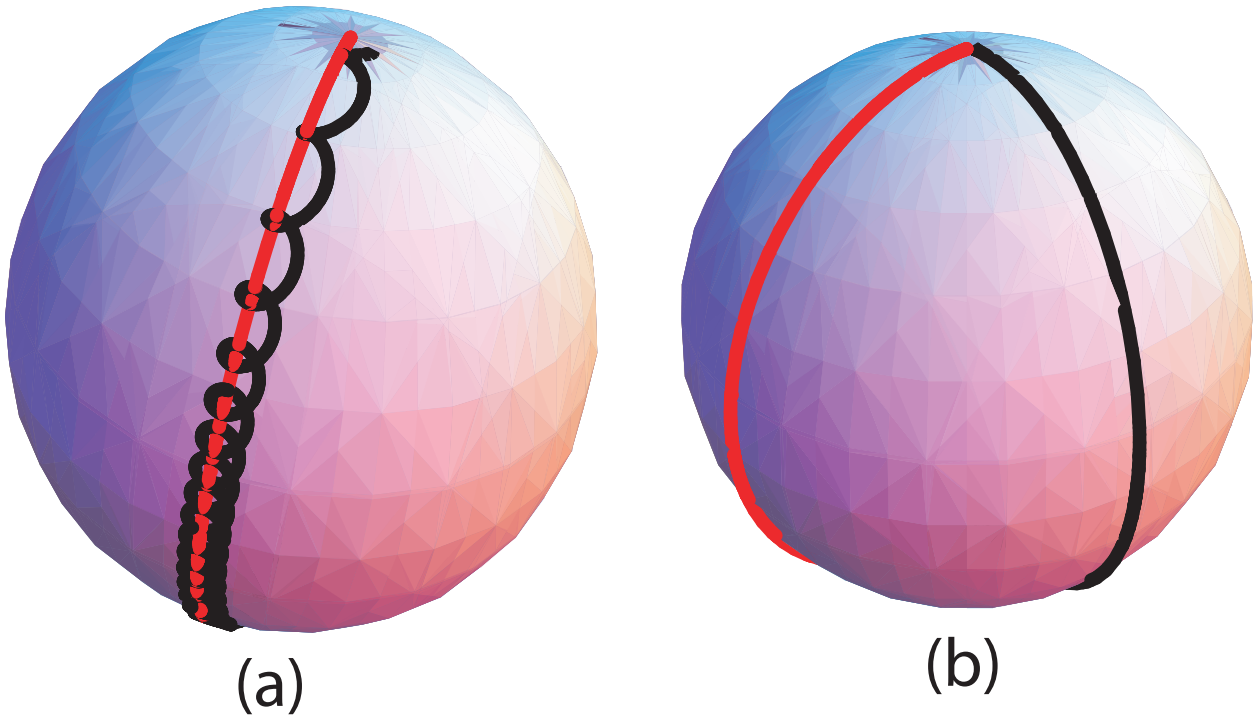

Figure 2.1: Plot of two trajectories (the north pole shown) of $\mathbf{R}(t)$ (black) and $\mathbf{\Omega}(t)$ (grey). Part (a) has $\delta_0 = 30\,\omega_m$ and $\Omega_0 = 50\,\omega_m$ to show the usual ARP where $\mathbf{R}$ makes many precession cycles and stays close to $\mathbf{\Omega}$ during the sweep. Part (b) has $\delta_0 = 1.10\,\omega_m$ and $\Omega_0 = 1.61\,\omega_m$ to show the unusual case where the trajectory of $\mathbf{R}$ is a simple arc along a meridian that is $\sim 90^\circ$ away from the path of $\mathbf{\Omega}$.

by $\delta_0 \sim \Omega_0 \sim \omega_m \gg \gamma$ well outside the usual ARP domain as stated in Eq. 2.1. By relaxing the adiabatic condition of ARP, the pulse duration (π/ω_m) may be decreased, which leads to faster absorption-stimulated emission cycles, and therefore larger optical forces at reasonable values of Ω_0 and δ_0. These forces, predicted by Ref. [10, 29], were experimentally corroborated [9].

The timing scheme for ARP-based absoprtion-stimulated emission cycles is illustrated by Fig. 2.2. A pulse of duration π/ω_m from one direction (*e.g.,* from the left) is represented by the half-period sine wave in the upper trace, and its upward frequency sweep is represented by the curve in the lower trace. A second pulse, incident from the opposite direction (*e.g.,*

from the right), is represented by the second half-period sine wave, also with an upward frequency sweep. Then there is a dead time of $2\pi/\omega_m$ for experimental reasons [13] as well as for the theoretical reasons that will become obvious with the inclusion of spontaneous emission. The sequence can be repeated any number of times. In this simple picture, the optical force from a single pulse pair is $F_{\rm ARP} \equiv \hbar k \omega_m/\pi$ and can be orders of magnitude larger than the ordinary radiative force F_{rad}.

The Optical Bloch Equations enable the calculation of the optical force over multiple ARP sequences, and may also include the effects of Doppler shifts and spontaneous emission. The force onto the atom can be calculated using the Ehrenfest theorem [12]

$$\mathbf{F} = < -\nabla \mathcal{H} > = \mathrm{Tr}\big[\, \nabla \mathcal{H} \rho \,\big] = \frac{\hbar}{2}\big(u \nabla \Omega_{\rm r} + v \nabla \Omega_{\rm i}\big), \tag{2.2}$$

where $\Omega_{\rm r,i}$ and u and v are the corresponding components of torque and Bloch vectors. In the case of two counter-propagating light fields whose wavenumber is k, the resulting force is

$$\mathbf{F} = \frac{\hbar \mathbf{k}}{2}\left(\left(\mathbf{\Omega}_+ - \mathbf{\Omega}_-\right) \times \mathbf{R}\right)_3 \tag{2.3}$$

where the force is given by the third component of this vector product. The torque vectors $\mathbf{\Omega}_+$ and $\mathbf{\Omega}_-$ refer to the right and left propagating fields respectively. The case of temporally overlapping ARP pulses has been considered [30]. If the pulses are not temporally overlapped one can treat them individually and write

$$\mathbf{F} = \frac{\hbar \mathbf{k}}{2}\left(\mathbf{\Omega}_\pm \times \vec{R}\right)_3 = \frac{\hbar \mathbf{k}}{2}\dot{w}. \tag{2.4}$$

Identifying $\dot{w}$ yields an expected result: a momenta of $\hbar k$ is exchanged between the light field and the atom if the Bloch vector is driven from one pole to the other. The force of a

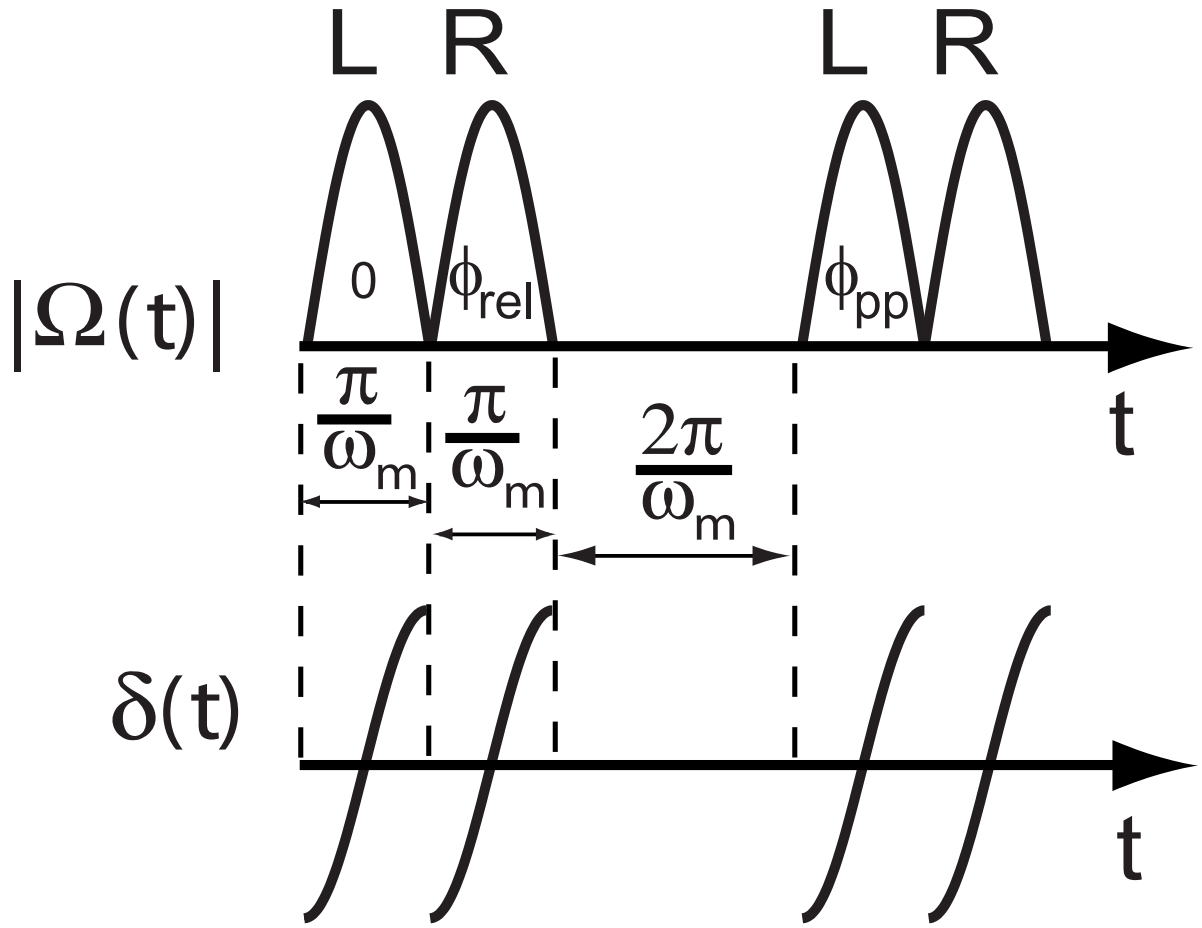

Figure 2.2: The upper trace shows the Rabi frequency $\Omega(t)$ during the pulse pair followed by the dead time, and then the next pulse pair. The lower trace shows the frequency sweep $\delta(t)$, in this case both upwards. (Figure adapted from Ref. [13].)

single pulse expressed through discretization of $\dot{w}$ is

$$\mathbf{F} = \frac{\hbar \mathbf{k}}{2} \frac{\omega_m}{\pi} \Delta w \tag{2.5}$$

In the interaction picture one may use the Optical Bloch Equations (Eq. 1.14) with the torque vector

$$\Omega_{\mathrm{r}} = \Omega_0 |\sin(\omega_m t)| \cos \alpha(t)) \tag{2.6}$$

$$\Omega_{\mathrm{i}} = \Omega_0 |\sin(\omega_m t)| \sin \alpha(t)) \tag{2.7}$$

$$\delta = 0 \tag{2.8}$$

and

$$\alpha(t) = -(\delta_0/\omega_m)|\sin(\omega_m t)| + (\mathbf{k} \cdot \mathbf{v})t + \phi \tag{2.9}$$

Here the frequency detuning $\delta(t)$ is included in the complex phase $\alpha(t)$ as $-(\delta_0/\omega_m)|\sin(\omega_m t)|$ along with contributions that come from Doppler shifts, $(\mathbf{k} \cdot \mathbf{v})t$, and unavoidable phase differences between pulses in a pair, ϕ_{rel}, as well as between pairs, ϕ_{pp} (see Fig. 2.2). The sign of δ_0 determines the direction of the frequency sweep for a single pulse. A positive δ_0 signifies a sweep up in frequency (as in Fig. 2.2) and a negative δ_0 signifies a sweep down.

These OBE's (Eq. 1.14) are solved numerically in Fortran-90 using the BIM subroutine [31] and an example of this code can be found in Appendix A. The next section will describe the results of these calculations under various conditions.

2.2 ARP Force on Two-Level Atoms

2.2.1 ARP Force on Stationary Atoms

In the absence of spontaneous emission, stationary atoms ($v = 0$) are described by the equations similar to those used previously to study dependence of optical forces from single swept pulses [29]. However, phase differences between pulses, ϕ_{rel} and ϕ_{pp}, caused by atomic motion and the jitter of the timing that starts each sequence respectively, are unavoidable experimentally and their effects are discussed below.

To demonstrate the effects of phase, I choose to vary ϕ_{rel} while holding $\phi_{pp} = 0$ and calculate the average optical force over the duration of the pulse sequence. This calculation simulates the ARP force on an atomic sample if the spatial extent of the sample along $\mathbf{k}$ is much larger than the optical wavelength (typical of most experiments). Figure 2.3 shows maps of the optical force averaged over 12 pulse pairs calculated for various values of Ω_0 and δ_0 scaled by ω_m. Averaging over 12 pulse pairs is sufficient to demonstrate regions of large, robust forces in the nonadiabatic regime. These maps show that the optical force depends strongly on relative phase as well as on the relative sign of δ_0 in consecutive ARP pulses.

The "up-up" case (top row of Fig 2.3) describes an ARP pulse pair with $\delta_0 > 0$ leading to the upward evolution of the torque vector on the Bloch sphere. It corresponds to our experiments using a retroreflected train of light pulses with appropriate delays that necessarily resulted in pulse pairs with same upward or downward sweeps (see Ref. [13]). Figure 2.3a shows the average calculated force with $\phi_{rel} = 0$. The strength of the ARP force is more sensitive to the values of Ω_0 and δ_0 than in Ref. [32] because those calculations were done for a single sweep and deviations from the ideal case accumulate with each successive sweep. Nevertheless, even after a very large number of sweeps there is a very strong ARP force for parameter values that do not satisfy the traditional conditions given in Eq. 2.1 [32].

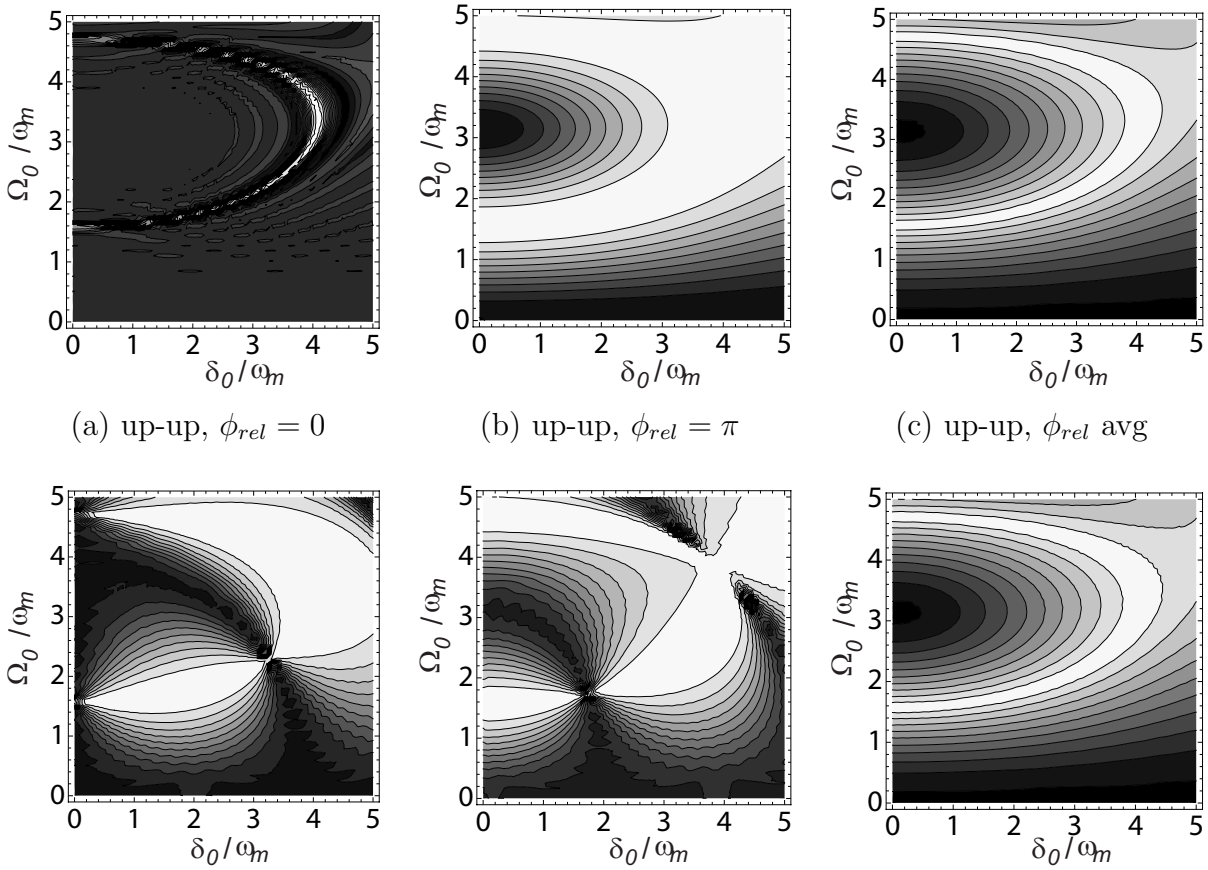

(a) up-up, $\phi_{rel} = 0$ (b) up-up, $\phi_{rel} = \pi$ (c) up-up, ϕ_{rel} avg

(d) up-down, $\phi_{rel} = 0$ (e) up-down, $\phi_{rel} = \pi$ (f) up-down, ϕ_{rel} avg

Figure 2.3: Contour plots of the average force calculated over a range of the experimental parameters, Ω_0 and δ_0, scaled by ω_m. White regions represent areas with the greatest average force, approximately $F_{ARP}/2$, and the darkest regions correspond to zero average force. The top row (parts (a), (b), and (c)) are for all sweeps upward, corresponding to the experiments of Ref. [13] . Part (a) shows the case for $\phi_{rel} = 0$, part (b) shows the case for $\phi_{rel} = \pi$, and part (c) shows the average over the region between 0 and π. The bottom row shows the corresponding results for pulse pairs with up-down sweep sequences. We leave $\phi_{pp} = 0$ in all plots.

By contrast, the results when $\phi_{rel} = \pi$ are quite different (see Fig. 2.3b). Here, each optical pulse has a π phase shift relative to its neighbors that clearly makes ARP much more robust against changes in Ω_0 or δ_0. It is not difficult to show mathematically that the second pulse of an ARP pair will cause $\mathbf{R}$ to retrace its path back to the south pole. This results in complete cancellation of the errors associated with the first pulse pair and hence a robust force.

The "up-down" case (bottom row of Fig. 2.3) corresponds to pairs of ARP pulses that switch from $\delta_0 > 0$ in one pulse to $\delta_0 < 0$ in the next pulse. This case, illustrated in Fig. 2.3d, shows that changing the nature of the sweep without changing its parameters can increase the efficiency of ARP over a wide range of parameter values. Using $\phi_{rel} = \pi$ effectively changes the sign of Ω_0 so that $\mathbf{\Omega}$ continues past the north pole as the second sweep begins so that the torque vector evolves continuously and completes its second sweep toward the south pole on the opposite side of the Bloch sphere. The force map for this case is in Fig. 2.3e.

As ϕ_{rel} is varied smoothly from 0 to π for the up-up sweeps, the region of high efficiency ARP evolves quickly from the narrow region of Fig. 2.3a to the broader region of Fig. 2.3b even for $\phi_{rel} < \pi/2$, and then stays quite robust in the region $\pi/2 < \phi_{rel} < \pi$. Although such phase shifts could be controlled in principle, in any real experiment, the region occupied by a sample of atoms always exceeds the wavelength of the light so different atoms experience different values of ϕ_{rel}.

It is not difficult to imagine how averaging over values of ϕ_{rel} between Fig's. 2.3a and 2.3b can result in Fig. 2.3c because the regions of efficient ARP simply expand and distort a bit between these two extremes. By contrast, the same variation of ϕ_{rel} in Fig. 2.3d causes the narrow pinch near (0, 1.6) at the left edge of Fig. 2.3d to drift toward the right, ending near (1.7, 1.7) in Fig. 2.3e. The evolution between the limits shown in Fig's. 2.3d and 2.3e

is difficult to visualize without access to the several plots between them. They show that this drift leaves a trail of high efficiency ARP region that is maintained by the wider regions on each side of the pinch. The consequence is that the averages shown in Fig's. 2.3c and 2.3f look surprisingly similar.

Two important observations about the effect of ϕ_{rel} on the forces from ARP emerge from Fig. 2.3. First, repetitive sweeps in the same directions are the most robust if relative phase in a pulse pair is equal to π. Second, averaging over relative phase produces results of the maps for optical force that are independent of the sweep directions as shown in the right column of Fig. 2.3.

2.2.2 ARP Force on Moving Atoms

In all of the calculations described here, the atomic velocity will be kept fixed thus constituting the "dragged atom approach" [12]. Sample calculations including velocity changes were carried out. In some cases, calculation time increased considerably, but the force results did not change in any noticeable way. Therefore I feel justified in retaining this approximation.

It is clear from Fig. 2.3 that the ARP force on atoms at rest is close to its maximum value $F_{ARP}/2$ over a large range of experimental parameters. Atomic motion in the "dragged atom approach" assumes that the velocity v along the axis of the counterpropagating ARP pulses is fixed, leading to constant Doppler shifts $\pm kv$. Therefore, it is reasonable to assume that the ARP force will be in the neighborhood of $\sim F_{ARP}/2$ for all atoms whose motion leads to Doppler shifts $\pm\, kv$ that are well below the sweep range $\pm\, \delta_0$.

With moving atoms, a significant change in ϕ_{rel} occurs during the flight of an atom if it moves by more than $\lambda/4$ during the interaction time $t_{\rm int}$ that could be estimated based

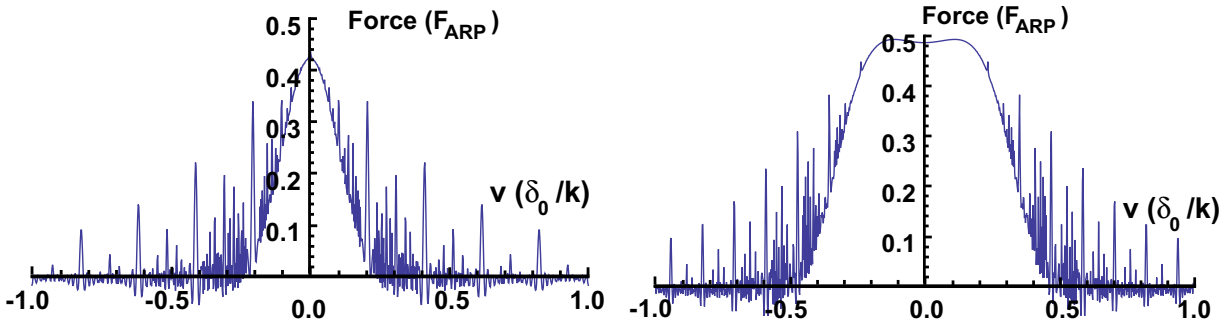

(a) (2.4, 1.8) (b) (4.19, 3.39)

Figure 2.4: The velocity dependence of the ARP force for various values of the light field parameters given as (δ_0/ω_m, Ω_0/ω_m). These two sets of parameter values were chosen from the white region of Fig's. 2.3c and 2.3f. Here ϕ_{pp} was fixed at 0 but ϕ_{rel} was averaged.

on the velocity range of the ARP force, $|kv| < \delta_0$. Choosing $(F_{ARP}/2M)t_{\rm int} = \delta_0/2k$ gives $t_{\rm int} = \pi M\delta_0/\hbar k^2\omega_m$. Avoiding a significant phase shift then requires that the atomic velocity be $< v_r(\omega_m/2\delta_0)$, a speed always less than the recoil velocity $v_r \equiv \hbar k/M$, corresponding to a temperature of a few μK or less. Thus the effect of ϕ_{rel} cannot be neglected, so one must average over it.

To present the effect of atomic motion in more detail, I chose two sets of values for $(\delta_0/\omega_m, \Omega_0/\omega_m)$. The first set (2.4, 1.8) is from our previous work [32] and corresponds to part of the narrow region of the maximum ARP force in Fig. 2.3c. The velocity dependence in this case is presented in Fig. 2.4a where the force in units of F_{ARP} is plotted *vs.* velocity (plotted in units of δ_0/k, the velocity where the Doppler shift equals the range of the ARP sweep). It shows that the velocity range where the force is half of its maximum value is $|kv| \approx \delta_0/8$. However, this velocity range is expanded dramatically by choosing laser parameters to be (4.19, 3.39) that correspond to the broader region of the maximum ARP force in Fig. 2.3c.

One of the most obvious features of Fig. 2.4 is the multitude of very narrow spikes,

especially at higher velocities. These are resonances (which are not computational artifacts) that occur when the atomic velocity satisfies $v = f\omega_m/4k$, where f = rational fraction, as suggested in App. B of Ref. [13]. This velocity condition implies that atoms move by an integer number of half wavelengths during a time of (pulse pair + dead time $= 2 \times 2\pi/\omega_m$) so that atoms experience all pulse pairs with the same value of ϕ_{pp} [29].

In experiments however, ϕ_{pp} cannot be kept fixed. During the interaction time, each atom may experience a range of values of both ϕ_{rel} and ϕ_{pp} as discussed above. Therefore, Fig. 2.5 is based on averages over both phases. For ϕ_{rel} I choose 21 evenly spaced phases and then average all results. For ϕ_{pp} the phase is determined by random numbers at the beginning of each pulse pair, and the calculation is averaged over the 21 values of ϕ_{rel}. Then the procedure is repeated 25 times and the averages are averaged.

The velocity dependence of the ARP force is plotted for four sets of parameters in Fig. 2.5, chosen from our previous work. Each of the four plots in Fig. 2.5 shows that the height of the spikes is strongly reduced by the averaging over the phases, and three of them show that the velocity range $|kv| \approx \delta_0/4$.

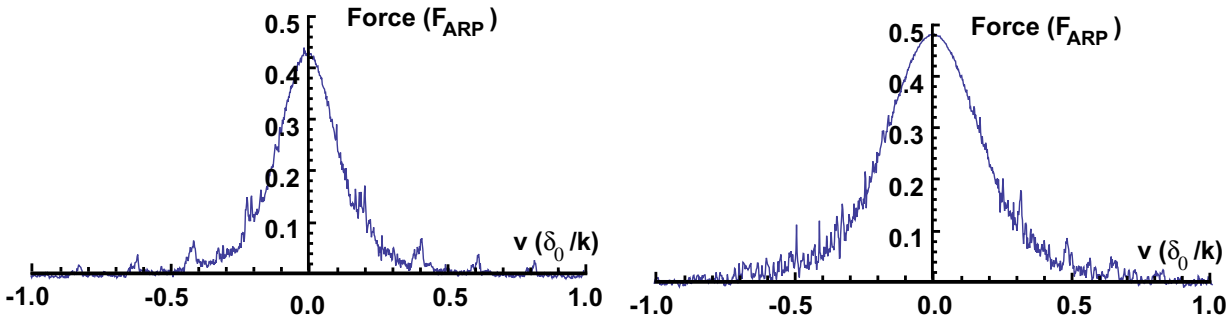

(a) (2.4, 1.8)

(b) (3.0, 4.4)

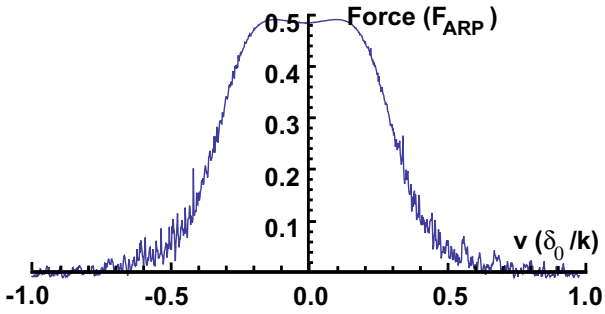

(c) (4.19, 3.39)

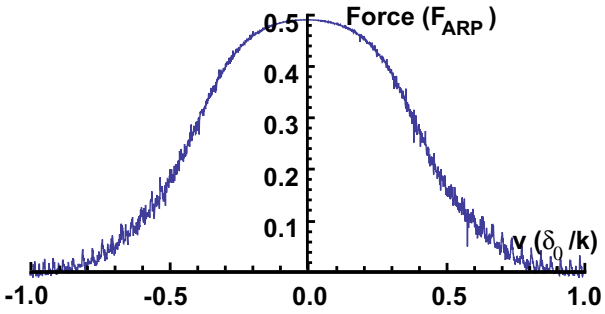

(d) (14, 18)

Figure 2.5: Force *vs.* velocity plots with averaging over both ϕ_{rel} and ϕ_{pp} for three parameter sets matching those of Fig. 2 of Ref. [32] (parts a, b, and d) and one (part c) corresponding to the wide part of Fig. 2.3c.

2.3 The Effects of Spontaneous Emission

Spontaneous emission serves as the origin of the word "rapid" in ARP by requiring that the frequency sweep rate be much larger than the natural decay rate γ as stated in Eq. 2.1. Otherwise, the concomitant damping reduces the atomic coherence established by the laser light and it precludes complete atomic inversion.

A typical dependence of the force on the ratio of ω_m/γ is shown in Fig. 2.6 for 12 pulse pairs with $\delta_0 = 4.19\omega_m$ and $\Omega_0 = 3.39\omega_m$. The solid curve is for an atom at rest while the other three are for atoms with $v = \delta_0/3k$ and different sweep directions. When $\omega_m/\gamma \sim 1$, spontaneous emission returns the atom to the ground state frequently enough that the counterpropagating pulse pairs are inefficient at transferring momentum $2\hbar k$ to the atoms. As ω_m/γ increases, the atom-light coherence is preserved for more pulse pairs, thus more momentum can be transferred from the light field to the atoms before a spontaneous emission event occurs.

However, satisfying the "rapid" condition (R in ARP) by choosing $\omega_m/\gamma \gg 1$ for a single pulse pair does not eliminate effects of the spontaneous emission during a long sequence of pulses. The possibility of a spontaneous emission to occur before the arrival of the second pulse of a pair can have a huge effect because the second pulse would then deliver momentum $\hbar k$ in the wrong direction resulting in the reversal of the ARP force. Such a force reversal is unlikely to be immediately repeated, thus many sequential pulses will maintain the force in the wrong direction. On average the force would vanish. In order to ameliorate this force reversal, we allow a dead time between each pair of pulses. In this case, an atom left in the excited state after the second pulse in a pair has a greater chance to return to the ground state before the arrival of the next pulse pair, effectively restoring the original direction of the force (see Ref's. [13, 29]).

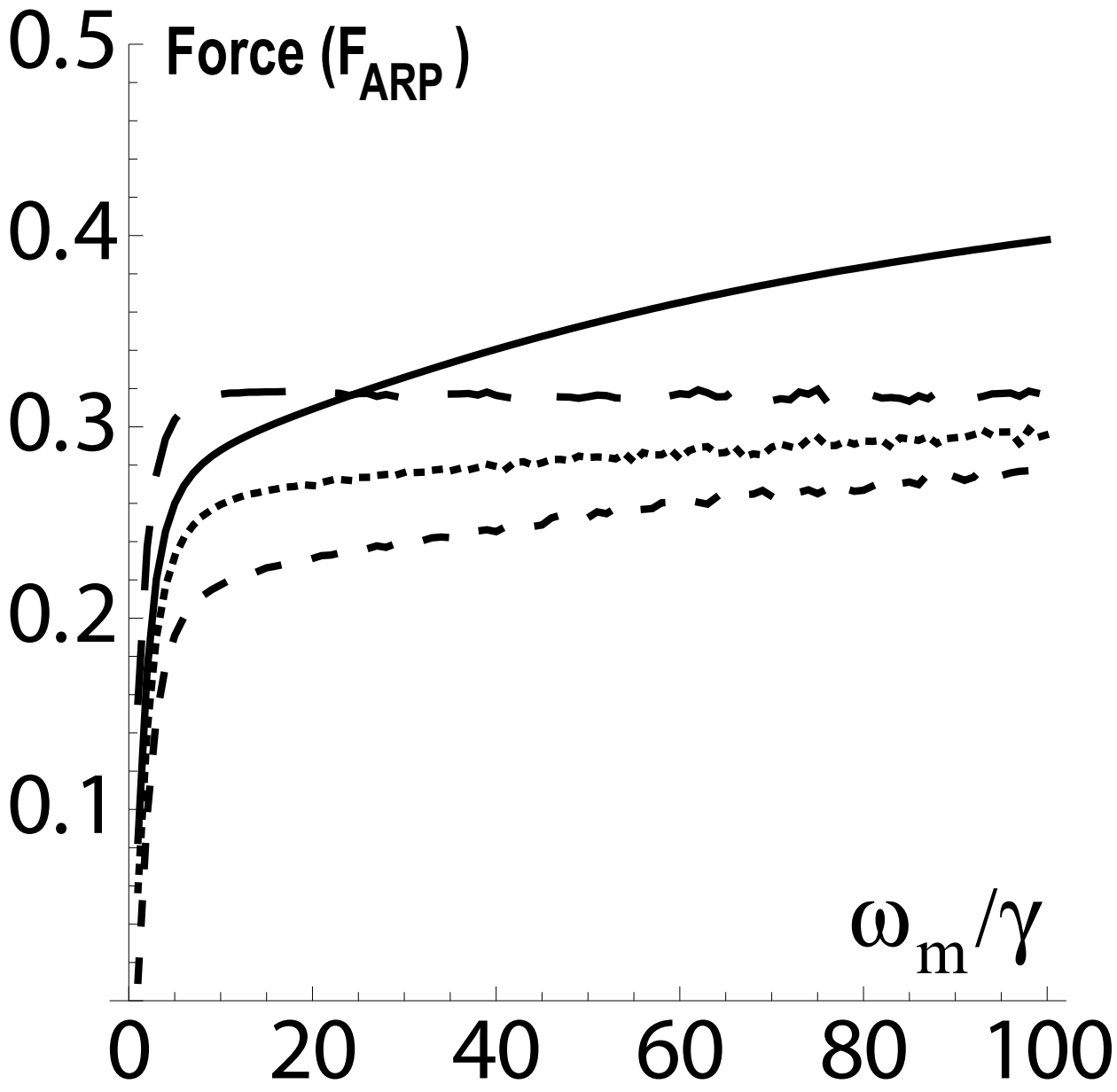

Figure 2.6: The ARP force depends on the sweep rate ω_m/γ for $v = 0$ (solid) and on sweep direction for $v = \delta_0/3k$, which is about the velocity where Fig. 2.5 shows the force has half of its maximum value. The long dashed curve is for the down-down case; the dotted one is for the up-down or down-up case, and the short dashed one is for the up-up case. The arrangement of these three curves would be reversed for $v < 0$.

Figure 2.7 shows the dependence of the force on the dead time resulting from multiple ARP pulse pairs having $\omega_m/\gamma = 100$. Five choices for the dead time with π/ω_m increments have been considered. For zero dead time (solid curve), the ARP force is reduced to zero after a small number of pulse pairs because of the increased probability of force reversal during a pulse sequence. However, the inclusion of dead time allows for the ARP force to be maintained over many more pulse pairs. The greater the amount of dead time, the faster the sequence can be repeated, but the more likely the sign of the force can be reversed. A simple picture of this process that does not include the finite pulse length would lead to a force as a function of dead time for long interaction times ($t_{int} \gg \tau$) of $F_{ARP}(T_d/(1+Td)^2)$, where T_d is in units of $2\pi/\omega_m$. Though the magnitude of the force is in disagreement with the numerical results, this simple picture agrees with the numerics as to the position of the maximal force at a dead time of $2\pi/\omega_m$ over very many pulse pairs, thus justifying its use in this paper.

Choosing $\omega_m/\gamma \gg 1$ and introducing the dead time do not prevent the decrease of ARP force over a long interaction time ($\gg 1/\gamma$). This reduction occurs because the damping in the optical Bloch equations decreases the length of the Bloch vector $|\mathbf{R}|$ from its initial value of unity to a steady state value less than one. This simply means that the atoms are in a superposition of ground and excited states, and that the coherence has been reduced by the damping associated with spontaneous emission. For the case of $|\mathbf{R}| < 1$, even perfect pulse sequences cannot transfer momentum $2\hbar k$ to atoms since the Bloch vector cannot reach from pole to pole of the Bloch sphere. This limits the magnitude of momentum transfer by each pulse pair to a steady state value over long times so that the force scale of Fig. 2.3 is reduced below $F_{\mathrm{ARP}}/2$, but the contour plots of average force do not change shape.

The velocity dependence of the ARP force with optimal dead time of $2\pi/\omega_m$ is shown in Fig. 2.8. The plots result from solving the optical Bloch equations for $(\delta_0/\omega_m, \Omega_0/\omega_m) =$

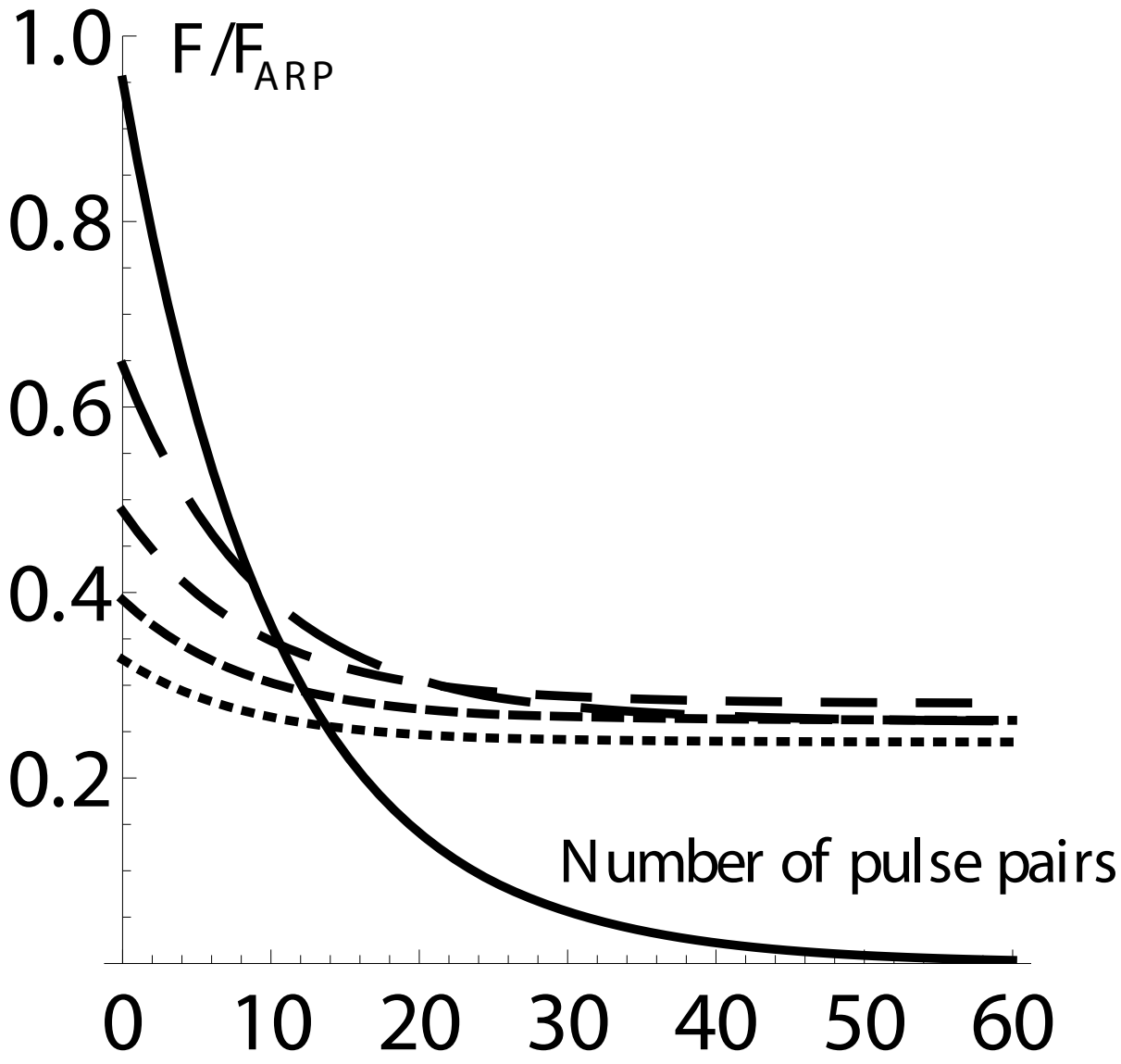

Figure 2.7: Calculated force *vs.* number of pulse pairs for various values of the dead time between pulse pairs. The solid curve is for zero dead time, and the increasingly smaller dashes correspond to integer multiples of π/ω_m dead time (1, 2, 3, and 4 respectively). Although the initial force values are different for a range of dead times, they eventually converge toward $F \approx F_{ARP}/4$.

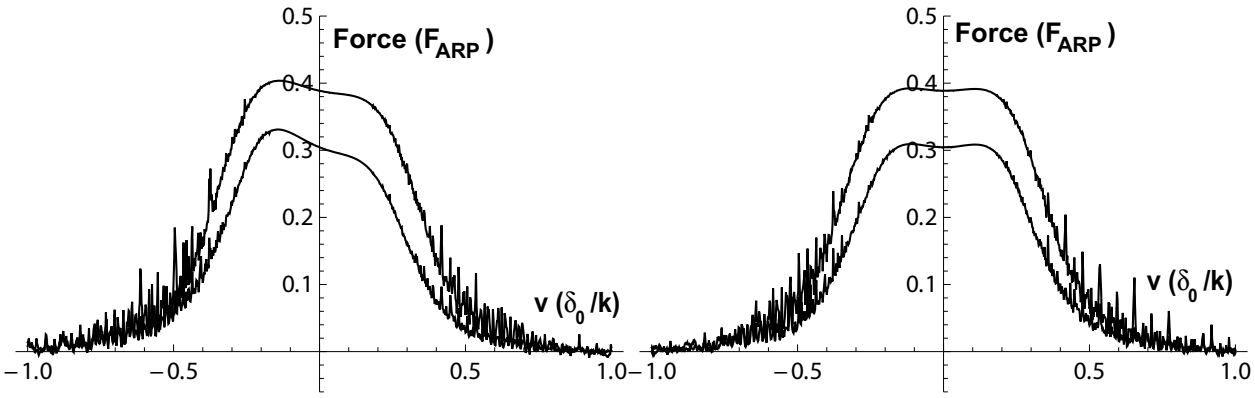

(a) (Up-up) (b) (Up-down or reverse)

Figure 2.8: Calculated velocity dependence of the ARP force for two sweep schemes at $(\delta_0/\omega_m, \Omega_0/\omega_m) = (4.19, 3.39)$ as in Fig. 2.5c. In part (a) the frequency in both pulses of each pair are swept from red to blue. Sweeps from blue to red produce a mirror image. In part (b) each pulse of a pair has opposite directions for the frequency sweeps, either from red to blue or from blue-to-red. The results are the same. In both (a) and (b) both ϕ_{rel} and ϕ_{pp} are averaged, just as in Fig. 2.5.

(4.19, 3.39) with phase averaging, and a spontaneous emission rate given by $\omega_m/\gamma = 100$. Two sequences of pulse pairs have been analyzed and are represented by the upper and lower curves for twelve and sixty pulse pairs, respectively. These curves clearly demonstrate that spontaneous emission reduces the magnitude of the force as compared with the plots of Fig. 2.5. We have found that the steady state magnitude of the ARP force is reached after sixty pulses which means that our recent experiments with more than sixty pulse pairs were done in the steady state regime [9].

The most noticeable effect of spontaneous emission on the ARP force is the unexpected asymmetry with respect to the velocity reversal when consecutive sweeps are in the same direction, as shown in Fig. 2.8a. This dependence even survives phase averaging since it is caused by the difference in the time spent by the atom in the excited state $|e\rangle$. Because spontaneous emission tends to reduce the magnitude of the ARP force, the reduction must be

larger when the atom spends most of its time in $|e\rangle$. This is difficult to see in the Bloch sphere trajectories because they are complicated and depend strongly on the laser parameters.

In the up-up case, the frequency sweep begins below atomic resonance by δ_0. In the rest frame of an atom in $|g\rangle$ moving with positive velocity in the direction opposite to the k-vector of the first pulse of a pair, the initial frequency of the field is Doppler shifted upward. The light is initially closer to resonance than δ_0 and the atomic state is driven quickly toward $|e\rangle$ near the beginning of the pulse, and spends the majority of the pulse duration in the upper hemisphere of the Bloch sphere, eventually approaching the north pole. The frequency sweep for the following pulse also begins below resonance but it propagates in the opposite direction so that the atom experiences light with a downward Doppler shift. The initial frequency is further below resonance than δ_0 so that the atom dwells longer in the northern hemisphere of the Bloch sphere before being driven downward toward $|g\rangle$. Therefore, after two pulses with consecutive sweeps in the same direction, an atom moving with positive velocity spends most of its time in $|e\rangle$ (upper hemisphere) and thus experiences a weaker ARP force.

By contrast, if an atom's velocity is negative, then the Doppler shifts are reversed and the atom spends most of its time in $|g\rangle$ resulting in a stronger ARP force. When the two sweeps of a pulse pair have opposite directions the longer time spent in $|e\rangle$ during one pulse is compensated by the shorter time spent in $|e\rangle$ during the other one, restoring the symmetry with respect to velocity direction, as shown in Fig. 2.8b.

2.4 Velocity Capture Range

Forces suitable for laser cooling must have significant strength at some velocities and vanish at others. This is the only way for atoms that are initially spread in velocity space to be compressed into the region at the boundary where the force vanishes. The utility of

such forces depends on their range and strength where they're finite, and the steepness of their falloff where they vanish. Thus the velocity capture range (v_c) is one of the important parameters for characterizing laser cooling forces.

For the radiative force in the low intensity limit, $v_c \approx \gamma/k$ and is entirely dependent on the atomic properties. By contrast, the ARP force remains large for velocities where the Doppler shifts are well within the range of the frequency sweep. This means that velocity capture range for the ARP force, $v_c \sim \delta_0/k$, can be substantially increased by choosing δ_0 to be larger than γ so that it can be orders of magnitude larger than that of the radiative force. Furthermore, the velocity capture range is not determined only by atomic properties, and in principle can be applied to different atomic species with optical transitions within the range of the sweep.

The results of our calculations of the velocity capture range for the ARP force in the presence of spontaneous emission and "up-up" sweep sequences are presented in Fig. 2.9 as a function of δ_0 and Ω_0. The figure confirms that the amplitude of the frequency sweep, δ_0, is the most important parameter in defining v_c. It also shows that the ARP force remains effective (*i.e.*, half of the $v = 0$ value), at velocities up to $\sim \delta_0/3k$. In particular, the ARP force with $\delta_0 = 4.5\,\omega_m$, where $\omega_m = 100\,\gamma$, means that $v_c \sim 150\,\gamma/k$, which is two orders of magnitude larger than the capture range of the radiative force. Such a broad velocity capture range of the ARP force removes the need for the Doppler compensation that is required for most beam-slowing schemes [12].

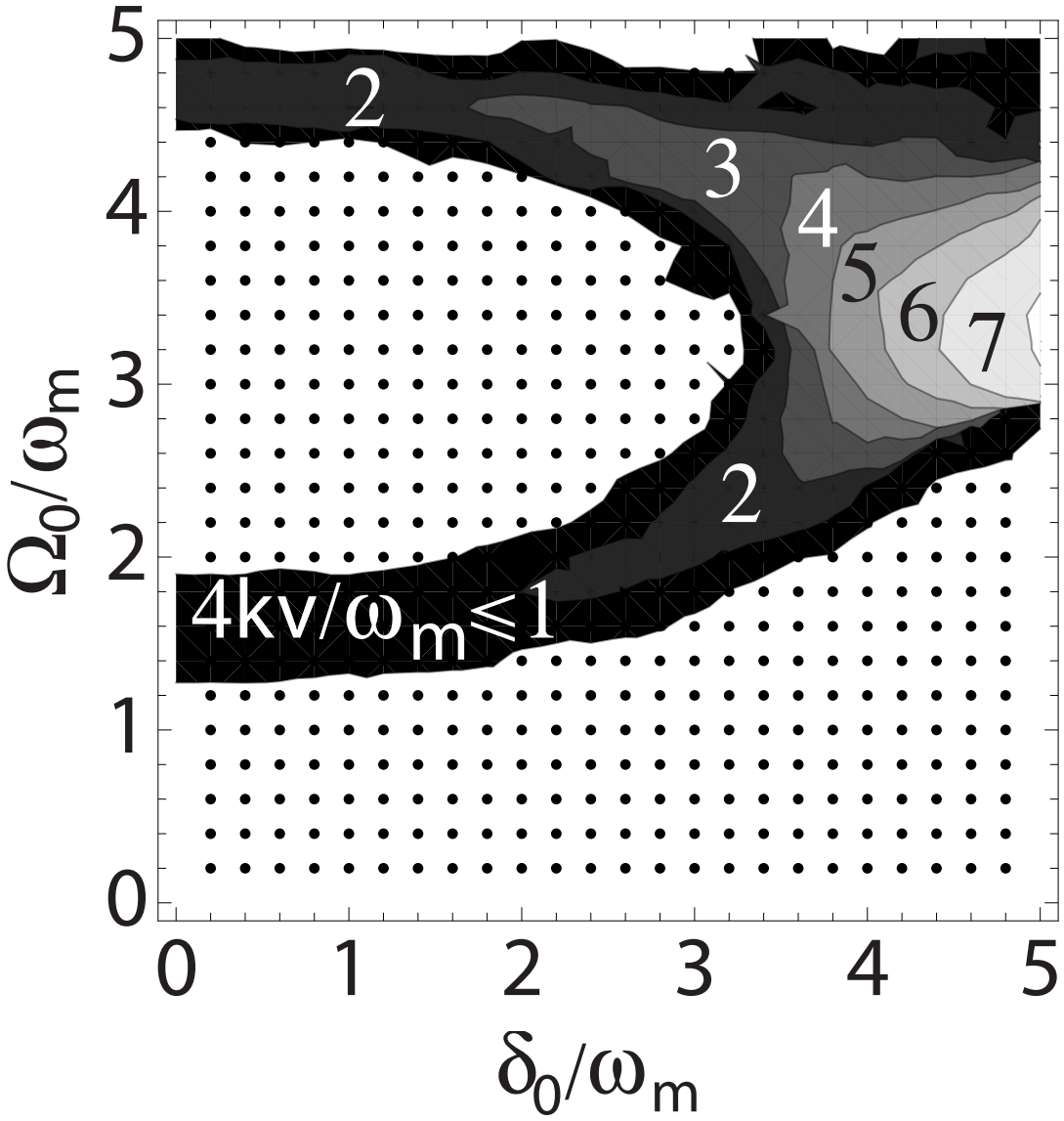

Figure 2.9: The shaded area shows the parameter values where the force exceeds $F_{ARP}/6$ (in the dotted region the force is always very small as shown in Fig's. 2.3e and 2.3f). Each succeeding lighter area indicates a region where the force exceeds $F_{ARP}/6$ for the indicated velocity. The velocity increment between regions is $\omega_m/4k$ up to $v = 7\omega_m/4k$ in the white region at the right edge. Since $\delta_0 \sim 4.5\omega_m$ in this region, the velocity is well in excess of $\delta_0/3k$.

Chapter 3

Numerical Simulations

The purpose of the numerical simulations presented in this chapter is to explore slowing (and perhaps cooling) of atomic beams via the ARP force. I will first motivate why slowing and cooling of atomic beams is of great interest. This will be followed by a description of the model used in these simulations. The rest of the chapter will be dedicated to results of these numerical simulations under various operating parameters and their implications.

3.1 Motivation

Small, portable, cold atomic samples have enormous potential for use in a fully integrated quantum mechanical device like a clock [33, 34] or inertial sensor [35, 36]. A significant challenge to this realization is the d^6 scaling of the atom number with the size of an atomic trap, where d is the diameter of the trapping light beams [37]. A decrease in atom-number reduces the signal to noise ratio (SNR) and will preclude evaporative cooling to produce ultracold temperatures (below the recoil limit) if the trap density is too low [12]. These atom traps have slow loading rates and a relatively small number of atoms. Loading times

of > 1 s are needed for sufficient atom number to create Bose-Einstein Condensation in many small atom traps [38]. Faster loading rates will increase SNR over a finite observation time. A way to alleviate these problems is to use laser cooling on an atomic beam. The most common methods to date for laser cooling rely on velocity dependent absorption and spontaneous emission.

Many paths to cold atoms rely on the magneto-optical trap (MOT) as a means to hold the atoms in place so that stages of laser and evaporative cooling may be applied to reach ultracold temperatures [12]. However, it is well known that the number of atoms loaded into a MOT from a thermal vapor scales strongly with the size of the trapping light beams [39–41]. It has been shown that the steady-state number of atoms in a MOT, $\mathrm{N}_{SS} \propto d^{3.6}$, where d is the diameter of the trapping beams, for trapping volumes greater than ~ 1 cm^3 [40, 41]. However, experiments on mm-scale traps show a stronger scaling, with $N_{SS} \propto d^6$ [37].

In an atomic-beam-loaded MOT, a counter-propagating laser beam will slow fast atoms below the capture velocity of the MOT to amplify the number of trapped atoms [42]. The changing Doppler shift associated with the slowing of the atomic beam may be compensated for by a spatially varying magnetic field [15] or by chirping the frequency of the slowing laser [43]. The length required to stop a thermal atomic beam is v_{max}^2/a_{max} [12]. Here v_{max} is the maximum atom velocity to be stopped and a_{max} is the maximum radiative force $\hbar k\gamma/2$ divided by the atomic mass ($1/\gamma \equiv \tau$ the lifetime of the excited state). For the alkali-metal atoms this sets the stopping length to ~ 1 m. Radiative force cycles rely on spontaneous emission to return the atoms to the ground state so that it may be re-excited by the slowing beam. Very many of these cooling cycles ($\sim 10^4$) are needed to stop a thermal atomic beam. The stopping length is dramatically decreased with the use of stimulated forces, thereby decreasing the size of the apparatus.

The bichromatic force uses stimulated emission in a standing wave to scatter photons at

a rate much faster than $\gamma/2$ [23–25]. This force also has the additional benefit of exerting these strong forces over a large range of velocities [19, 44]. It has been show that bichromatic slowing of a Rb beam increased atom-number and loading rates for a MOT by more than an order of magnitude when compared to MOT loading without bichromatic slowing [45].

The velocity dependence of radiative force in the low intensity limit, $v_c \approx \gamma/k$ is entirely dependent on the atomic properties. By contrast, the ARP force remains large for velocities where the Doppler shifts are well within the range of the frequency sweep. This means that velocity capture range for the ARP force, $v_c \sim \delta_0/k$, is substantially increased by choosing δ_0 to be much larger than γ so that it is much larger than that of the radiative force. Furthermore, the velocity capture range is not determined only by atomic properties, but also upon experimental parameters. Figure 2.5c shows the ARP force as a function of atomic velocity for a given Ω_0 and δ_0. Here the force stays greater than half its maximum for all $v < \pm\delta_0/3k$. With this motivation in mind, I will now introduce our model for simulating the slowing of an atomic beam via the ARP force.

The potential benefits of ARP on the slowing of neutral atoms may also be applied to molecules as well. There is considerable interest in the production of samples of ultracold molecules for applications in quantum computation [46, 47], quantum simulation of condensed matter systems [48–50], precision measurements [51–54], controlled chemistry [55], and high precision spectroscopy [56]. The crucial step is to bridge typical molecular source velocities ($\sim 150 - 600$ m/s) and velocities for which trap loading or confinement is possible ($\leq 5 - 20$ m/s) [57]. Spontaneous decays to many different ro-vibrational states has been a significant hindrance to the direct laser cooling of molecules to ultracold temperatures. With its decreased reliance on spontaneous emission, ARP may be a suitable candidate for laser cooling and slowing of molecules. For these reasons it is advantageous to explore the properties of the ARP force via numerical simulations.

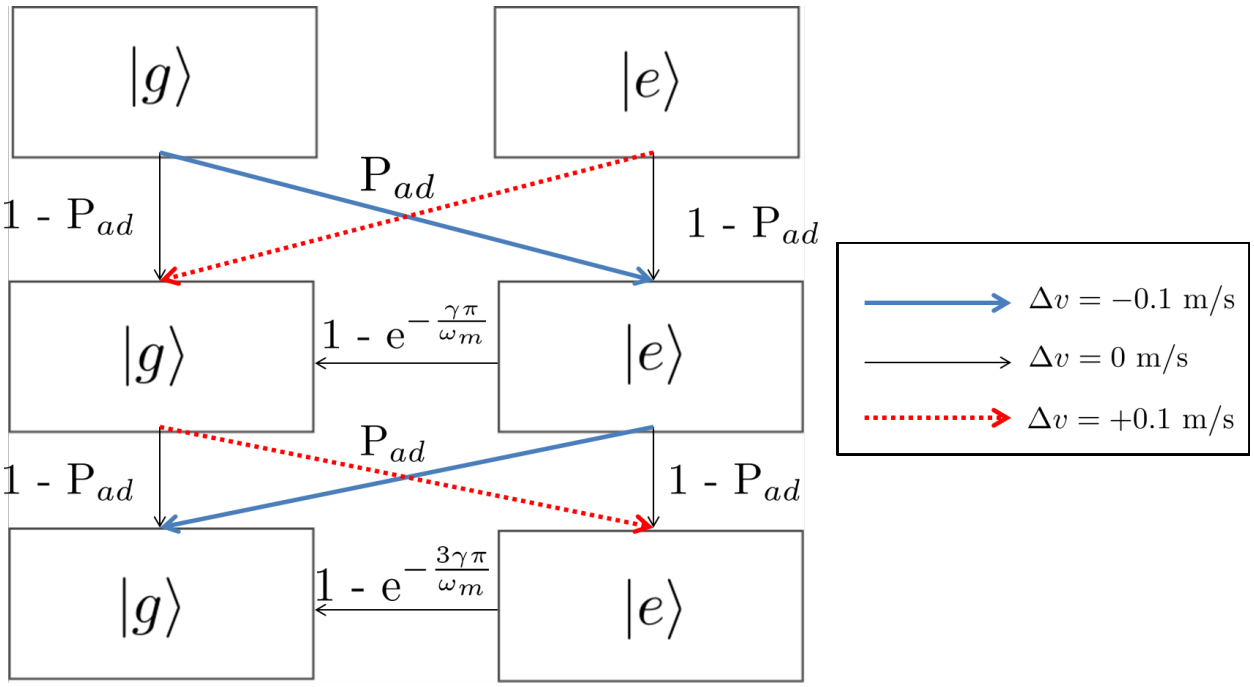

Figure 3.1: Graphical depiction of model for a single sequence of adiabatic rapid passages with spontaneous emission for numerical simulations. P_{ad} is the probability of an adiabatic transition, ω_m is the modulation frequency, γ is the spontaneous emission rate, and Δv is the velocity change for a single recoil. See text for further description.

3.2 Model

Semi-classical numerical calculations were performed to simulate the longitudinal interaction of an atomic beam with a series of periodic adiabatic rapid passage sequences over a finite interaction time. The atomic beam consists of 5,000 atoms unless otherwise noted. The initial longitudinal velocity of a single atom is a pseudo random number from a Maxwellian distribution centered at $v = 1050$ m/s, a FWHM of 520 m/s, and zero transverse velocity. A flow chart of the model used for a single ARP sequence can be seen in Fig. 3.1.

A single ARP sequence consists of counterpropagating ARP pulses separated in time with a finite amount of time where there is no light interacting with the atom as shown in Fig. 2.2. The first pulse in each sequence is labeled L, and the second pulse R. Each pulse

has some finite probability P_{ad} to transfer a single atom between two states, labeled $|g\rangle$ and $|e\rangle$. An atom initially in $|g\rangle$ will go to $|e\rangle$ with a probability P_{ad}, and an atom initially in $|e\rangle$ will go to $|g\rangle$ with a probabilityP_{ad}. If pulse L (R) drives the atom from $|g\rangle \rightarrow |e\rangle$ ($|e\rangle \rightarrow |g\rangle$), then the atoms velocity will change by - 0.1 m/s. If pulse L (R) drives the atom from $|e\rangle \rightarrow |g\rangle$ ($|g\rangle \rightarrow |e\rangle$), then the atoms velocity will change by + 0.1 m/s.

The effects of spontaneous emission may be taken into account in this model as well. If the atom is in state $|e\rangle$, there is some probability the atom will return to state $|g\rangle$ before interacting with the next ARP pulse. That probability for the atom to return to the ground state is $1-e^{-\gamma t}$, where γ is the spontaneous emission rate and t is the time between pulses. In this simple model there is no momentum kick associated with spontaneous emission. Using the timing sequence in Fig. 2.2, the time between L and R in a single sequence is π/ω_m, and a time of $3\pi/\omega_m$ between R of one sequence and L of the next.

It is also possible to include the velocity dependence of the ARP force by making P_{ad} velocity dependent that can vary the width of the atomic velocity distribution. Broadening of the velocity distribution is characteristic of heating, and narrowing of the velocity distribution is characteristic of cooling.

3.3 Effect of Spontaneous Decay and Moving Atoms

This section will discuss the effects of spontaneous emission and P_{ad} on the ARP force. As shown in Sec 2.3, the ARP force decreases by a factor of ~ 2 in the presence of spontaneous emission for interaction times much longer than the excited state lifetime. To mitigate this effect, all simulations without spontaneous emission use 5,000 pulse pairs, and simulations with spontaneous emission use 10,000 pulse pairs. Motivated by experimental values, the spontaneous emission rate is chosen to be $\gamma = \omega_m/100$. This leads to an interaction time

with spontaneous emission of $\sim$ 800 lifetimes.

To begin with, consider the case of perfect ARP (P_{ad} =1) with and without spontaneous emission. Fig. 3.2 shows that spontaneous emission has very little effect on final atomic velocities when compared to the simulation with no spontaneous emission. The widths of the initial and final velocity distributions are very nearly the same in both plots. Without a velocity dependent force, the ARP force is unable to cool a sample, but it is possible to cause heating. Since the width of the velocity distribution is related to the temperature of the sample, we may infer that perfect ARP, with and without spontaneous emission, does little to change the temperature of the sample.

Variations in experimental parameters (intensity, atomic velocity, frequency sweep, etc.) lead to imperfect ARP ($P_{ad} \neq 1$). Such small imperfections can rapidly lead to a dramatic decrease in the ARP force over time as these errors may compound themselves. Fig. 3.3 shows the effect of imperfect ARP with and without spontaneous emission over 10,000 and 5,000 pulse pairs respectively. This figure shows that without spontaneous emission, even a 1% error makes the ARP force very ineffective. The final atomic velocity is very nearly the initial atomic velocity. However, with spontaneous emission, a 1% error in a single ARP only reduces the force by $\sim$ 15%. A 4% error in a single ARP only reduces the force by $\sim$ 50%. As in the previous figure, it should also be noted that the width of the velocity distributions are relatively unchanged so little heating or cooling is observed.

It may seem counterintuitive that spontaneous emission, an incoherent process, should have such a profound positive effect on a coherent process such as ARP. Fig. 3.4 shows how quickly the ARP force deteriorates when a small imperfection is present (P_{ad} = 0.99) and spontaneous emission is turned off. The simulation begins with 500 atoms at zero velocity. For 250 pulse pairs and perfect ARP with $\Delta v = -0.1$ m/s, a final velocity of - 50 m/s for all 500 atoms would be expected. Fig. 3.4a shows the atomic velocity distribution after 250

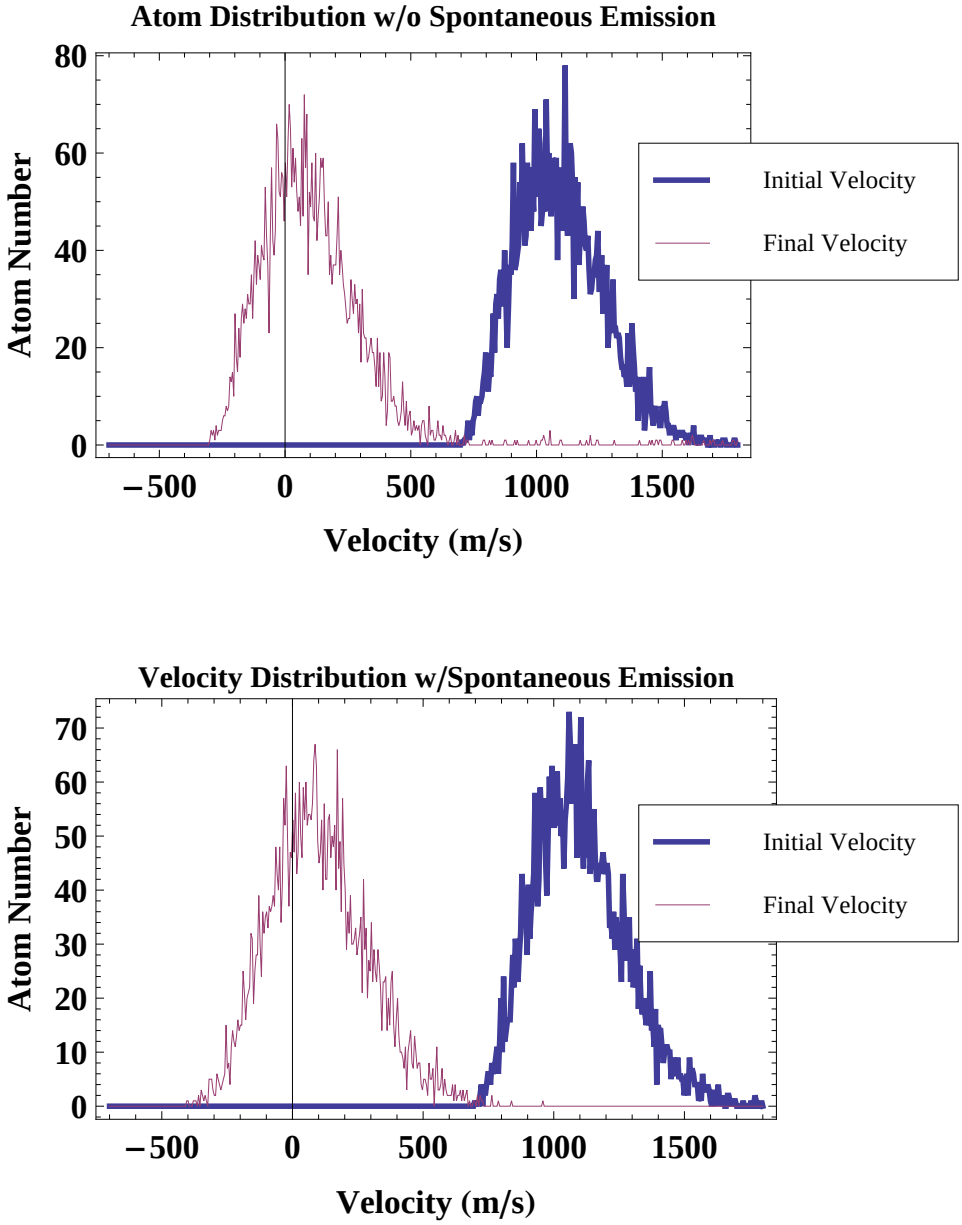

Figure 3.2: The effect of of spontaneous emission on the ARP force. The top plot shows 5000 pulse pairs acting on a velocity distribution without spontaneous emission. The bottom plot shows 10000 pulse pairs acting of the same ensemble with $\omega_m = 100\gamma$.

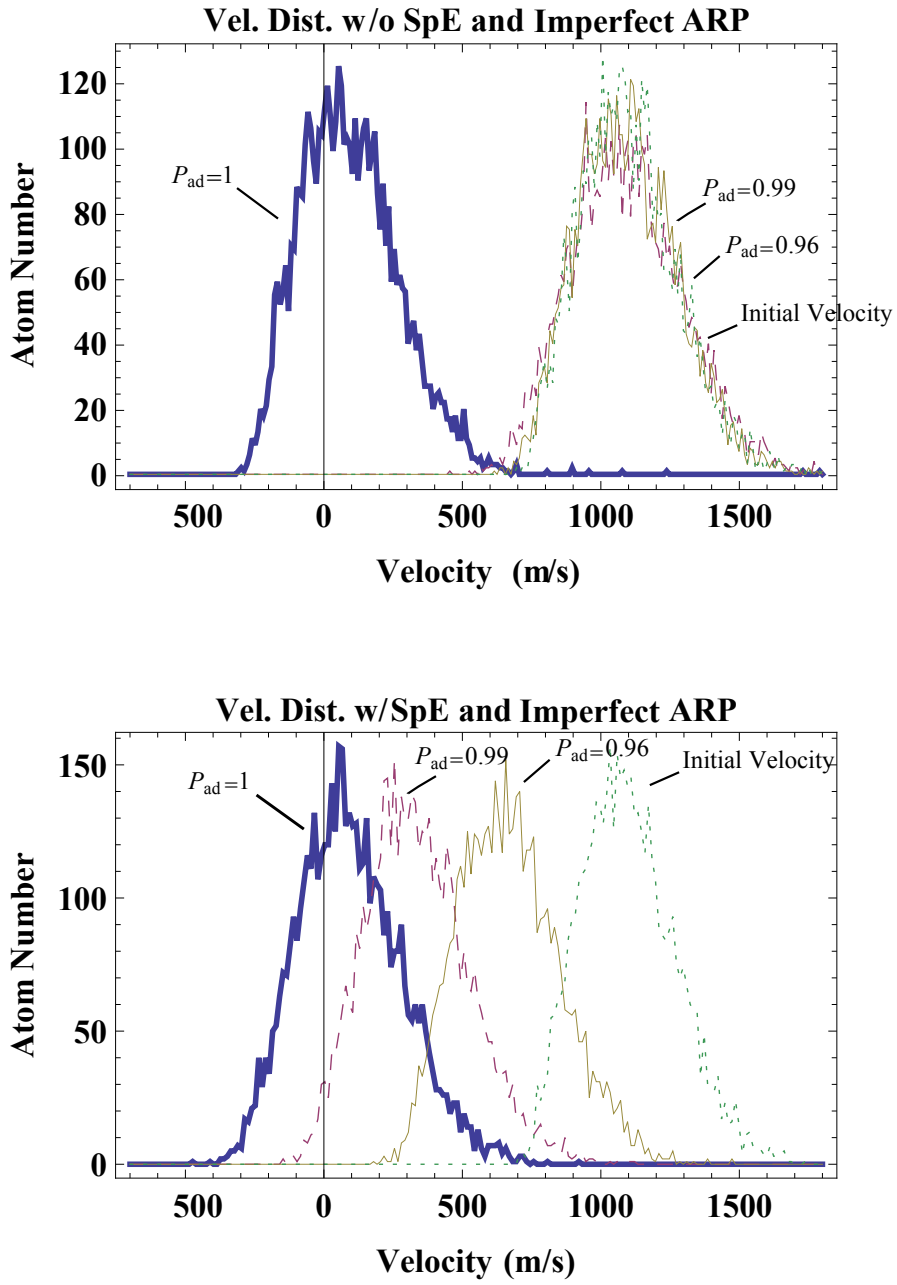

Figure 3.3: The effect of of imperfect inversion on the ARP force. The top plot shows 5000 pulse pairs acting without spontaneous emission for $P_{ad} = 1$, 0.99, and 0.96. The bottom plot shows 10000 pulse pairs acting of the same ensemble and $\omega_m = 100\gamma$.

pulse pairs for $P_{ad} = 0.99$. This figure shows that a 1% error in a single ARP leads to an average velocity of only - 5 m/s and a width of $\sim$ 50 m/s. Fig. 3.4b shows how the average final velocity of the ensemble varies with the number of pulse pairs for imperfect ARP. According to this figure, the average velocity levels off at $\sim$ - 5 m/s after 50 pulse pairs. After 50 pulse pairs (100 pulses) there should be almost as many atoms in the ground state as the excited state if there is a 1 % error for a single pulse. As a consequence, any additional pulse pairs will not increase the mean of the velocity distribution. The width of the distribution will increase over time as additional pulse pairs cause a random walk in velocity space. Though imperfect ARP may heat an ensemble of atoms in this example, imperfect ARP can be used to cool atoms under the right conditions.

The velocity dependence of an optical force plays a critical role in determining its utility for laser cooling. Fig. 3.5 shows that ARP may be suitable for the cooling of an atomic sample. It is required to know the velocity dependence of P_{ad} to study the velocity dependence of ARP in this model. Fig. 3.5a shows a numerical calculation of P_{ad} as a function of atomic velocity for a single pulse with parameters $\delta_0 = 3.0\,\omega_m$ and $\Omega_0 = 4.4\,\omega_m$ (Plot b in Fig. 2.5). The velocity frame is centered at 1050 m/s to match the peak of the initial atomic velocity distribution. Also shown in this figure is a Gaussian fit to P_{ad} to be used in the numerical simulation that is nearly perfect between the velocities of 0 and 2000 m/s and has a $1/e$ width of $\pm$ 795 m/s.

With $P_{ad}(v)$ from the Gaussian fit, numerical simulations of 2,000, 6,000, and 10,000 pulse pairs are carried out upon an atomic ensemble containing 5,000 atoms with a Maxwellian velocity distribution (most probable velocity of 1050 m/s and a velocity spread of $\pm$ 260 m/s). The final velocity distribution in Fig. 3.5b shows both slowing and significant velocity compression. The peak final velocity for $\sim$ 750 m/s and the velocity spread is $\sim \pm$50 m/s. The ARP force reduces the peak atomic velocity by $\sim$ 25% and reduces the velocity spread

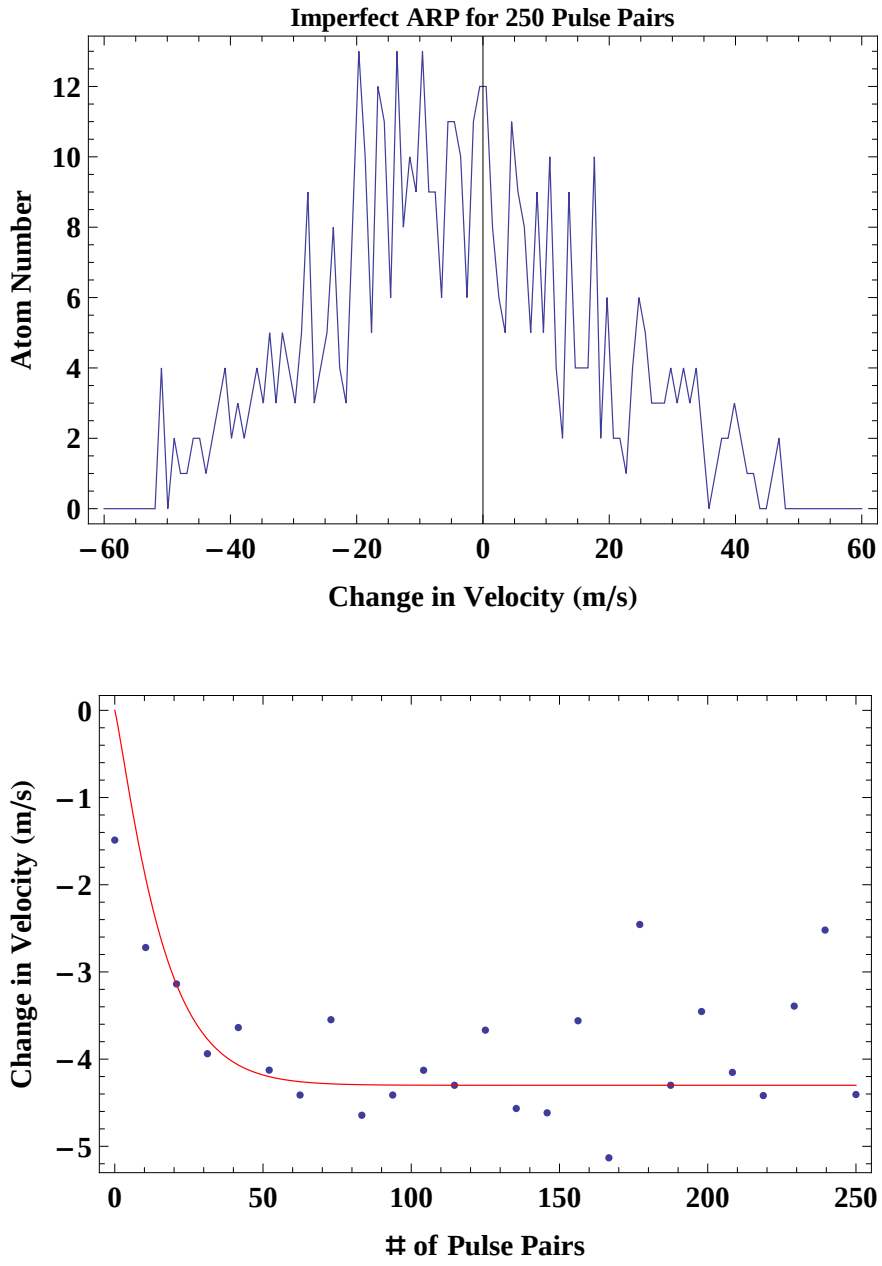

Figure 3.4: Imperfect ARP without spontaneous smission. The top plot shows, for 500 atoms starting at $v = 0$, their velocity after 250 pulse pairs with $P_{ad} = 0.99$ and no decay. The bottom figure shows how the average velocity of the ensemble varies with the number of pulse pairs. The average velocity levels off at $\sim$ - 5 m/s after 50 pulse pairs.

by $\sim$ 80%. Reducing the velocity spread by a factor of 5 is equivalent to reducing the temperature of the ensemble by a factor of 25. It should also be noted that there are very few atoms with velocities $>$ 1000 m/s for 10,000 pulse pairs. From this observation it can be concluded that the ARP force can slow and cool atoms over a wide range of velocities.

The total interaction time for 10,000 pulse pairs in this simulation is $\sim$ 1250 lifetimes for $\omega_m = 100\gamma$. If the ensemble was under the influence of a constant radiative force, each atom would have received at most 300 velocity recoils in that same interaction time (see Eq. 1.16). The resulting change to the atomic velocity would be $\sim$ 30 m/s. For the chosen parameters, the ARP force is $\sim$ 10 times greater than the maximum radiative force and shows significant cooling.

Magnetic and optical trapping of neutral atoms is used in many areas of atomic physics such as high resolution precision spectroscopy, collision studies, Bose-Einstein condensation, and atom optics [12]. However, atoms traveling at high velocity that do not come to rest by the end of the trapping region cannot be trapped. Typical velocity capture ranges for magneto-optical traps are of the order 10-100 m/s. It would then be desirable to discover under what circumstances the ARP force could slow an atomic beam to a velocity that most atoms could be trapped.

The amount of beam slowing capable of being produced by the ARP force depends on the width of the force vs. velocity distribution ($\sim \delta_0/k$) and the interaction time. The ARP force in Fig. 3.5b with $\delta_0 = 3.0\ \omega_m$, $\Omega_0 = 4.4\ \omega_m$, and $\omega_m = 100\gamma$, reduces the peak atomic velocity by $\sim$ 25% for an interaction time of 1250τ. One way to increase the rate and magnitude of slowing is to increase ω_m from 100γ to 400γ, resulting in an increase of the magnitude and velocity range of the ARP force by a factor of 4. Fig. 3.6 shows an atomic beam with 5000 atoms can be slowed to $\sim$ 75 m/s in a time of 1000τ, via the ARP force with $\delta_0 = 3.0\ \omega_m$, $\Omega_0 = 4.4\ \omega_m$, and $\omega_m = 400\gamma$. The interaction time corresponds to 32,000

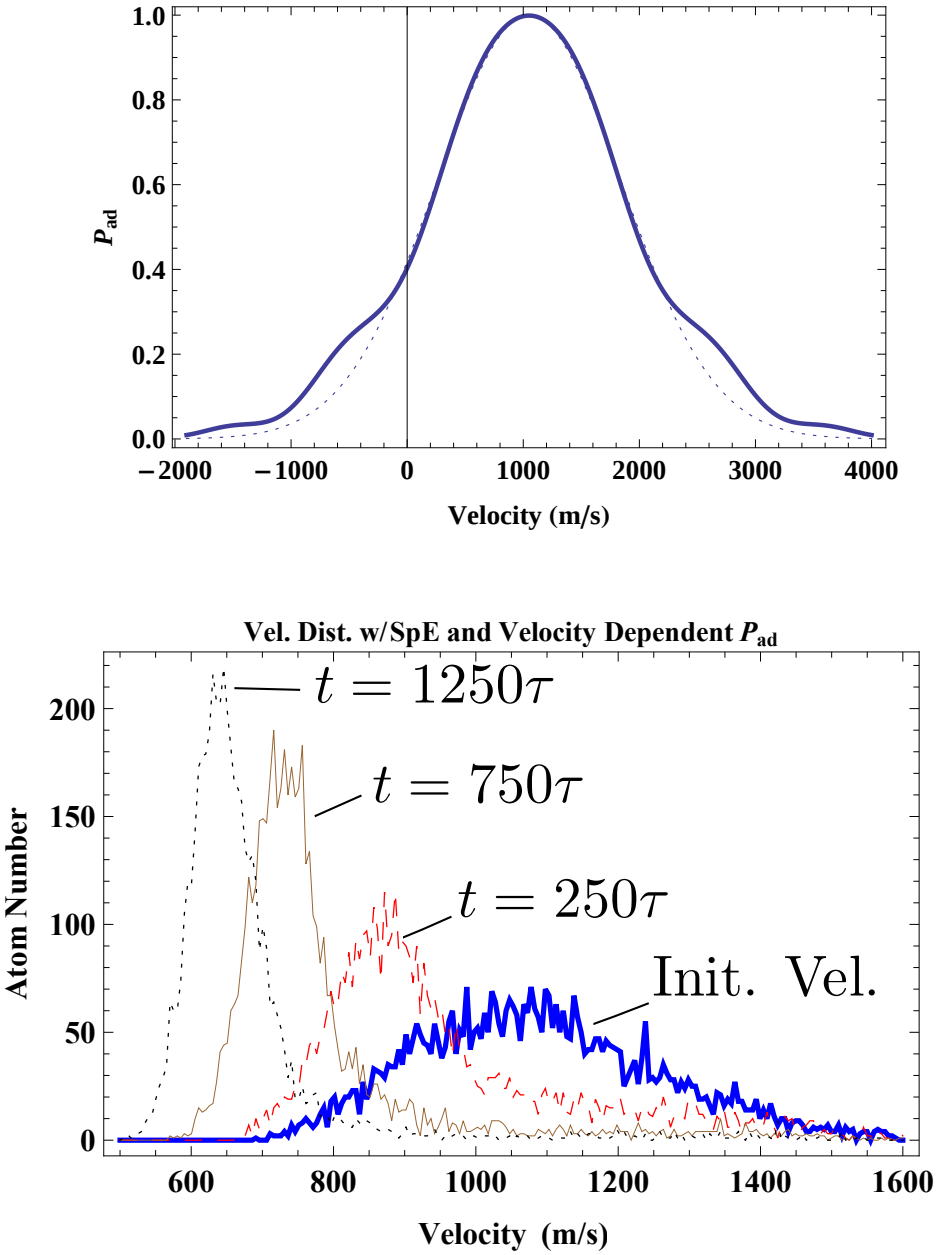

Figure 3.5: Longitudinal slowing of an atomic beam. Shown at the top is $P_{ad}(v)$ for ARP with $\delta_0 = 3.0\ \omega_m$ and $\Omega_0 = 4.4\ \omega_m$ (solid line) and a Gaussian fit to the distribution (dotted line). The bottom figure shows the result of 8000 pulse pairs acting on 5000 atoms using the Gaussian fit for $P_{ad}(v)$ from the top. The ensemble is slowed by $\sim 25\%$ and its temperature is reduce by more than an order of magnitude.

pulse pairs with an average force ≈ 40 times the maximum radiative force.

The width of final velocity distribution in Fig. 3.6 is roughly 4 times larger than that of Fig. 3.5b. The steady state temperature of a sample acted upon by a damping force should be proportional to the ratio of the diffusion rate to the damping rate [12]. The damping rate of a force is proportional to F_{Max}/v_c which does not depend on ω_m. The diffusion rate, however, should depend on ω_m as a single spontaneous emission event will reverse the sign of the ARP force for many cycles until another spontaneous emission event restores the correct sign to the force. The number of cycles it will take for the force to be corrected (and hence the diffusion rate) will therefore be proportional to ω_m.

It should also be noted that the beam is slowed over a distance of ≈ 5 cm in a time of ≈ 100 μs, both of which are more than an order of magnitude less than slowing distances and slowing times achievable via the radiative force. Most of the atoms in the resultant velocity distribution could be trapped by a traditional magneto-optical trap.

Adiabatic Rapid Passage has many potential advantage over traditional beam slowing techniques. The average force can be more than an order of magnitude larger while still reducing the temperature of the ensemble. The shorter interaction time required to stop an atomic beam also decreases the amount of distance required for the slowing apparatus. It should also be noted that this laser cooling is done without the aid of any spatially dependent magnetic field found in most slowing apparatuses. Also, the use of the ARP force significantly decreases the number of unwanted spontaneous emission events. Spontaneous emission causes heating in all dimensions via random walk and the atom may result in decay to a dark state that will disrupt the cooling cycle. I will now describe the apparatus used to create and image a metastable helium beam for our experiments using the ARP force .

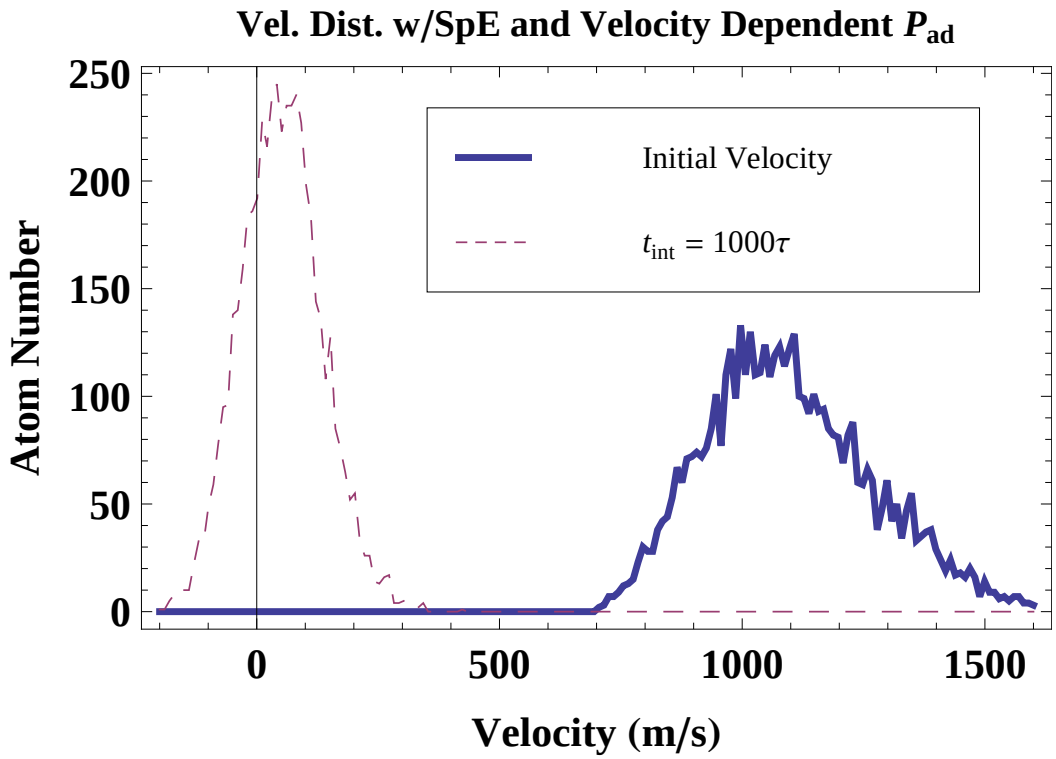

Figure 3.6: Longitudinal slowing of an atomic beam to zero velocity. The bottom figure shows the result of 8000 pulse pairs acting on 5000 atoms using the Gaussian fit for $P_{ad}(v)$ from the top. The ensemble is slowed to an average velocity of ~ 75 m/s and its temperature is reduced by roughly a factor of 4.

Chapter 4

Metastable Helium Apparatus

The $2^3S_1 - 2^3P_2$ transition in helium is an ideal choice for experiments using adiabatic rapid passage. Various important properties and the relevant energy levels for this transition can be found in Table 4.1 and Fig. 4.2 respectively. The transition wavelength of ~ 1083 nm allows the use of fiber-coupled electro-optical modulators and optical fiber amplifiers that are discussed in 5. The lifetime of the 2^3P_2 electronic state is relatively long compared to most laser cooling transitions which helps satisfy the rapid condition for ARP. The relatively low saturation intensity also helps by making it easier to at least partially satisfy the adiabatic condition for ARP. Finally, the energy levels of the 2^3P are well separated and thus make the two level atom approximation valid in the context of the experiments to be discussed in this thesis. This chapter will discuss the vacuum system used in the production and detection of metastable helium (He*) after a transverse interaction with ARP light.

A top view schematic of the vacuum system can be seen in Fig. 4.1. First I will discuss the components of the beamline. Then a discussion of how the metastable helium beam is produced by a reverse flow DC discharge source (A in Fig 4.1). This will be followed by details of how the atomic beam travels inside a stainless steel vacuum system before

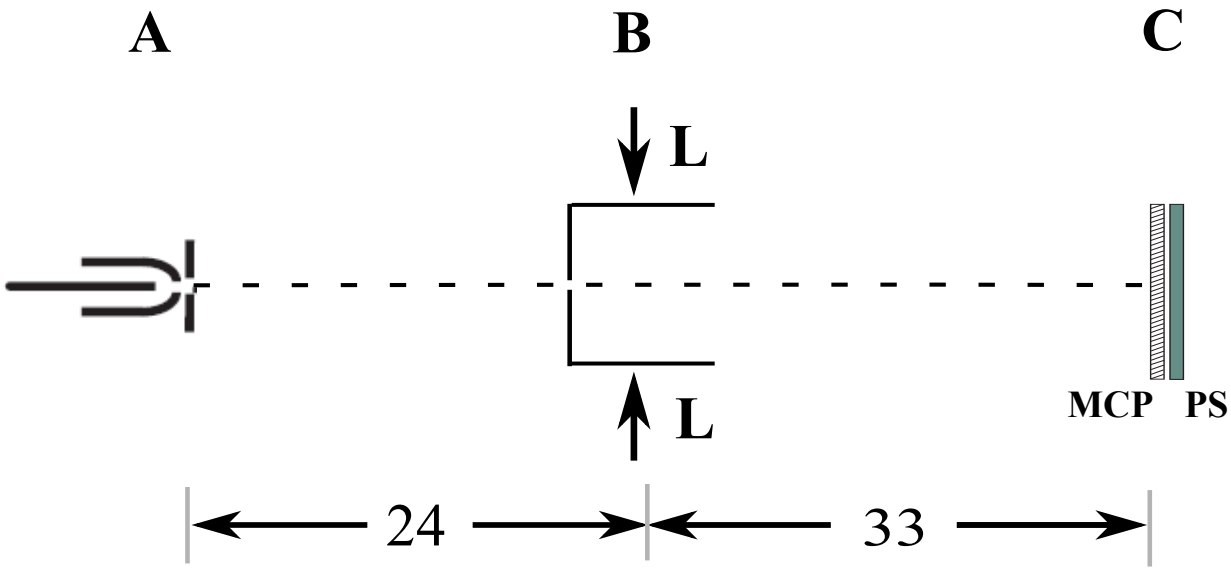

Figure 4.1: A top view schematic of the atomic beam setup which show the positions of the source, interaction, and detection regions (A, B, and C respectively). The counterpropagating laser beams (L) cross the atomic beam (dashed line) at right angles. All dimensions are in cm.

Quantity Units	λ (nm)	$\hbar\omega_a$ (eV)	τ (ns)	$\gamma/2\pi$ (MHz)	I_{sat} (mW/cm^2)	$\omega_r/2\pi$ (kHz)
	1083.33	1.144	98.04	1.62	0.17	42.46

Table 4.1: Values for the various properties of the $2^3S_1 - 2^3P_2$ Helium transition used in this experiment, taken from [12].

it is collimated by a narrow vertical slit and interacts with ARP light transversely (B in Fig 4.1). Lastly, there will be a discussion of the positional detection of the He* atoms by the combination of a multichannel plate (MCP) and phosphor screen (PS) (C in Fig 4.1).

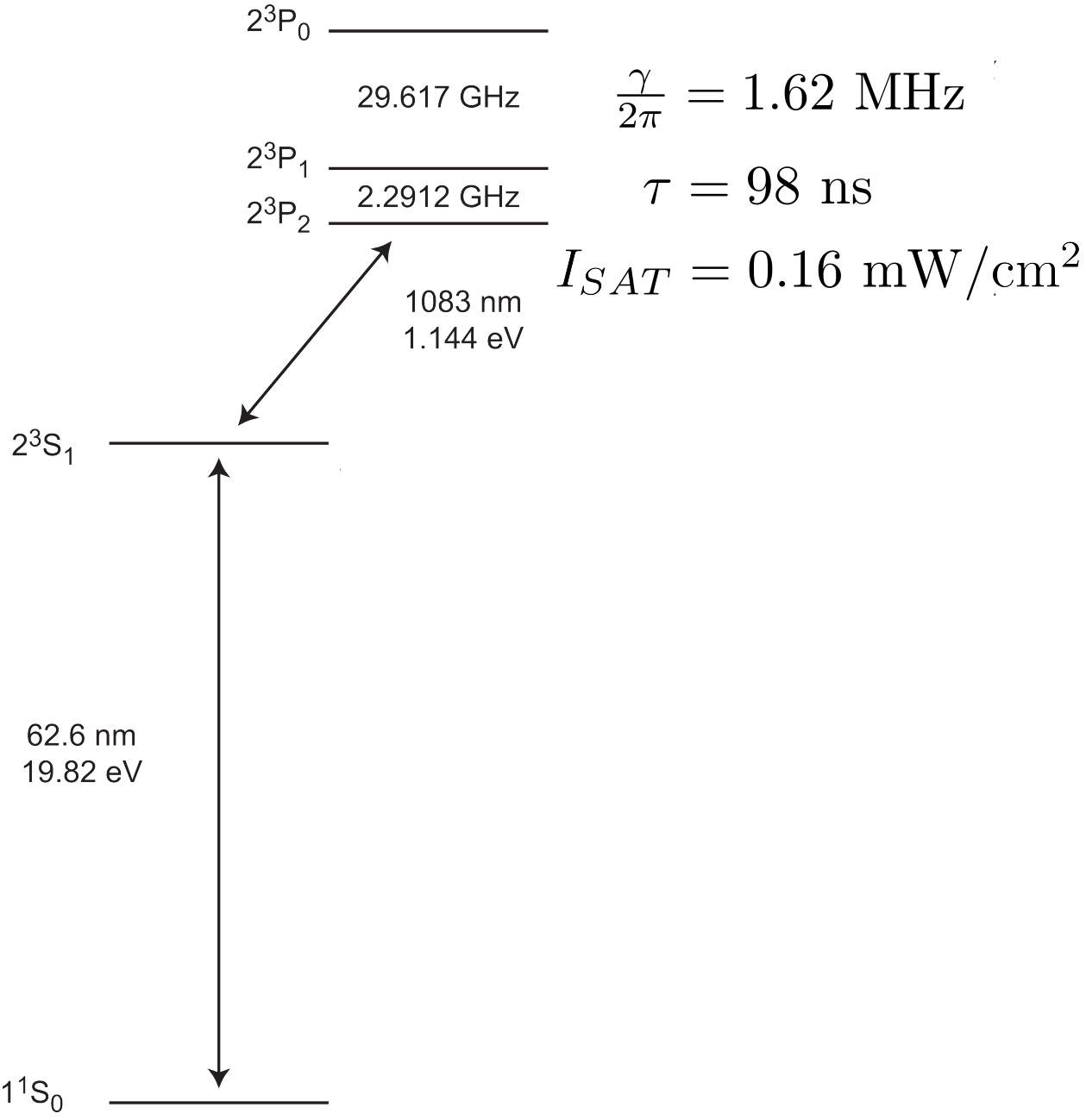

Figure 4.2: Relevant energy levels for the ARP experiments in helium. The lifetime of the metastable state 2^3S_1 is ~ 7900 s and serves as the "ground state" for our experiments [58].

4.1 Metastable Helium Beamline

The metastable He beamline can be broken into three distinct sections: source, interaction, and detection chambers. A schematic of the vacuum system can be seen in Fig. 4.3. The interaction and detection chambers will be referred to as the beam chamber at times. The system consists mainly of 4 inch diameter cylinders of stainless steel with 6 inch copper sealed ConFlat flanges. The experiments described in this dissertation are carried out on a high vacuum (HV) chamber with a background pressure of $\sim 10^{-7}$ Torr measured by Lesker G100F ion gauges. The mean free path of the He* atoms is much longer than that of the length of the beamline due to the small collisional cross section even at HV pressures.

The source chamber opens into the interaction chamber through a 0.5 mm aperture (as described in detail below) which allows differential pumping between the two regions. The source chamber is pumped by a Pfeiffer TPH 330 turbo molecular pump backed by a Pfeiffer Duo 110 mechanical pump. These pumps must handle a large influx of helium gas when the source is running. The interaction and detection chambers are pumped by a separate Pfeiffer TPH 330 turbo molecular pump backed by a Welch 1376 mechanical pump. The detection region can be closed off from the interaction region by a copper-sealed gate valve. This allows for the changing of detector parts without the need to bring the entire beamline up to atmospheric pressure.

The vacuum system is protected from the back-streaming of oil in the event of a sudden power outage by foreline shut-off safety vent valves placed between the mechanical and the turbo molecular pumps. The Pfeiffer Duo 110 is protected by a Pfeiffer ONF 25 safety foreline valve, while the Welch 1376 pump has a Lesker auto-off safety vent valve. In both cases the valves remain open as long as the power is on and pressure on the mechanical pump side is lower than that of the fore-line. The valves will close within 30 ms in the event of a power

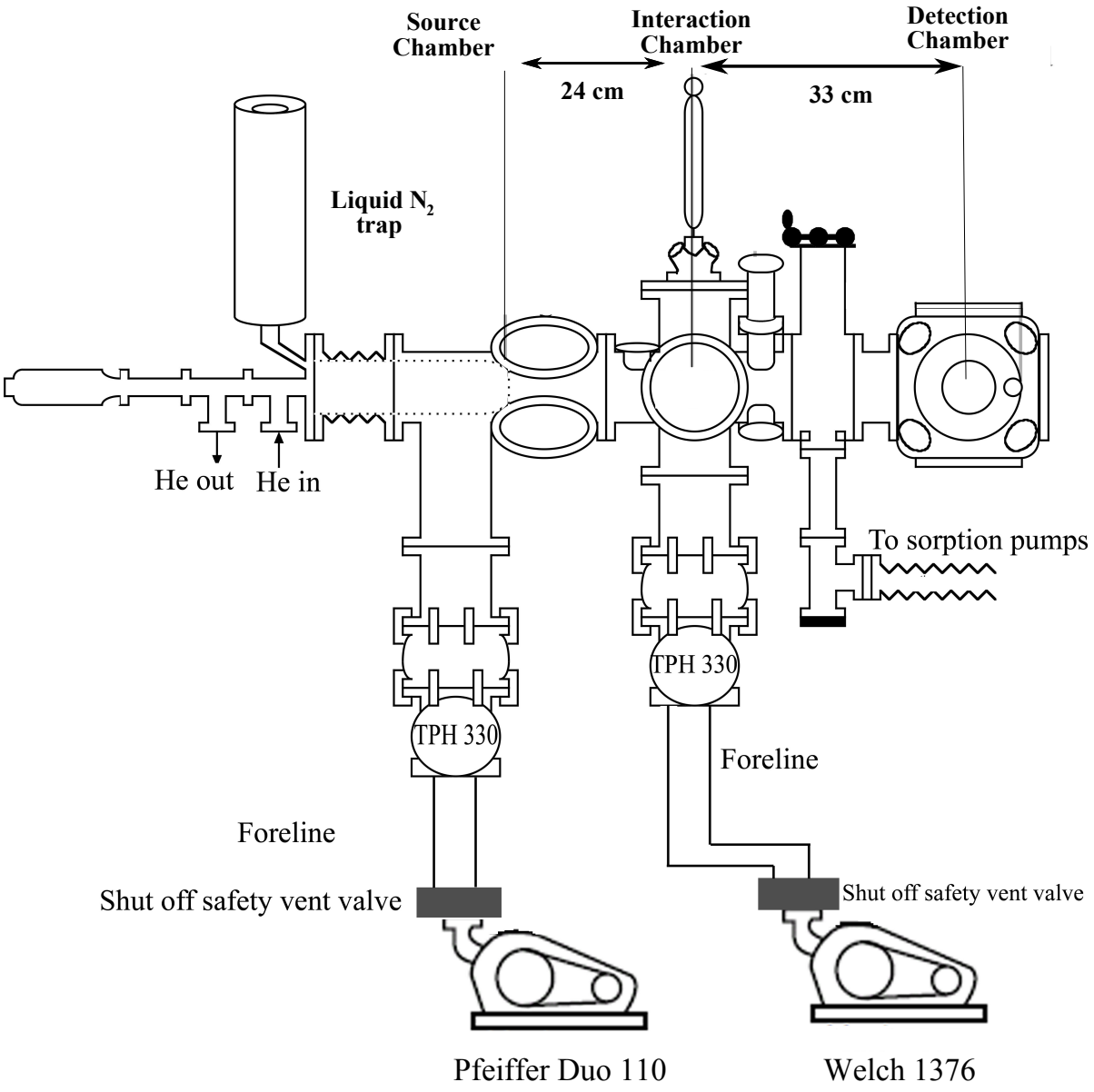

Figure 4.3: The vacuum system is divided into three distinct sections: source, interaction, and detection chambers. The system consists mainly of 4 inch diameter cylinders of stainless steel with 6 inch copper-sealed ConFlat flanges. Modified from [26]

outage and slowly vent to atmospheric pressure. The safety valves will not open the moment power has returned but only when the pressure on each side of the valve has equalized to prevent the back-streaming of oil into the vacuum system.

4.2 Metastable Helium Source

The optical transition $1^1S_0 \rightarrow 2^3S_1$ in helium is doubly forbidden by selection rules and is also at a wavelength where no simple laser exists. Therefore the production of metastable helium must be accomplished via some other method. The atomic beam source used in our laboratory is a reverse flow DC discharge designed modeled after the design of Shimizu [59], with modifications originated by Mastwijk *et al.*[60]. A diagram of the source can be seen in Fig. 4.4. Our source was originally built at Universiteit Utrecht and then assembled and tested at Stony Brook University in 1999.

The source consists of a 1 cm diameter glass tube mounted in the center of a 3 cm stainless steel jacket cooled by liquid N_2. The glass tube is held in place by a Teflon spacer between it and the jacket as well as an O-ring spacer near the input of the helium gas. Helium flows between the tube and the jacket towards the tip of the tapered glass tube. The helium gas is cooled as it comes into contact with the jacket.

A 1 mm diameter tungsten needle is placed inside the glass tube with its point toward the tapered end of the tube to serve as the cathode of the source. The anode is a grounded aluminum plate with a 0.5 mm aperture placed at the front end of the LN_2-filled jacket, called the nozzle plate. The distance between the tungsten needle and the nozzle plate can be adjusted by a linear feedthrough connected to the end of the rod holding the needle in place. A second plate, called the skimmer, with a 0.5 mm aperture is placed directly behind the nozzle plate. The skimmer plate geometrically defines the He* beam while also allowing

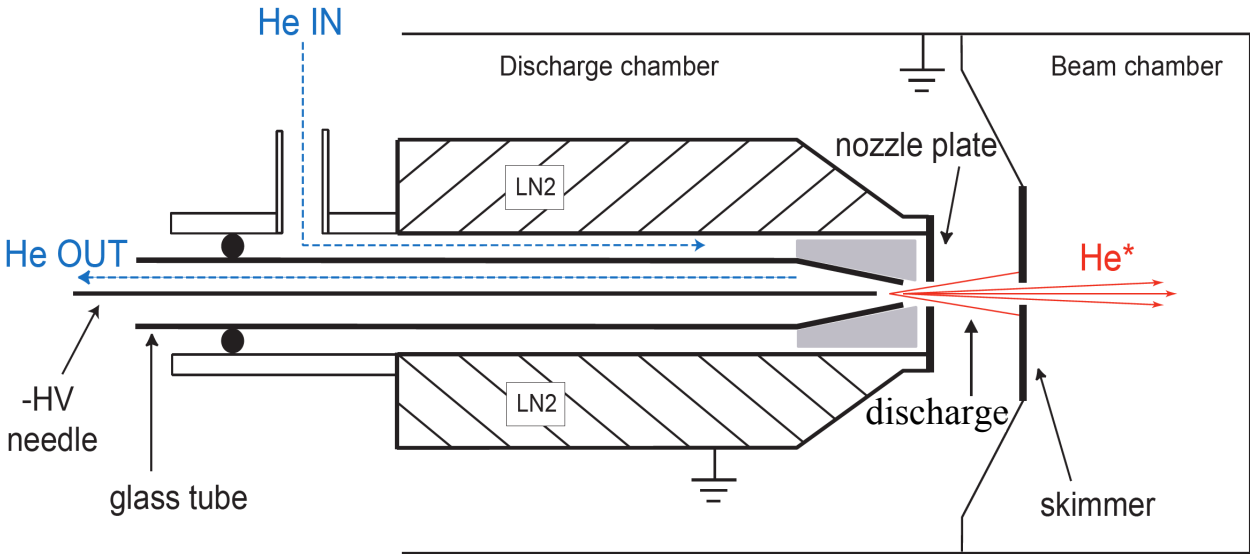

Figure 4.4: Top view schematic for DC discharge source for the production of metastable helium.

for differential pumping between the discharge chamber and the beam chamber. A Welch 1402 mechanical vacuum pump pulls the He gas though a small hole at the end of the glass tube and then pumps the gas out of the system. The typical outlet pressure is measured to be $\approx$ 1.10 Torr by an MKS Instruments convectron gauge and a Terranova 926 gauge controller. The remaining gas flow sustains a glow discharge between the needle and the nozzle plate when the needle is placed at a high negative voltage (typically -2200V provided by an HP 6525A). The plasma formed creates metastable He (2^3S_1) via electron impact or ion-electron recombination. A large fraction of the produced He* is immediately quenched by the collisions in the dense plasma. The He* atoms produced in the dilute afterglow of the discharge survive and fly through the skimmer plate aperture to define the beam line. The efficiency (measured by the number of metastable He atoms produced relative to the number of ground state He atoms flowing into the source chamber) of the source is quite low ($\sim 10^{-5} - 10^{-4}$). The source will also produce helium in the 2^1P state that decays quickly to the ground state with emission at 62.6 nm. This ultraviolet emission will serve

as an unwanted source of background in our measurements. Atoms are also produced in the 2^1S state with a lifetime of 19.7 ms (longer than the $\sim$ 1 ms flight time of the beam) [61]. These atoms will not interact with the ARP beams but will be detected by the MCP/PS as discussed later.

The source is very sensitive to the pressure in the discharge region and the voltage on the discharge needle. The discharge may run stably for discharge currents between 2 and 12 mA based on pressure and voltage. The choice of 6 mA for normal use is made as a trade-off between metastable production and source reliability and longevity. The source output flux is $\approx 10^{14}$ He* atoms/s·sr [62, 63]. The atoms have a roughly Maxwellian distribution of longitudinal velocities centered at $\sim$ 1000 m/s with a FWHM of $\sim$ 400 m/s as measured by time of flight [62].

4.3 Interaction Region

The source and skimmer protrude into a six-way Conflat cross that is directly welded onto the Tee of the source chamber. Four of these arms have windows ± 45 deg from the vertical with anti-reflection coatings for $\lambda = 1083$ nm and $\lambda = 389$ nm light. The purpose of this setup is to allow optical access to the He* beam as close as possible to the point at which the atoms emerge from the skimmer. This region is used in the experiments concerning the use of the bichromatic force to show cooling without spontaneous emission. It is not used in the ARP experiment.

The beam then arrives at another six-way cross oriented with arms in the vertical and horizontal directions. The atomic beam travels for 24 cm from the skimmer before impinging on a gold slit 250 μm wide by 1 cm tall as seen in Figure 4.5a. The vertical slit is required to geometrically define the atomic beam so the atoms have very little transverse velocity.

Behind the atomic slit is a small Helmholtz coil setup. The Helmholtz coils are designed to produce a homogeneous magnetic field along the optical axis of the ARP light (perpendicular to the atomic beam) for optical pumping (see Section 1.3). There were two important considerations that had to be made when placing the coils in the vacuum system. First, all of the materials had to be vacuum compatible. The coil holder is made of the machineable glass-ceramic Macor and its dimensions can be seen in Figure 4.5b. It was also important to consider the poor thermal conductivity of the volume inside the vacuum system. Relatively low currents must be used in order to minimize the need to dissipate heat in the coils used to generate the magnetic field. A B-field of a few Gauss ($1G = 10^{-4}$ T) is sufficient to lift the degeneracy of the magnetic sublevels (1.4 MHz/G$\cdot B[G] > \gamma/2\pi = 1.62$ MHz). The assembly was built with an average coil radius of $R \approx 2.3$ cm with $n = 18$ turns on each side. The wires were made of copper with Kapton insulation. The B-field as a function of applied current in the center of the Helmholtz coils was measured to be ≈ 5 G/A. The ARP experiments were carried out with 2 Amps of current for a B-field of 10 Gauss. The ARP beams traverse the atomic beam approximately in the center of the Helmholtz coils.

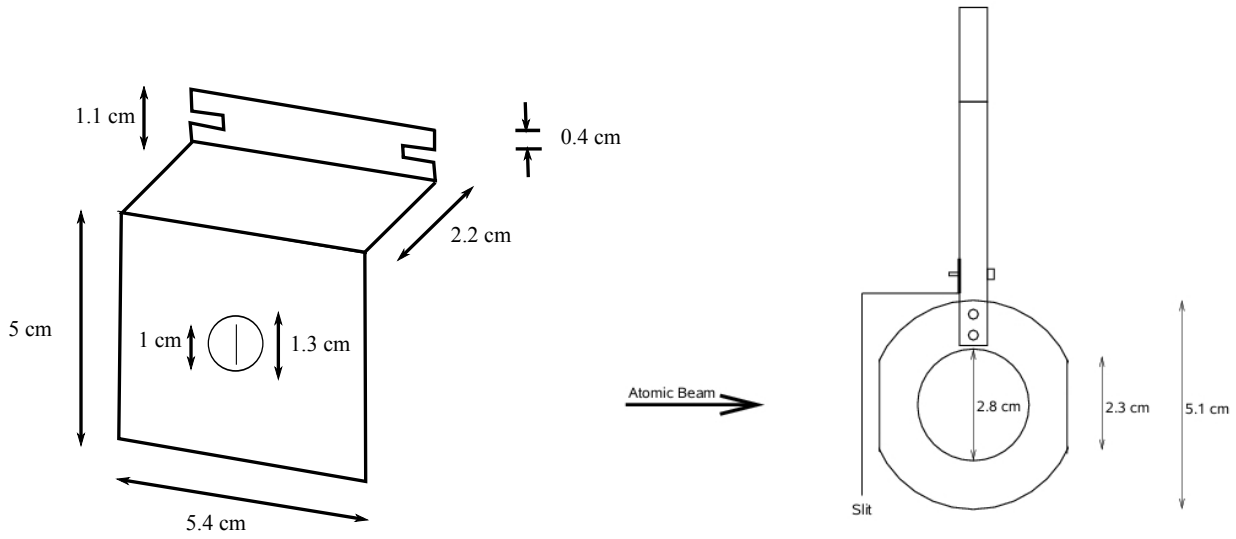

(a) Front View (b) Side View

Figure 4.5: Part (a) shows a schematic of the slit for the atomic beam. A thin slit is cut into a metal foil that is glued on a piece of aluminum. The slit is 1 cm tall and 250 μ wide. Part (b) shows a side-view of the Helmholtz coils including mount and slit for the atomic beam.

4.4 Detection Chamber

He* atoms carry nearly 20 eV of internal energy which may be released via collision. Such a collision with a metallic surface will release an energy that is much larger than the work function of that material and result in the ejection of an electron. This effect is used in the ARP experiment for the detection of He* atoms. A microchannel plate (MCP) and phosphor screen (PS) combination are used to image the cross section of the atomic distribution thereby measuring the deflection caused by the ARP force.

An MCP is a thin disc of lead glass comprised of many parallel channels perpendicular to the disc surface as seen in Figure 4.6. The 10 μm diameter channels are arranged in a hexagonal lattice with lattice spacings of 12 μm. The large internal energy of the He* atom results in near unit efficiency conversion of He* atoms to electrons. A negative bias voltage

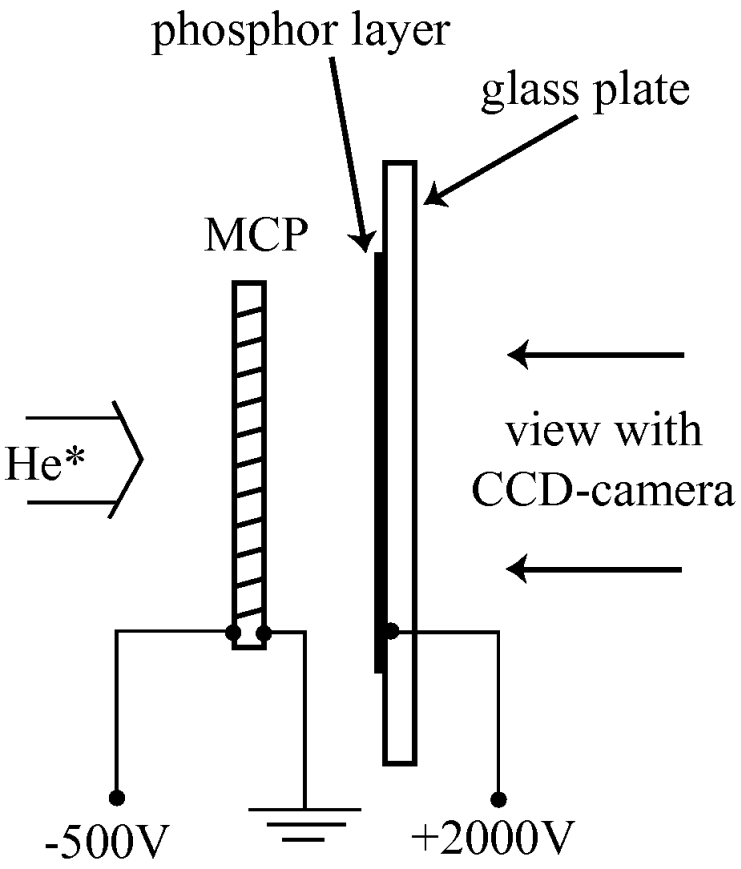

Figure 4.6: Schematic of the MCP/PS detector. Metastable helium atoms hit a multichannel plate and eject electrons, which causes a cascade that can be made visible by the fluorescence of a phosphor screen. Images of the screen are then taken with a CCD camera. Figure modified from [63]

is placed across the MCP to cause electron multiplication and acceleration of the electrons through the channels. The MCP's used in this experiment are produced by the company Photonis. They are specified to be 25 mm in diameter and provide gain of $\sim 10^3$ for a bias voltage of -1000 Volts.

The electrons are detected by a 1 inch diameter Lexel phosphor screen placed directly behind the MCP. The phosphor screen consists of a 1.16 inch diameter glass plate with a thin layer of Indium-Tin Oxide (ITO) and aluminum for conductivity. A layer of P43 phosphor

particles are deposited on top of the glass plate for an active phosphor area with a diameter of 0.96 inch. A large positive voltage ($\sim$ 2000V) is applied to the phosphor screen to accelerate the electrons from the output of the MCP to the PS. The electrons will then cause the PS to fluoresce with a brightness at a particular position that is roughly proportional to the electron flux. Therefore the brightness of the PS is related to the number of He* atoms incident upon the MCP channel directly in front of the PS.

To capture this image, a 35 mm X 50 mm front surface mirror is mounted directly behind the PS at 45°. The mirror is glued to a piece of sheet metal and is assembled together with the MCP/PS detector with Kimball Physics standard eV parts. The detector is constructed with Alumina (Al_2O_3) rods, C7X7 stainless steel plates with centered one inch diameter holes, springs, spacers, and retaining rings. Copper wires with Kapton® insulation are spot welded to the stainless steel plates and connected to high voltage power supplies through a 1.33 inch electrical feedthroughs on a flange multiplexer (see Figure 4.6 for electrical connections). The detector is mounted onto a feedthrough on the top flange of the detection region.

The image is viewed through a side window of the detection chamber and captured by a CCD camera with 640 X 480 resolution. The images of the camera are captured using a TV tuner card (AverMedia TV98). These images can be viewed on a computer screen with the program VLC Media Player and saved by the screen capture program CMD Capture in bitmap format. The default of CMD capture is to take images in RGB color format so the file size per image can be quite large ($\approx$ 1.4 MB). A video of the deflected atoms can also be taken using the open source program VirtualDub when needed. Considerable hard drive space and analysis time is saved by converting the images to 8-bit (greyscale) and cropping the images to just the area of interest before converting the images into TIFF format. This part of the analysis is done with ImageJ, a freeware Java application developed at the National Institutes of Health. The data is then analyzed with a Mathematica code,

especially written for this purpose.

The MCP/PS detection scheme is not without some disadvantages. The detector reacts strongly to the UV light from the source discharge and results in fluorescence just like the He* atoms. Also, the relationship between the fluorescence of the PS and electron number is entirely unknown and there is no absolute calibration between atom flux and the image pixel value. The PS detector is also nonlinear and nonuniform in its sensitivity to atomic flux. The non-uniformity is mainly the result of the aging of the PS under high flux impact. These disadvantages make relative measurements of atomic flux difficult, but not impossible, over a single image. The techniques used will be described in Section 6.1.

Chapter 5

Laser Systems

In this chapter I will describe how ARP light is produced for experiments in the laboratory by diode lasers, fiber amplifiers, and electro-optic modulators to drive the desired transition in metastable helium ($2^3S_1 \rightarrow 2^3P_2$) at $\lambda = 1083$ nm ($\tau(2^3P_2) \approx 97$ ns). These experiments measured the ARP force at fixed atomic velocity (varying Ω_0 and δ_0) and varying atomic velocity (fixed Ω_0 and δ_0). The chapter begins with a discussion of the frequency tuning, locking, and measurement of diode lasers. Next, it will be shown how the chirped pulses required for ARP are produced by $LiNb0_3$-based fiber-coupled, electro-optic modulators. From there, I will discuss how the frequency spectra and intensity distributions of the lasers are measured using a Fabry-Perot spectrometer and fast InGaAs photodiode respectively. This will be followed by a discussion of the Yb-doped fiber amplifiers used to produce the required intensity of the ARP beams. At the end of the chapter, I will describe the optics required to transport the optical beams to the interaction region.

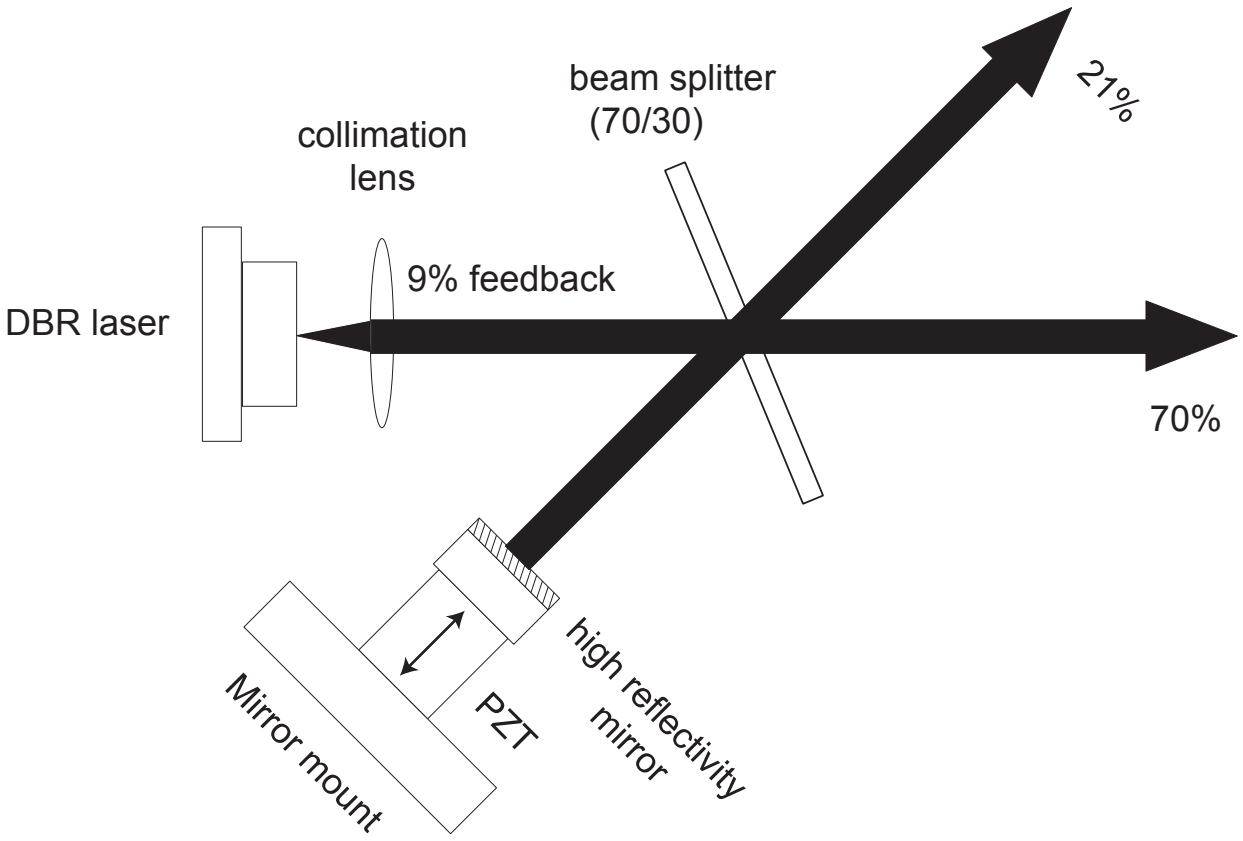

Figure 5.1: Configuration of the diode laser extended cavity. After collimation by a spherical lens, the laser light is sent through a 70/30 beam splitter. The light reflected off the beam splitter is retroreflected by a high reflectivity mirror to provide 9% optical feedback to the laser. A PZT is mounted on the kinematic mirror mount so that the external cavity length is tunable by voltage applied to the PZT. The 70% transmitted beam is used for the experiment and the 21 % leakage beam is used for saturated absorption spectroscopy.

5.1 The Diode Laser

The ARP experiments described in this thesis were done using two Spectra Diode Labs SDL-6702-H1 Distributed Bragg Reflector lasers. The distributed Bragg reflector configuration for a diode laser involves making corrugations in the substrate outside the gain region to force the diode to oscillate in a single axial mode that satisfies the Bragg condition [64]. Frequency control and stabilization of the diodes used in the ARP experiments was first

investigated by C. Avila [65].

The SDL-6702-H1 diode laser comes in a standard 8-pin TO-3 window package with a thermistor and a thermoelectric cooler included. A Newport model 325 temperature controller and a Newport model 505 current controller are used for temperature stabilization and current injection for one diode. The other diode operated with a Lightwave LDT-5910 temperature controller and Thorlabs LDC-500 current controller. The injection current to the diode may be modulated at up to 500 KHz for the purpose of frequency locking to be described later.

5.1.1 Laser Frequency Tuning

For the ARP experiment and for most experiments in atomic and molecular physics it is crucial to control and stabilize the laser frequency on both short and long time scales. The laser frequency may be coarsely controlled by adjusting the temperature of the diode with a tuning coefficient of -22 GHz/°C [65]. Fine control of the laser frequency is achieved through injection current control and has a tuning coefficient of -300 MHz/mA. To achieve the wavelength of the $2^3S_1 \rightarrow 2^3P_2$ in He* ($\lambda = 1083.3307$ nm) the thermistor on one diode was typically set to 9.83 $k\Omega$ ($\sim$ 25°C) and its current controller to roughly 140 mA. The second diode operated at a temperature of 23.3°C and $\sim$ 140 mA. At these settings, the typical diode output power is $\sim$ 30 mW.

The active optical feedback required for frequency stabilization is achieved through the use of 70/30 beam splitter and a high reflectivity mirror mounted on a piezo-electric transducer (PZT), driven by a homemade, high voltage controller (see Fig. 5.1). An "extended cavity" (EC) is formed between the back Bragg reflector of the diode and the high reflectivity mirror. Some of the light (9%) is reflected back into the diode for frequency stabilization.

A larger portion of the light (21%) is used for Saturation Absorption Spectroscopy (see Sec 5.1.2) and is hereafter referred to as the "leakage" beam. Most of the light (70%) is coupled into an optical fiber and sent to the experiment. Applying a voltage to the PZT will change the position of the EC mirror, thereby changing the length of the cavity. A change in the cavity length will in turn change the resonance condition of the laser and, as a consequence, tune the frequency of the laser.

The EC is sensitive to both mechanical vibrations, air flows, and temperature drifts. To alleviate the effects of vibrations the cavity is rigidly mounted on a solid 305 mm X 710 mm X 76 mm slab of aluminum. To diminish the effects of air flow and changes in room temperature the cavity is enclosed on 5 sides with 51 mm thick Owens-Corning® polystyrene foam. In addition to providing fine tuning of the laser frequency, the EC also dramatically reduces the laser linewidth [66, 67] to $\sim$ 125 KHz [13]. This linewidth is much smaller than the natural linewidth (1.6 MHz) of the $2^3S_1 \rightarrow 2^3P_2$ in He* used in the ARP experiment.

5.1.2 Laser Frequency Locking

To further reduce frequency fluctuations and long term drift more action must be taken. A Doppler-free Saturated Absorption Spectroscopy (SAS) signal is derived from the interaction of the leakage light and an He* cell to lock the laser frequency to the desired atomic transition [68]. The leakage light may be incident on an acousto-optical modulator (AOM) so as to produce light at some frequency δ above or below the original laser frequency based on the orientation of the AOM.

AOM's consist of a crystal into which an RF acoustic wave is launched. This acoustic wave generates a sinusoidal refractive index gradient that may act as a grating. A laser beam incident on this grating may be diffracted if the Bragg condition is satisfied. The laser

frequency is shifted either up or down by an integer multiple of the RF frequency equal to the diffraction order. The efficiency of this diffraction depends upon the laser's angle of incidence and the strength of the RF wave [69]. AOM's typically operate in the frequency range 20 - 1000 MHz, with a bandwidth typically 50% of the AOM's center frequency, and efficiencies upwards of 80% in the first order diffracted beam. Optical beams to lock off resonance are produced by an Isomet 1205-1-804B, Isomet 1250-2BS-943A, or a Brimrose TEF-270-100 AOM. These AOM's allow the laser to be detuned from atomic resonance anywhere from 30-350 MHz from atomic resonance. Each AOM is driven by a voltage controlled oscillator (VCO) and a ZHL-2W-1 Minicircuits RF amplifier. The VCO's used in this experiment were the Minicircuits ZX95-100 -S+, ZX95-200A-S+, and the ZX95-400-S+.

The beams required to do Saturated Absorption Spectroscopy are produced by the small (4%) reflection from each surface of a thick piece of uncoated glass as well as the beam transmitted through the glass (see Fig 5.2). The transmitted beam is much stronger and is referred to as the "pump" beam. The two reflected beams are referred to as "reference" and "probe" beams. The reference and probe beams pass through a He discharge cell and 50/50 beam splitter before striking two photodiodes. The pump beam is reflected from the 50/50 beam splitter and couter-propagates with the probe beam through the discharge cell. As the laser frequency is swept, the absorption peak of the reference and probe beams is the normal Doppler-broadened signal. However, there is a decrease in absorption at atomic resonance in the probe beam due to the presence of much stronger pump beam that saturates the transition and has the opposite Doppler detuning for a given velocity class of atoms. The resulting signal is referred to as the Doppler-free Lamb dip. The photodiode signal from the probe is subtracted from the reference to give a Doppler-free absorption spectrum.

The absorption signal alone is not enough to provide feedback to the laser. The laser frequency is dithered at 10 KHz for lock-in detection. The absorption signal is then sent

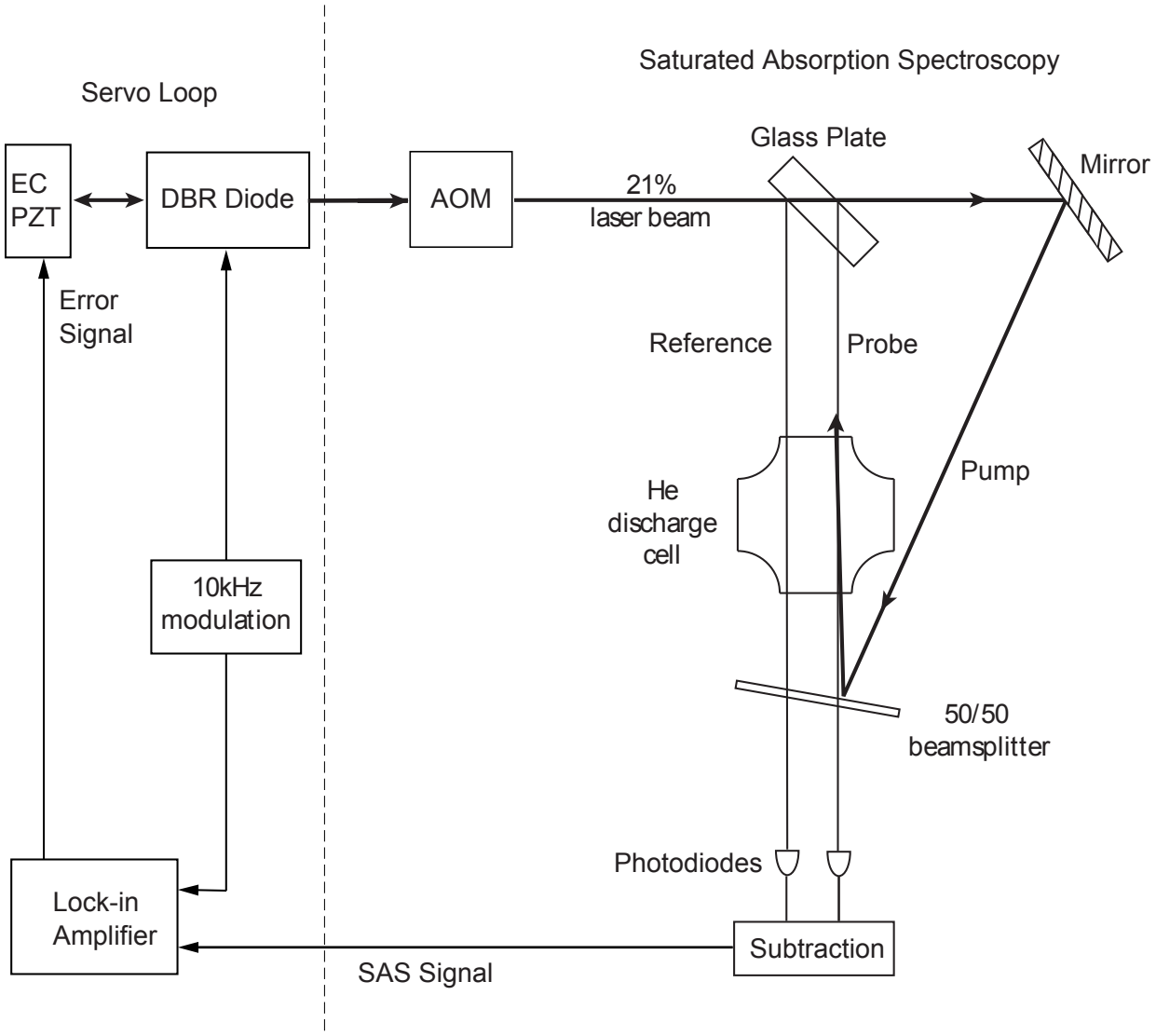

Figure 5.2: Schematic for laser frequency locking to the $2^3S_1 \rightarrow 2^3P_2$ transition of He* by Saturation Absorption Spectroscopy. The right side of the diagram shows how the SAS signal is derived from the 21% leakage beam of the diode laser. The left side of the figure shows how the SAS signal is used to produce electronic feedback for laser frequency stabilization.

to a PAR model 126 Lock-in Amplifier to produce the desired error signal. Afterwards, the error signal is sent to an SRS PID, whose output signal is sent to the PZT of the EC mirror to keep the laser frequency stable with respect to atomic resonance. If the laser light used in the SAS setup is shifted via an AOM by a frequency δ relative to the leakage light, the laser light sent to the experiment is locked at a frequency $-\delta$ from atomic resonance.

A variant of the setup in Figure 5.2 was also used at times for locking the laser at a frequency other than $-\delta$. Rather than place the AOM before the glass plate, it is also possible to place the AOM in the transmitted beam from the glass plate and use the diffracted beam for the pump beam. The Doppler subset which will be simultaneously excited by both beams will be the one with a Doppler shift equal to one half of the AOM frequency shift [70]. This results in frequency locking at $-\delta/2$. As a result, it becomes much easier to lock the diode laser to a specific frequency relative to atomic resonance when only AOM's of certain frequencies are available.

5.1.3 Relative and Absolute Frequency Measurements

For the variable velocity measurements of the ARP force it was required to sweep the frequency of the diode lasers in a controllable fashion. An atomic velocity was simulated by the Doppler shift from oppositely-detuned, counter-propagating optical beams. By applying a slow, periodic, ramp voltage to the PZT of each diode's EC mirror, the velocity dependence of the ARP force could be studied for fixed intensity and chirp on the minute time scale.

The voltage tuning of each diode laser was calibrated using the scheme shown in Fig. 5.3. In this setup one of the diode lasers was locked to atomic resonance by SAS while the other diode's frequency was swept. The ramp voltage was supplied by a Wavetek 142 function generator and amplified by a homemade voltage amplifier. The ramp signal was monitored

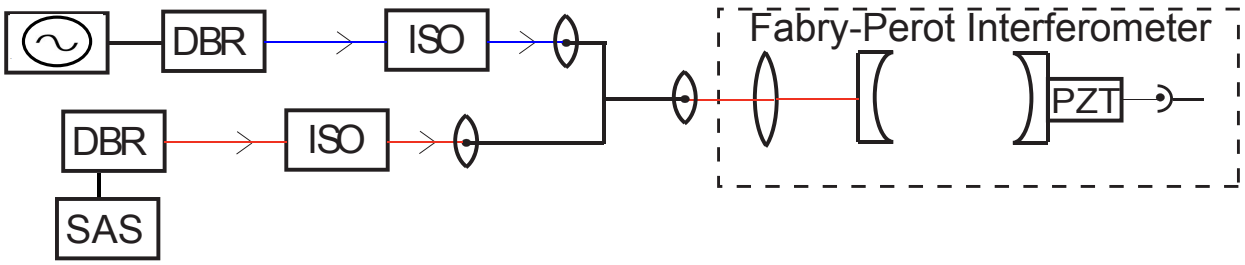

Figure 5.3: Shown above is the schematic for calibrating the frequency sweep of the diode lasers.

by a Lecroy WaveAce 232 oscilloscope. The lasers were then fiber-coupled seperately and combined by a 50/50 O/E Land fiber splitter (used in reverse). The combined light was then coupled into a scanning Fabry-Perot (FP) interferometer. Locking one of the lasers to a reference will negate any slow changes to the FP cavity from changes in the room temperature. The out-coupled light was measured on a photodiode, monitored by a Tektronix 210 oscilloscope. The interferometer is scanned quickly ($\sim$ 500 Hz) relative to the diode frequency sweep ($\sim$ 0.1 Hz). The oscilloscope trace is saved periodically and the frequencies are found by fitting a Lorentzian to each peak (see Fig. 5.4 for an example). To obtain a frequency scale for the FP one of the lasers contained two frequency components separated by a known frequency (80 MHz) created by an AOM. The frequency sweep of each diode was measured to be 56.67(45) MHz/V and 393.8(24) MHz/V. The uncertainties in each measurement correspond $< 1\%$.

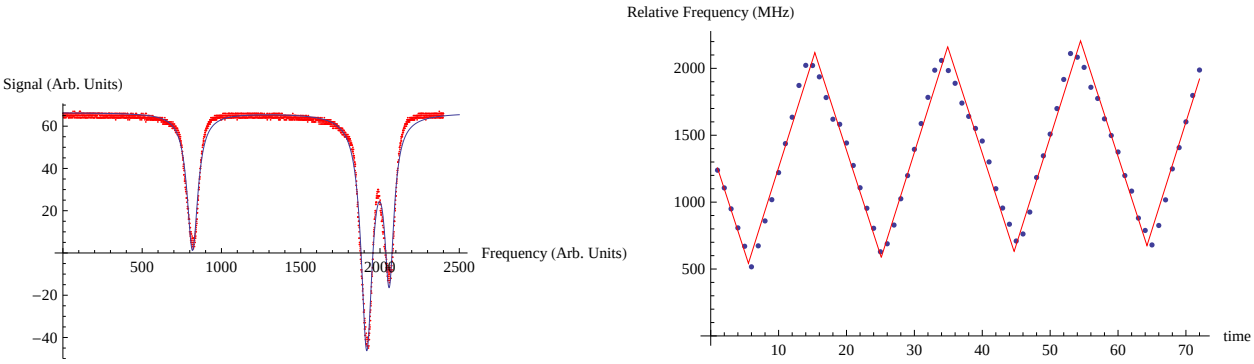

(a) Example FP Spectra for Sweep Calibration (b) Frequency Sweep of a Single Diode

Figure 5.4: Shown here are plots used to determine the frequency sweep amplitude as a function of applied voltage to the PZT of an EC mirror for a single diode. Plot (a) is a spectrum of the combined diode light (points) fitted with 3 Lorentzians (solid line). Plot (b) is the relative frequency of the two diodes as one of the diodes is swept as a function of time. The solid line corresponds to a best fit to the experimental data represented by points on the plot. From this plot the frequency of a diode can be known as a function of applied voltage when measured against a reference.

5.2 Electro-optic Modulators

For the ARP experiment electro-optic modulators were used to produce two separate pulsed and chirped optical beams. This is made possible by the linear electro-optic effect in $LiNb0_3$ crystals. The linear electro-optic effect refers to the change in the refractive index of a material in the presence of an applied electric field [71]. The NIR-MX-LN03 from Photline Technologies[1] amplitude modulator creates an optical pulse from CW light. The Photline NIR-MPX-LN03 phase modulator adds a frequency chirp to the input light field.

The linear optic effect in a crystal is relatively simple if the electric field applied and the polarization of the light field are along one of the principle axes of the crystal. The strongest electro-optic coefficient for $LiNbO_3$ (r_{33} along the Z direction) dictates the applied E-field and the polarization of the light field to be along the Z axis (see Fig 5.5). A light wave

[1]Photline Technologies, 16 rue Jouchoux, 25000 Besancon, France. Phone: +33 (0) 381 85 31 80. www.photline.com

traveling perpendicular to the E-field will experience a change in optical path length due to the change in the index of refraction of the material. This results in a modulation of the phase of the light field (and therefore frequency) if the applied E-field is time dependent.

The electro-optic effect is generally very small ($r_{33} = 32$ pm/V in $LiNbO_3$). This requires a large E-field to be applied to create a sizable phase shift. This can be accomplished, however, with the use of a waveguide-type integrated modulator. In this type of modulator the electrodes are placed very close together, producing a large E-field with a much lower drive voltage when compared to that of bulk modulators.

5.2.1 Phase Modulator

When a time dependent voltage is applied to the electrodes of a phase modulator the total phase delay that is introduced to the light traveling along the waveguide is given by

$$\phi(t) = \kappa M(\omega_m) V(t) \tag{5.1}$$

with

$$\kappa = \frac{\pi}{\lambda G} n_e^3 r_{33} \eta L \tag{5.2}$$

where L and G represent the length of and gap in between the electrodes respectively, r_{33} is the electro-optic coefficient, and n_e is the index of refraction for the light polarized in the extraordinary direction. The η term refers to an overlap coefficient of the electric and optical fields. The dimensionless parameter $M(\omega_m)$ describes the frequency dependence of the phase delay as a result of RF losses and RF to optical phase mismatch.

An important quantity for characterization of a phase modulator is the voltage required to produce a π phase shift, or V_π. This is the voltage required to delay the signal by half of

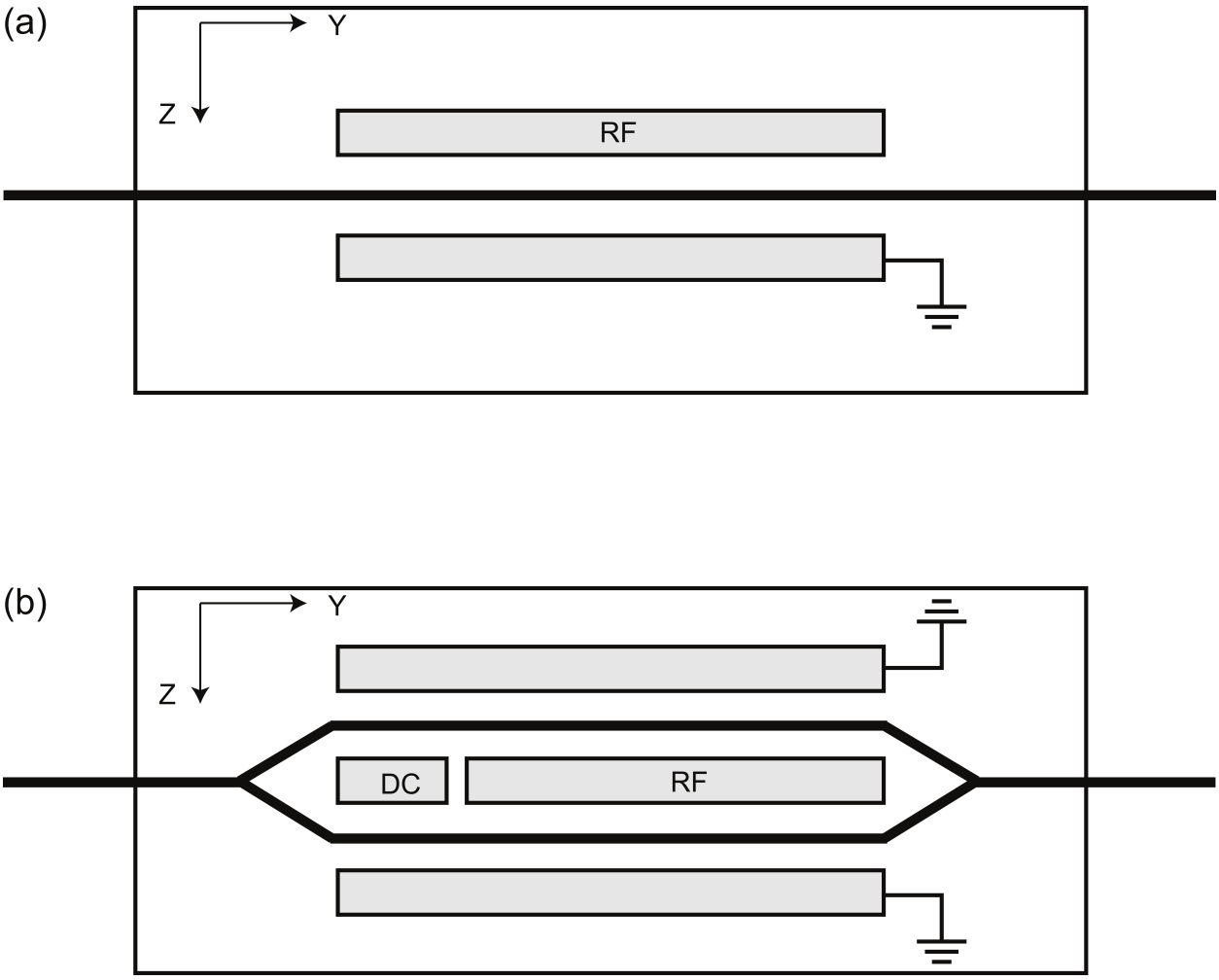

Figure 5.5: Schematic layouts of the NIR-MPX-LN03 phase and NIR-PX-LN03 amplitude modulator ((a) and (b) respectively). The principle axes of the crystal are shown in the corner of the figure.

a wave and is sometimes referred to as the half-wave voltage. V_π for a given drive frequency (ω_m) can be calculated with the equation

$$V_\pi(\omega_m) = \frac{\lambda G}{n_e^3 r_{33} \eta L M(\omega_m)} \tag{5.3}$$

$M(\omega_m) = 1$ for DC modulation and decreases as a function of ω_m.

In the ARP experiment a sinusoidal RF modulation signal is applied to the phase modulators resulting in an optical field in the form of

$$E(t) = E_0 \cos[\omega_l t - \beta \sin(\omega_m t)] \tag{5.4}$$

where E_0 is the amplitude of the light field and ω_l is the unmodulated laser frequency. β is commonly known as the modulation index and is the amplitude of the phase modulation. From Eq. 5.1, Eq. 5.3, and Eq. 5.4 it can be shown that

$$\beta = \frac{\pi V}{V_\pi(\omega_m)} \tag{5.5}$$

In practice it is not easy to determine $V_\pi(\omega_m)$ for a phase modulator. One way is to measure it by calculating β from the measured Fourier spectrum of the phase modulated signal when a sinusoidal modulation voltage is applied. Measurement and calculation of the half-wave voltage is described later in the chapter.

It is well known that the instantaneous angular frequency of a light field is just the time derivative of the overall phase. Therefore it can be shown that phase modulation leads to frequency modulation of the form

$$\omega(t) = \frac{d\phi(t)}{dt} = \omega_l - \beta \omega_m \cos(\omega_m t) \tag{5.6}$$

Sinusoidal phase modulation results in cosinusoidal frequency modulation at the same frequency ω_m.

5.2.2 Amplitude Modulator

The amplitude electro-optic modulator is very similar to the phase modulator with the exception that instead of a single waveguide, a Mach-Zehnder interferometer is patterned into the $LiNb0_3$ substrate (refer to Figure 5.5b) [72]. In this configuration a single waveguide is split into two parallel waveguides and then recombined into a single waveguide. In the Photline NIR-MX-LN03, grounded electrodes are placed outside the arms of the interferometer. Two other electrodes are placed in between the two arms. A DC voltage is applied to one of the electrodes to cause destructive interference in the presence of no RF. An RF pulse is applied to the other electrode to produce the desired optical pulse.

The output electric field can be described in general as

$$E(t) = \frac{E_0}{2}[\sin(\omega_l t + \phi(t)) + \sin(\omega_l t - \phi(t)] = E_0 \sin\phi(t) \sin\omega_l(t) \tag{5.7}$$

where $\phi(t)$ is the total phase shift in one arm of the Mach-Zehnder interferometer proportional to the voltage applied to the DC and RF electrodes. Light in each arm of the interferometer experiences a phase shift of the same magnitude but opposite sign. This is done so there is no net phase modulation on the output pulse. The resulting output power is

$$P(t) = \frac{P_0}{2}[1 + \sin 2\phi(t)] \tag{5.8}$$

where P_0 is the maximum output power.

5.2.3 Production of Chirped Pulses

Two trains of counterpropagating, periodic, chirped pulses are required to study the velocity dependence of the optical forces from periodic adiabatic rapid passage. In experiments to measure the ARP force at a fixed atomic velocity the first step in this process is the creation of the optical pulses. The pulses are produced from a single NIR-MX-LN03 amplitude modulator whose transfer function is $\sin\phi(t)$ (see Eq. 5.7). The desired output is a $\approx 25\%$ duty cycle, sinusoidal optical pulse of duration 3.125 ns (as modeled in Chapter 2). This required a triangle-shaped electric pulse of the same duration and duty cycle. Experiments to measure the ARP force for varying atomic velocity required two separate laser diodes and hence two separate amplitude modulators. This subsection will describe the production of chirped pulses for the fixed velocity experiments but the techniques are readily applicable to experiments with variable atomic velocity.

The RF signal sent to the amplitude modulator is supplied by an HP8082A pulse generator triggered by an HP8657A signal generator (see Fig. 5.6). The HP8657A signal is set to a frequency of 80 MHz and an output power of +7 dBm, setting the repetition rate of the pulses at 80 MHz. The HP8082A creates a triangle-shaped electronic pulse at $\approx 25\%$ duty cycle, with an amplitude of ≈ 4 volts, and a base width of ≈ 3.4 ns (see Fig. 5.7). This is done by proper selection of the pulse width, transition time, and amplitude settings. Technical limitations of the HP8082A are chiefly responsible for the discrepancies between the desired and actual pulses. The DC voltage is supplied by a Power Design Inc. model 2005 precision power supply.

Two phase modulators are required in the experiment to create frequency sweeps of opposite directions. The 160 MHz RF signal to drive the 2 NIR-MPX-LN03 phase modulators originates from a single HP8657D signal generator. The signal is then amplified by a Mini-

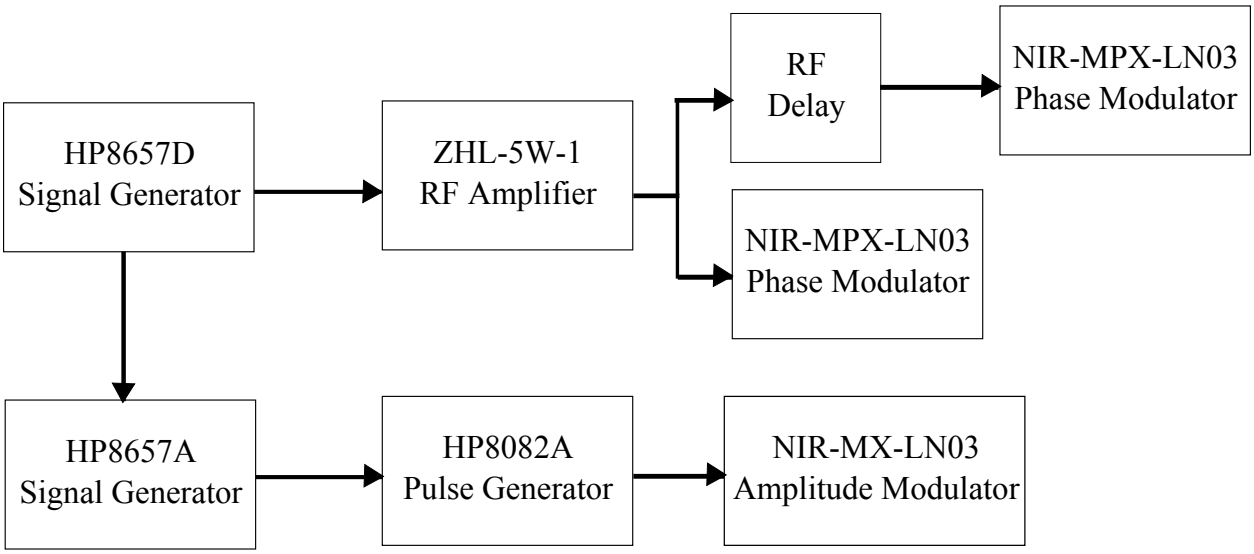

Figure 5.6: RF signal generation for use with EOM's. The RF signal to the NIR-MX-LN03 is supplied by an HP8082A pulse generator triggered by an HP8657A signal generator. The DC voltage is supplied by a Power Design Inc. model 2005 precision power supply. The signal is then amplified by a Mini-Circuits ZHL-5W-1 RF amplifier powered by a Power Design Inc. model 6105 power supply. Afterwards the signal is split into two equal parts with one signal sent directly to a phase modulator and the other is delayed by an RF trombone before it arrives at the other modulator.

Circuits ZHL-5W-1 RF amplifier. This amplifier has a gain of $\approx$ 43 dB at an input RF frequency of 160 MHz. The ZHL-5W-1 is powered by 24 Volts DC from a Power Design Inc. model 6105 power supply. The resultant signal is then sent to a Minicircuits 50/50 RF splitter. One arm of the RF splitter is sent directly to a phase modulator. To control the relative phase of the RF signals, the other signal is sent to an RF trombone for delay before being sent to the second phase modulator. The amount of phase modulation is limited by the maximum input power to a single phase modulator of +29 dBm.

It is necessary to synchronize the frequency chirping and amplitude modulation in order to produce the chirped pulses needed for ARP. The HP8657D signal generator is synchronized to the HP8657A signal generator through the high precision frequency reference output of the HP8657D. The relative phase of the signal generators will remain relatively constant for

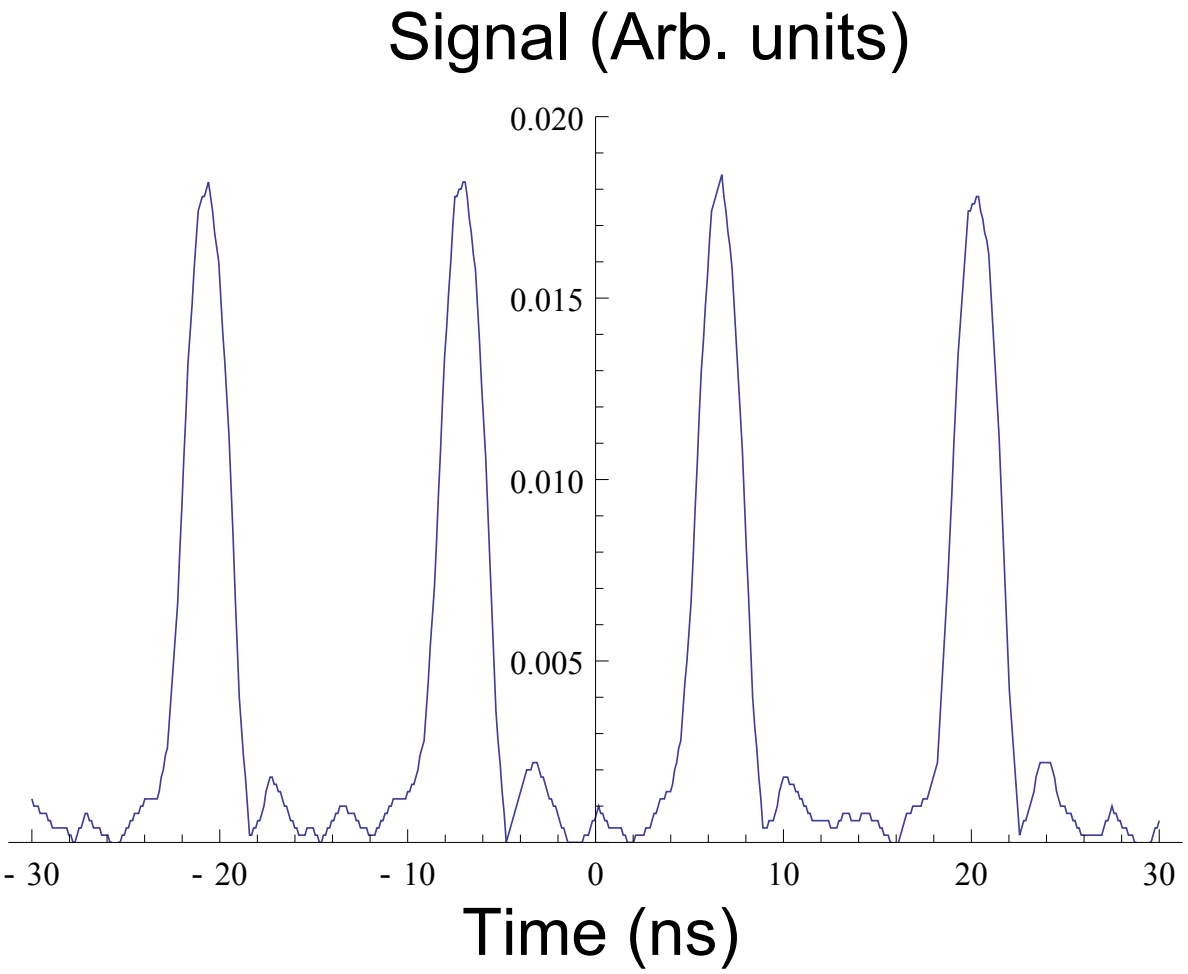

Figure 5.7: Electronic and optical pulses used in the ARP experiment. Light pulses as measured by a Thorlabs D400FC fast photodiode. The data was taken with a Lecroy WaveAce 232 oscilloscope.

upwards of 1 hour. By adjusting the delay knob on the pulse generator and the length of the RF trombone, control of the relative phase between the electronic signals sent to the three modulators is obtained.

5.3 Characteristics of Chirped Pulses

The use of fiber-coupled electro-optical modulators allows for the creation of nanosecond scale optical pulses whose frequencies can span a few GHz by properly synchronizing the modulator drivers. The intensity of the pulse profiles is measured by a D400FC Thorlabs fast photodiode. The frequency spectrum is measured by a home-built Fabry-Perot spectrometer (see Fig. 5.8).

For sinusoidal amplitude and phase modulation, the optical electric field for $0 < t < \pi/\omega_m$ is

$$E(t) = \underbrace{E_0 \sin(\omega_m t)}_{\text{amplitude}} \underbrace{\cos\left[\omega_\ell t + \beta \sin(\omega_m t) + \phi\right]}_{\text{phase}} \tag{5.9}$$

where ω_ℓ is the laser frequency and $\beta = \delta_0/\omega_m$. The instantaneous frequency of the light field is $\omega_\ell + \delta_0 \cos\omega_m t$ which sweeps a frequency of $2\delta_0$ in the requisite time of $\pi/2\omega_m$. The relative phase of the amplitude and phase modulation is represented by ϕ.

In general the Fabry-Perot spectra can be calculated from the equation

$$I_{FP,n}(\omega_l + n\omega_c) = \left| \frac{2}{T} \int_0^T E(t) exp(-i(\omega_l + n\omega_c)t) dt \right|^2 \tag{5.10}$$

where n refers to the n^{th} peak relative to the carrier frequency.

The Fabry-Perot spectra of the purely amplitude modulated spectrum ($\beta = 0$) is

$$I_{FP,n}(\omega_l + n\omega_c) = \frac{4}{4 - n^2} \cos^2(\frac{n\pi}{4}) \tag{5.11}$$

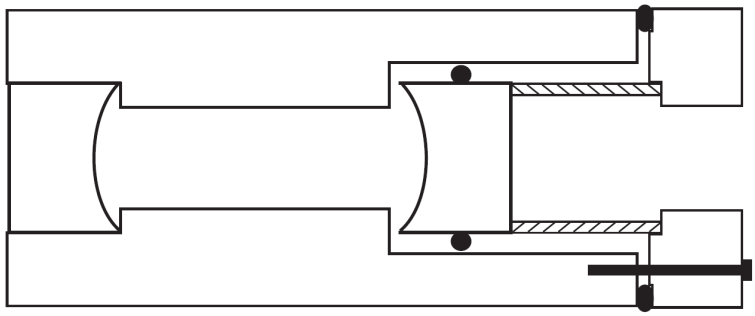

Fabry-Perot Spectrometer

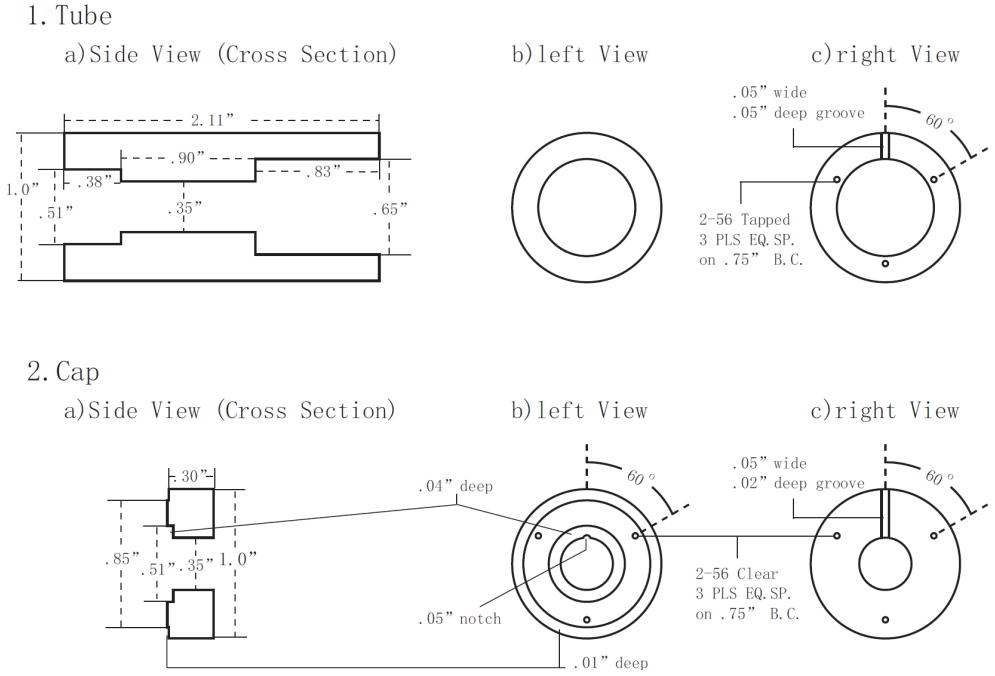

Figure 5.8: Schematic of the Fabry-Perot spectrometer used to measure the laser spectrum. the length of the cavity is 25 mm, the mirror diameters are 12.7 mm, with a focal length of 25 mm and thickness of 9.5 mm.

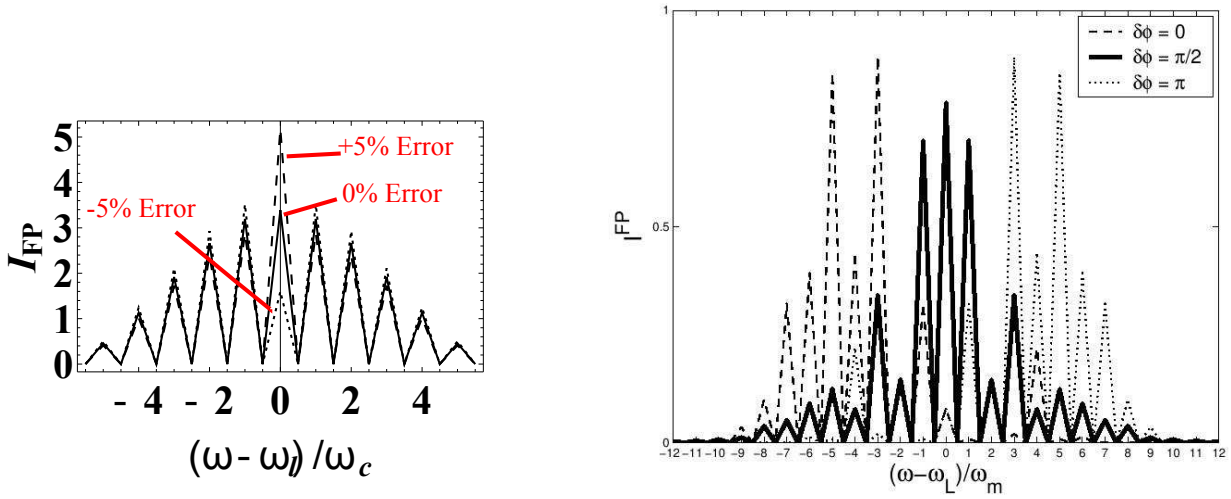

(a) Effects of a bias light field

(b) Phase dependence between PM and AM

Figure 5.9: Calculated FP spectra. Plot (a) shows how a DC bias field effects the carrier frequency. The stated DC offset is measured as a percentage of V_π. Plot (b) represents the effects of the relative phase between AM and PM on a calculated FP spectrum.

The peaks are separated by the repetition rate of the pulse ($\omega_c = \omega_m/2$). There are two critical requirements for ARP, one of which is the absence of any residual CW light. This may be monitored by the height of the carrier frequency peak to the other peaks of the spectra. The effect of residual CW light on the Fabry-Perot spectra can be seen in Fig. 5.9a.

The Fabry-Perot spectra of the purely phase modulated spectrum is given by

$$I_{FP,n}(\omega_l + n\omega_m) = J_n^2(\beta) \tag{5.12}$$

where $J_n(\beta)$ is the nth order Bessel function of the first kind evaluated at β. An example of a purely phase modulated spectrum can be seen in Fig. 5.10a.

The time-averaged, modulus squared frequency spectrum of each pulse is analyzed by a $\approx$ 30 MHz resolution Fabry-Perot cavity. The second critical requirement for ARP is that the relative phase between the amplitude and phase modulation signals (ϕ from Eq. 5.9) is

either 0 or π. If $\phi = 0$ the frequency sweep is upward and if $\phi = \pi$ the frequency sweep is downward. Both instances sweep symmetrically about the carrier frequency and as a result the Fabry-Perot spectra are symmetric about the carrier frequency. If $\phi \neq 0, \pi$ then the Fabry-Perot spectra will not be symmetric about the carrier frequency. The effect of ϕ on the FP spectra can be seen in Fig. 5.9b.

The Fabry-Perot spectra used in the ARP agree qualitatively with the calculated Fourier transform of a phase and amplitude modulated light field. Discrepancies between calculated and experimental spectra arise mostly from limitations of the HP8082A pulse generator. Examples of measured Fabry-Perot spectra can be seen in Fig. 5.10.

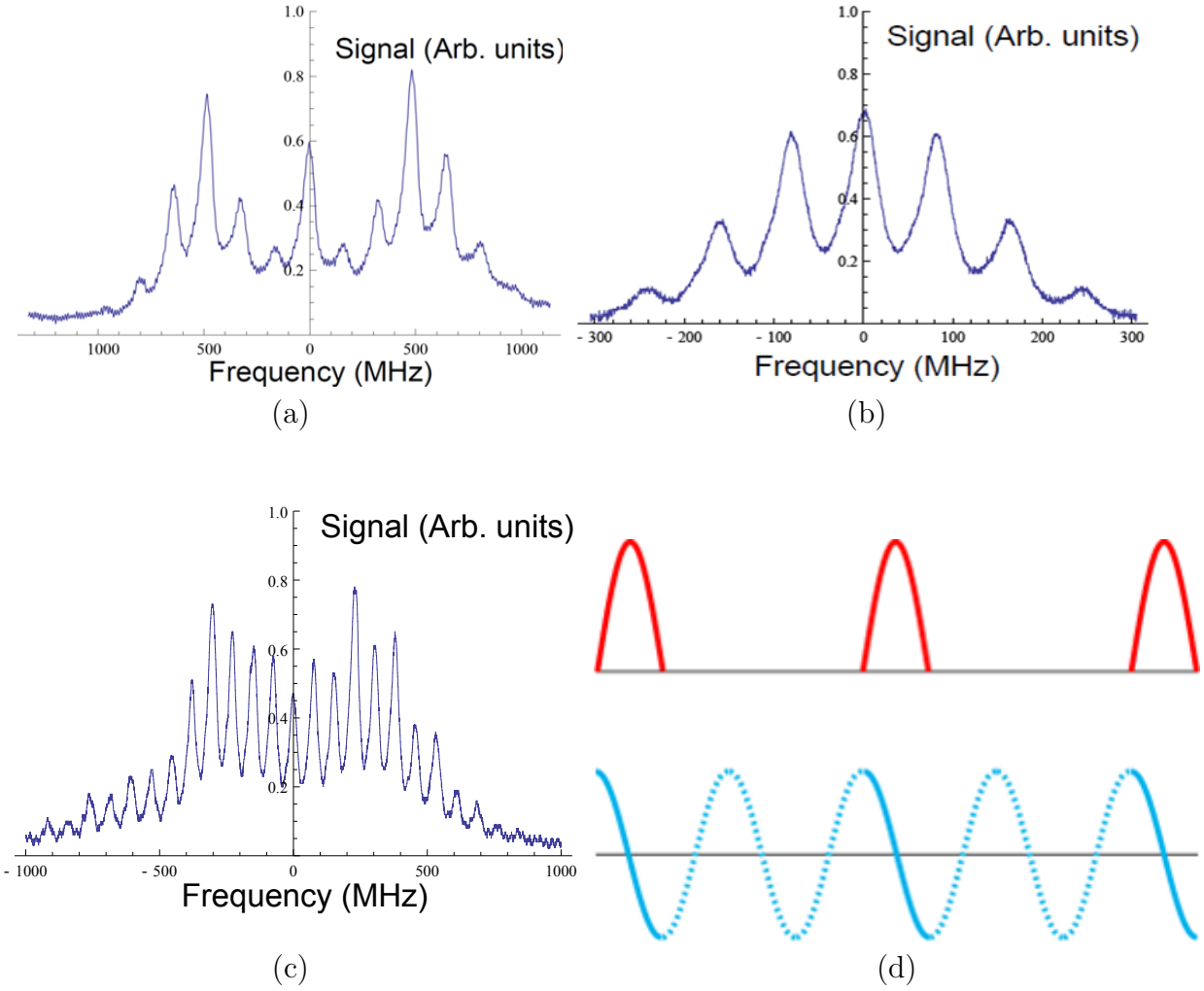

Figure 5.10: Measured Fabry-Perot spectra. Fig. 5.10a and Fig. 5.10b show examples of the frequency spectrum for phase-modulated only and amplitude-modulated only light respectively. Fig. 5.10c is the combined AM-PM spectrum with $\beta = 4.5$. Fig. 5.10d is the timing sequence for the intensity and frequency sweeps.

5.4 ARP Light Production

The diode lasers used in the ARP experiment typically put out ~ 30 mW of power (20 mW after EC). Insertion losses from each EOM, the amplitude modulator running at 25% duty cycle, free space fiber coupling, and splitting into two beams would result in optical power in each ARP beam less than 0.1 mW. ARP requires a large Rabi frequency ($\Omega \gg \omega_m$), and hence large optical power, for the atomic state to adiabatically follow the optical field during an ARP sequence. To achieve such a large Rabi frequency 4 fiber amplifiers are required in each experiment. A generalized schematic of the setup for fixed and variable atomic velocity experiments can be seen in Fig. 5.11 and Fig. 5.12.

For the fixed atomic velocity experiments the diode light from the extended cavity is fiber-coupled and amplified by a Keopsys model 0IYB30 1W fiber amplifier. The optical amplifiers used in the experiment use Yb-doped fibers as the gain medium. Yb-ions doped in the fiber core absorb strongly near 980 nm, where high-power, broad-stripe diode lasers are commercially available. Pump light is injected from a V-groove mechanically formed in the outer cladding of the fiber and propagates in the inner cladding. The seed light, at 1083 nm, is amplified by stimulated emission with a gain proportional to the pump power of the 980 nm diode lasers inside the amplifier. Both the input and output fiber connection of each fiber amplifier is single transverse mode, FC/APC to prevent harmful back reflections to the fiber amplifiers and the diode lasers.

The output of this fiber amplifier is amplitude modulated by a Photline model NIR-MX-LNO3, and amplified by another Keopsys 0IYB30 1W fiber amplifier. The light is then incident on an AOM operating at frequency 2δ (with respect to SAS AOM) to produce two spatially separate pulses of frequency δ and $-\delta$ (relative to atomic resonance) from the undiffracted and first order diffracted beams. The undiffracted beam goes through a delay

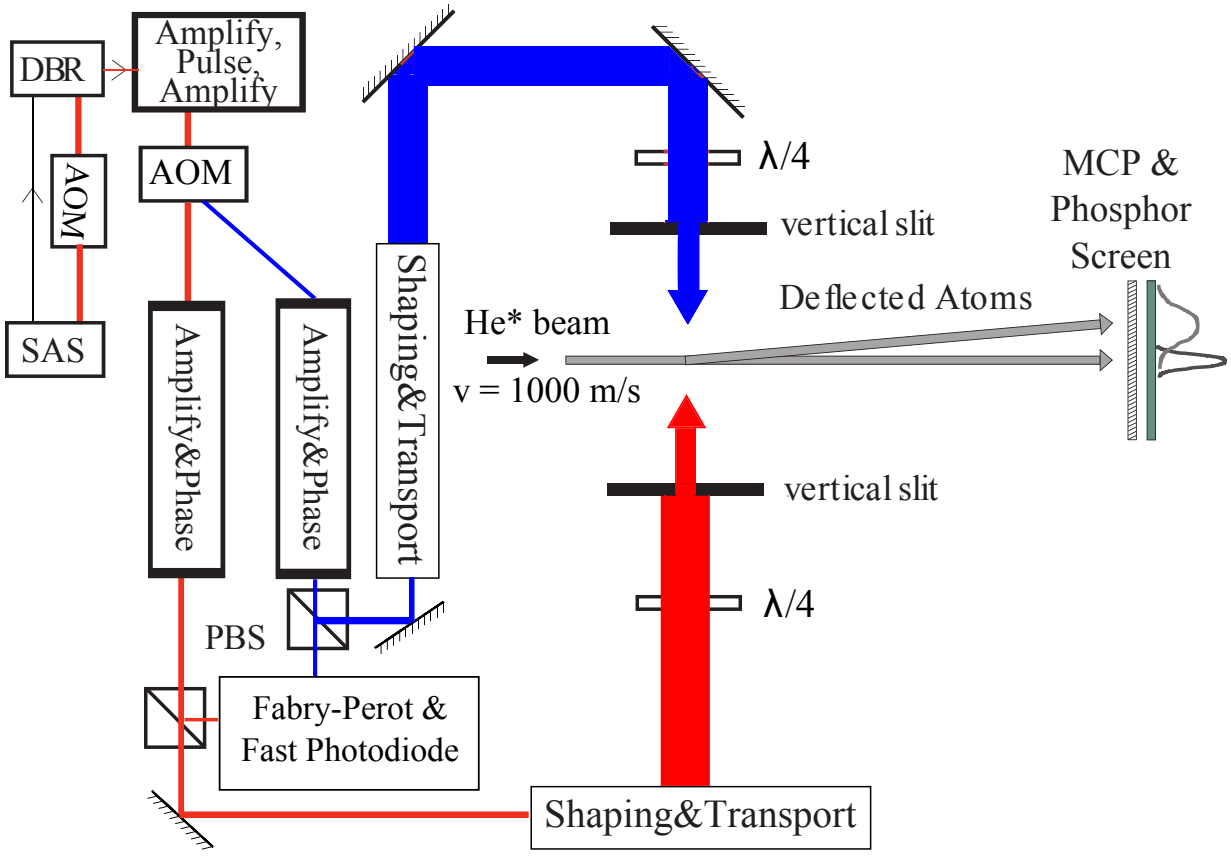

Figure 5.11: Experimental setup for deflection of He* with pulsed, chirped light at a fixed atomic velocity. Diode light is amplitude and phase modulated using EOM's while the absolute frequency is locked at a chosen frequency δ from atomic resonance. Using both undeflected and deflected beams from an AOM produces two optical beams at frequencies shifted by $+\delta$ and $-\delta$. More details can be seen in Fig. 5.13. Multiple fiber amplifiers are used to achieve sufficient optical power. The two pulses interact transversely with a He* beam sequentially to produce an atomic deflection that is detected using an MCP and phosphor screen.

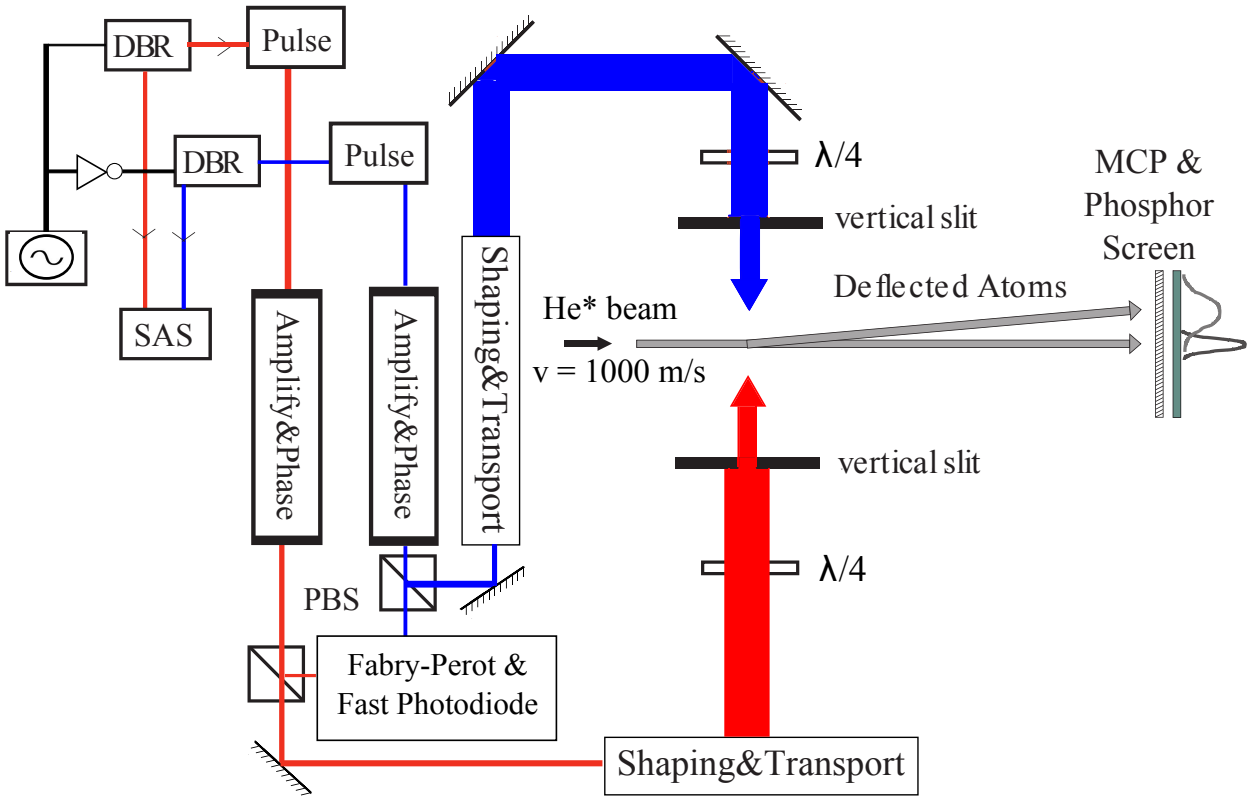

Figure 5.12: Experimental setup for deflection of He* with pulsed, chirped light with variable atomic velocity. Diode light is amplitude and phase modulated using EOM's while the frequency of each laser is swept slowly to simulate an atomic velocity. Multiple fiber amplifiers are used to achieve sufficient optical power. The two pulses interact transversely with a He* beam sequentially to produce an atomic deflection that is detected using an MCP and phosphor screen.

stage to enable proper timing of the ARP sequence. Then each beam is frequency modulated by separate Photline model NIR-MPX-LNO3 phase modulators before being amplified by two Keopsys model KPS-BT2-YFA 4W amplifiers separately in order to supply the necessary ~ 1 W of average power, modulated light. The KPS-BT2-YFA amplifier requires an average input optical power of at least 0.5 mW. A detailed picture of the experimental setup before the 4W fiber amplifiers can be seen in Fig. 5.13.

After the 4W amplifiers, each beam goes through a waveplate and a polarizing beam splitter (PBS) to control the optical power delivered to the experiment. The total optical power delivered to the experiment can also be manipulated by changing the current to the diodes of the fiber amplifiers. The leakage light from the PBS's are coupled to optical fibers and sent to fast photodiodes and a Fabry-Perot spectrometer for monitoring (see Sec. 5.3). The optical power of each beam is measured by separate Newport 1825-C power meters using the reflection from a microscope slide placed before a spherical telescope. The output power readings are sent to a single Tektronix 210 oscilloscope to be sent to a PC through a Prologix GPIB adapater. The voltage reading on the oscilloscope is calibrated using a Coherent 210 power meter placed at the focus of the cylindrical telescope. See Fig. 5.14 for a detailed picture of how the optical power is monitored.

The Gaussian beams are shaped by spherical and cylindrical telescopes to have horizontal and vertical waists of 5.9 mm and 1.7 mm respectively (Figure 5.15). A maximum intensity of ~ 26 W/cm^2, about $1.6 * 10^5$ I_S, where the saturation intensity is $I_S \equiv \pi hc/(3\lambda^3\tau)$, is achieved when the fiber amplifiers are running at ~ 1.1 W output power (Typical maximum running optical power used in the experiment). The output beam of each fiber amplifier is σ^+ polarized by a $\lambda/4$ waveplate to drive the closed transition between $2^3S_1 \rightarrow 2^3P_2$ $\Delta m_j = +1$ He* transition. The laser beam is occluded at the edges by a vertical slit of width $d = 4$ mm to limit the interaction time to $\approx 4\mu s$ ($\sim 40\tau$) with $v_\ell \sim 1000$ m/s and to ensure that

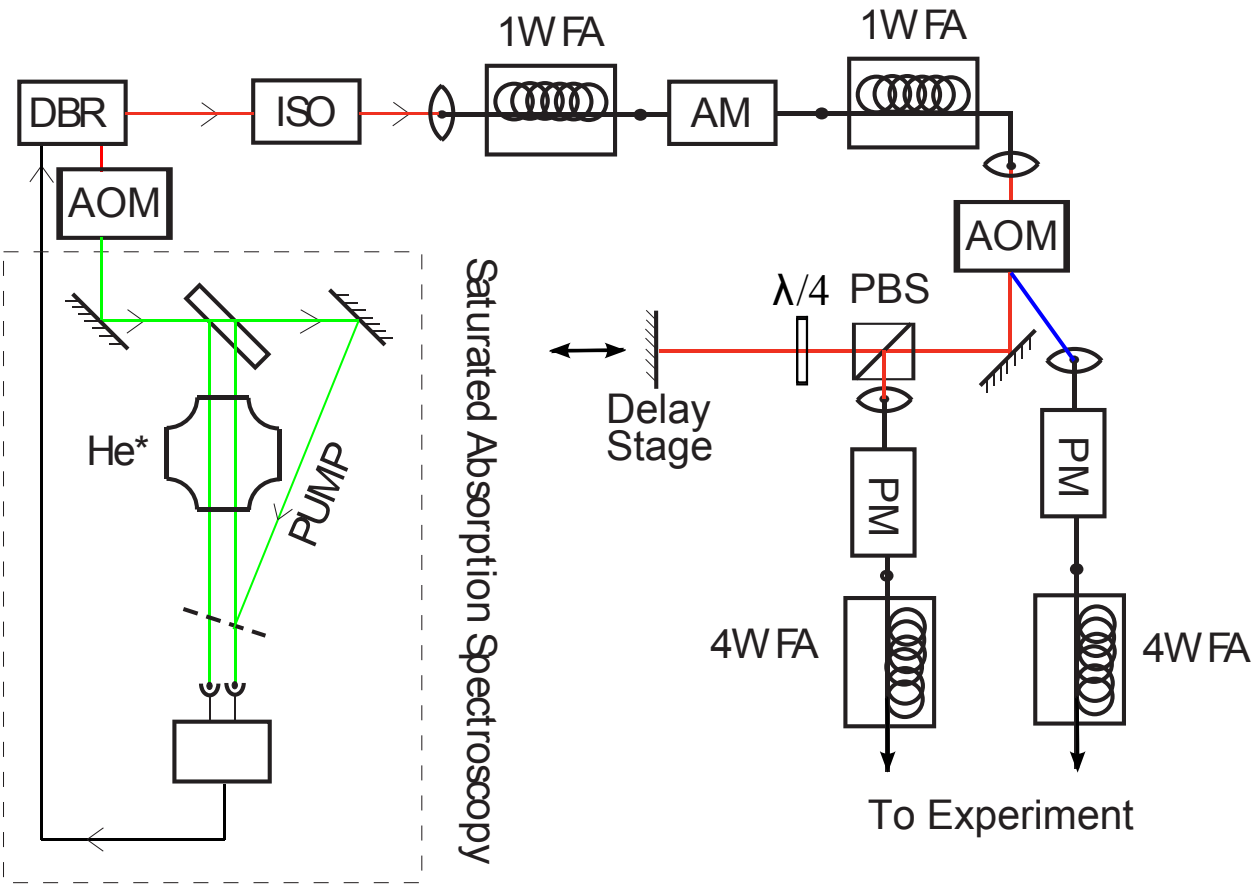

Figure 5.13: Optical system to produce two spatially separate chirped pulses. The diode laser goes through an isolator before being coupled into a SM optical fiber. The light is amplified and amplitude modulated before being amplified again. The resultant beam in sent through an AOM operating at 2δ. The deflected beam is phase modulated before being sent to a 4W YDFA. The undeflected beam is delayed and then phase modulated before amplification.

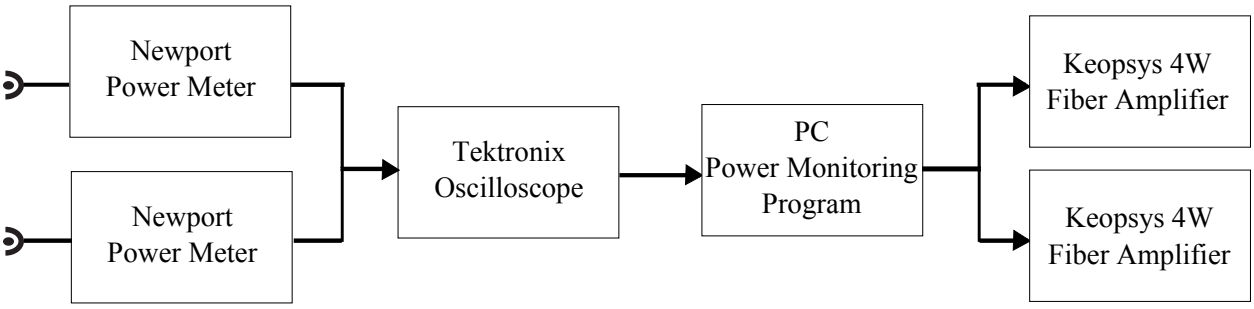

Figure 5.14: The optical power of light reflected from a piece of glass in each collimation line is measured by a Newport 1825-C power meter. The power readings are sent to a single Tektronix 210 oscilloscope to be sent to a PC through a Prologix GPIB adapter. A signal may then be sent by the PC to change the diode current in either 4W YDFA to achieve the desired optical power in each beam at the interaction region. The power measurement is calibrated with a Coherent 210 power meter before running the experiment.

the Rabi frequency will only vary by $\sim 6.4\%$ across the interaction region. A small fraction of the output of the first amplifier is used to optically pump the He* atoms to the $m_j = +1$ ground state. This is done by an additional 2.4 mm vertical slit 5.2 mm upstream from the ARP slit. The vertical slits are placed ~ 13 cm from the interaction region to minimize the effects of diffraction.

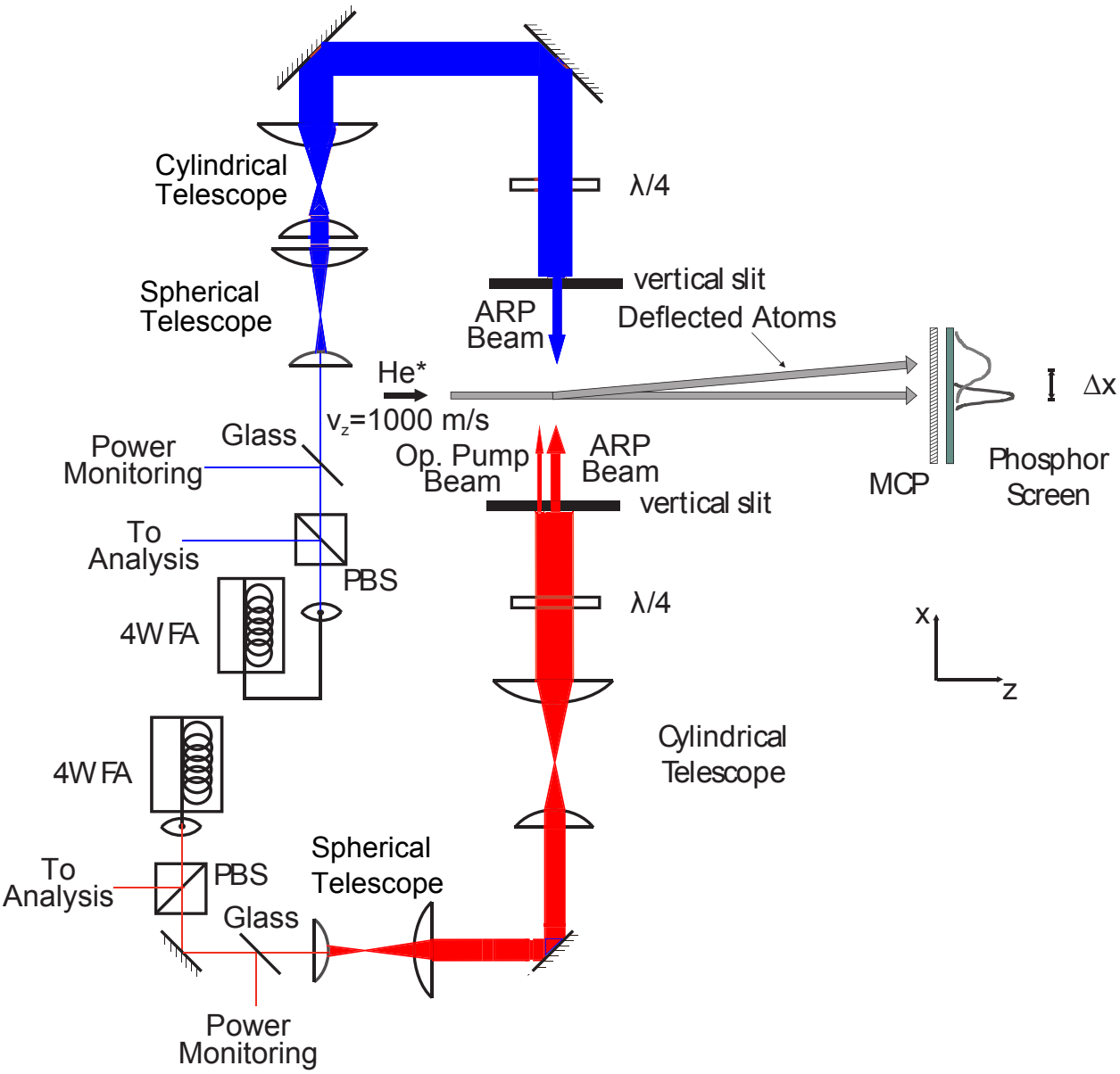

Figure 5.15: Optical setup for the interaction region. The optical beams are collimated and expanded by spherical and cylindrical telescopes. The resultant beam has a Gaussian profile with $\omega_z = 5.9$ mm and $\omega_y = 1.7$ mm. The z-axis (direction of atomic beam propagation) is further defined with a 4 mm vertical slit for both beams. An additional 2.4 mm vertical slit is present 5.2 mm upstream from the ARP slit in one beam for optical pumping.

Chapter 6

Measurement of Optical Forces

6.1 Experiment Overview

The goal of this experiment is to investigate the velocity dependence of the optical force on atoms associated with many adiabatic rapid passage sequences. A general overview of the experimental setups can be seen in Fig. 5.11 and Fig. 5.12. Details of the atomic beam apparatus and the optical system are described in Chapters 4 and 5.

In this experiment, chirped laser pulses interact with an atomic beam of He* at 90° to impart a transverse momentum kick of $\hbar$k to the atoms. The first chirped pulse, duration $\pi/\omega_m = 3.125$ ns, drives the atom to the excited state and a momentum of $\hbar\mathbf{k}$ is transfered to the atom. This pulse is immediately followed by a counter-propagating, chirped laser pulse of the same duration that drives the atom back to the ground state. The atom recoils in the same direction as the first momentum kick for a net change of the atomic momentum by $2\hbar$k. The next pulse pair arrives $2\pi/\omega_m = 6.25$ ns later, as shown in Fig. 2.2, leading to the expression of the average optical force for a single ARP sequence to be $\mathbf{F} = \Delta\mathbf{p}/\Delta t = 2\hbar\mathbf{k}/(4\pi/\omega_m)$.

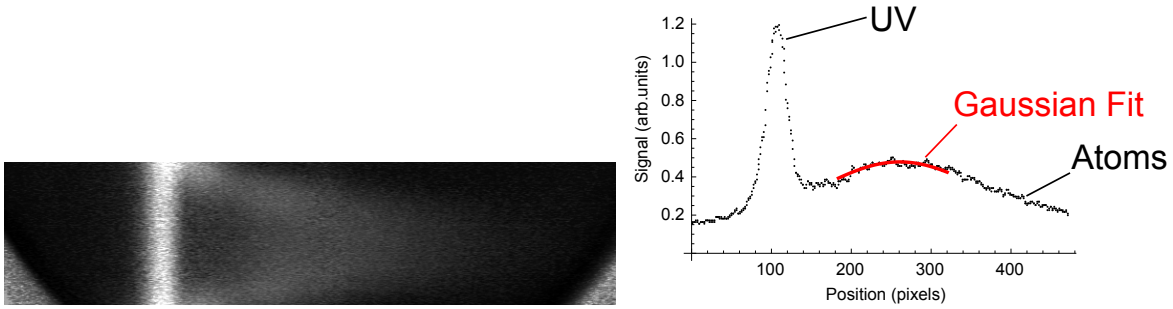

(a) (b)

Figure 6.1: Part (a) shows an image of a phosphor screen that is illuminated by electrons amplified by an MCP that are emitted by the impact of He* atoms and uv light from the source discharge. The bright vertical line is the image of a 250 μm slit that is used to define the transverse velocity of the He* atoms. Since the atom displacement is $\propto 1/v_l^2$, the atoms appear to be horizontally smeared out in the region of strong deflection.

An image of the atomic distribution is viewed 33 cm downstream from the interaction region for particular laser parameters as shown in Fig. 6.1a. A line-out, shown in Fig. 6.1b, is taken from the image by averaging over 11 rows of pixels and contains both atoms and uv light from the source discharge. Under the assumption that a constant force F is applied to an atom with mass m and over a time t_{int}, the final transverse atomic velocity should be

$$v_t = \frac{F}{m} \cdot t_{int} = \frac{F}{m} \frac{L_{int}}{v_l} \tag{6.1}$$

where $L_{int} = 4$ mm is the interaction length, and v_l is the longitudinal velocity of the atoms. The longitudinal velocity distribution is measured by TOF [63]. F can be calculated by measuring the deflection x of the atomic beam on the MCP/PS detector,

$$X = v_t \cdot t_{flight} = \frac{F}{m} \frac{L_{int}}{v_l} \frac{L_{flight}}{v_l} \tag{6.2}$$

where the time of flight is denoted t_{flight}. The flight time in this experiment is determined by

the 33 cm flight distance, L_{flight}, and the longitudinal velocity. By Eq. 6.2 X is proportional to the inverse square of v_l. Therefore the inverse square of the v_l distribution is required to obtain the corresponding X distribution. The characteristic force F due to ARP is calculated using the peak displacement X_{peak} and the peak of the v_l^{-2} distribution v_p. The v_l^{-2} distribution is calculated from the distribution of v_l and its profile is plotted in Fig 6.2 with a v_p of 1080 m/s (different from peak velocity of the v_l distribution).

The peak displacement of the atomic distribution is found by fitting a Gaussian to the measured atomic distribution (Fig. 6.1b) and subtracting that value from the position of the peak of the UV distribution. The magnitude of the ARP force may then be calculated from Eq. 6.2 using v_p. However, a more accurate way to determine F is to measure X_{peak} of the ARP force, measure X_{peak} of the maximum radiative force over the same interaction length, and then take the ratio of the two measurements. The resulting number tells how many times larger F is than F_{rad} directly. Both methods of measuring F agree with each other but there is less uncertainty in the ratio technique. All measurements of F will be in reported units of F_{rad} or F_{ARP}.

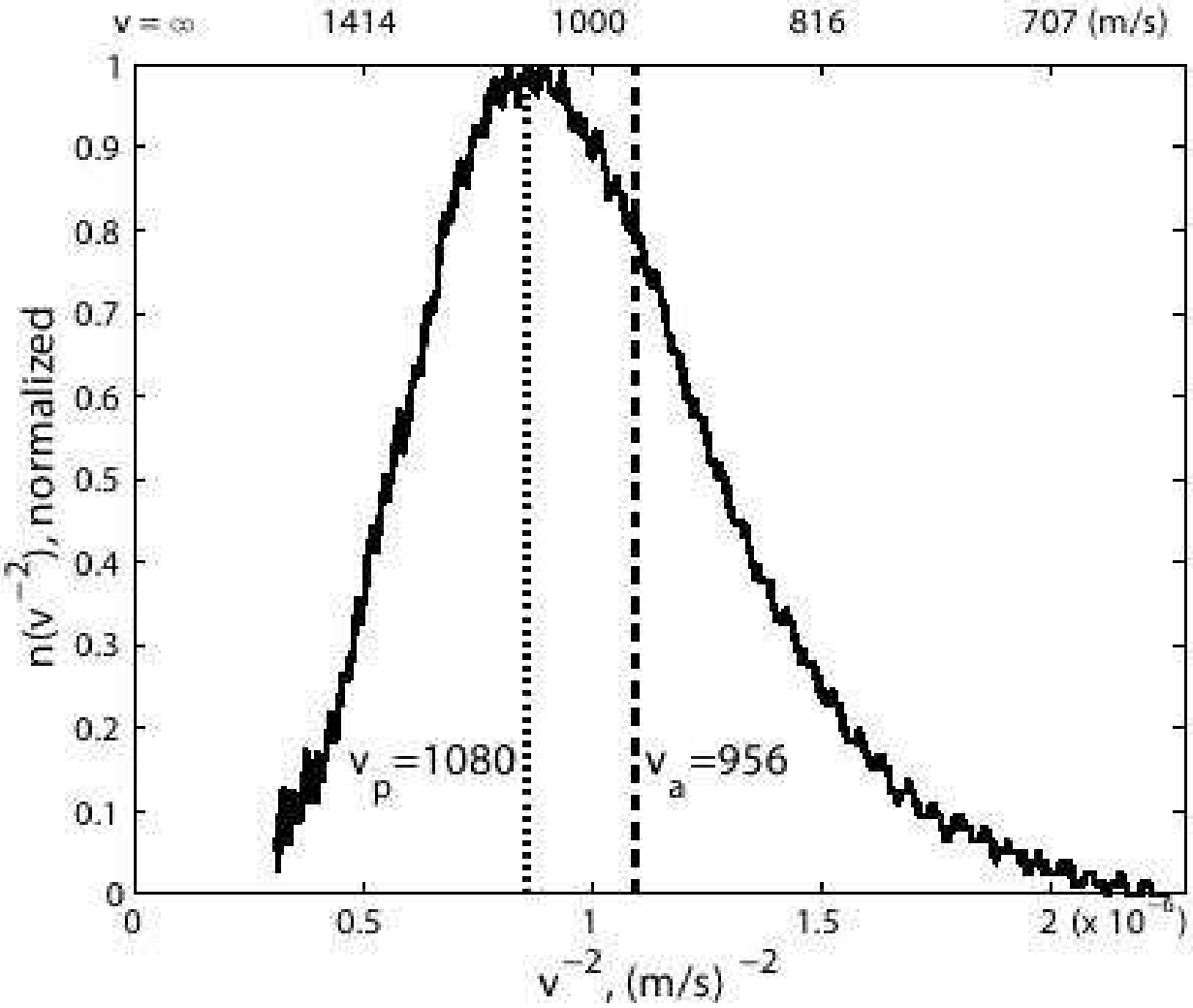

Figure 6.2: Probability distribution function of the $1/v_l^2$ distribution normalized to a peak value of 1. The parameters v_p and v_a are the peak and average of the distribution.

6.2 ARP Force at Atomic Resonance

Large optical forces are only possible for certain combinations of Ω_0 and δ_0 in the non-adiabatic parameter range. This range has been carefully studied numerically and has shown that such large forces are indeed possible [10, 29]. It has also been shown experimentally that large optical forces can be produced with retro-reflected light [9]. However, since it may be desirable to have two independent beams, we present here our study of the ARP force in the $v = 0$ regime with different frequency sweep direction protocols.

It is natural to systematically study the dependence of F on the chirping amplitude δ_0 and pulse amplitude Ω_0, resulting in a measurement of the force in a two dimensional parameter space we call a force map. In Fig. 6.4 we plot the measured force in units of the radiative force as a function of both δ_0 and Ω_0 for various sweep protocols, with both of the frequency sweeps centered about atomic resonance. The chirp and pulse amplitudes are varied by a Pascal-based program communicating via GPIB with the HP8567D signal generator driving the phase modulators and the 4 W fiber amplifiers respectively. During these measurements the protocol was to start by fixing the sweep direction (sign of chirp) and the Rabi frequency of each beam to $\Omega_0 = \Omega_{Max}$ (roughly 4.1 ω_m), while increasing the chirp frequency range from zero to $\pm 5\omega_m$ in 80 steps. A single image of the deflected atoms on the phosphor screen is captured and saved at each step and the set of 80 steps constitutes a row on a single force map (details of image capture can be found in Sec. 4.4). The power in the optical beams is then reduced by changing the current in the 4 W fiber amplifiers so that $\Omega_0 = \Omega_{Max} - \Omega_{step}$ (typically 0.15 ω_m). The chirp amplitude is swept again and a new set of 80 images is taken. This process is repeated many times with decreasing Ω_0 until $\Omega_0 \approx \omega_m$.

Fig. 6.4 shows large regions of parameter space with forces much greater than the radiative

force and agrees qualitatively with our numerical calculations shown in Fig. 2.3. The peak forces for each plot were very nearly 10 times the radiative force. The same sweep direction plots show very good agreement with numerical simulations up to a small scaling factor for δ_0. Discrepancies between the various frequency sweep protocols, the smaller than predicted maximum force, and the scaling of δ_0 may be attributed to non-ideal pulse shapes. Nonlinear effects in the phase modulators and fiber amplifiers may also play a role in the observed deviations of the ARP force from the predictions of the numerical calculations.

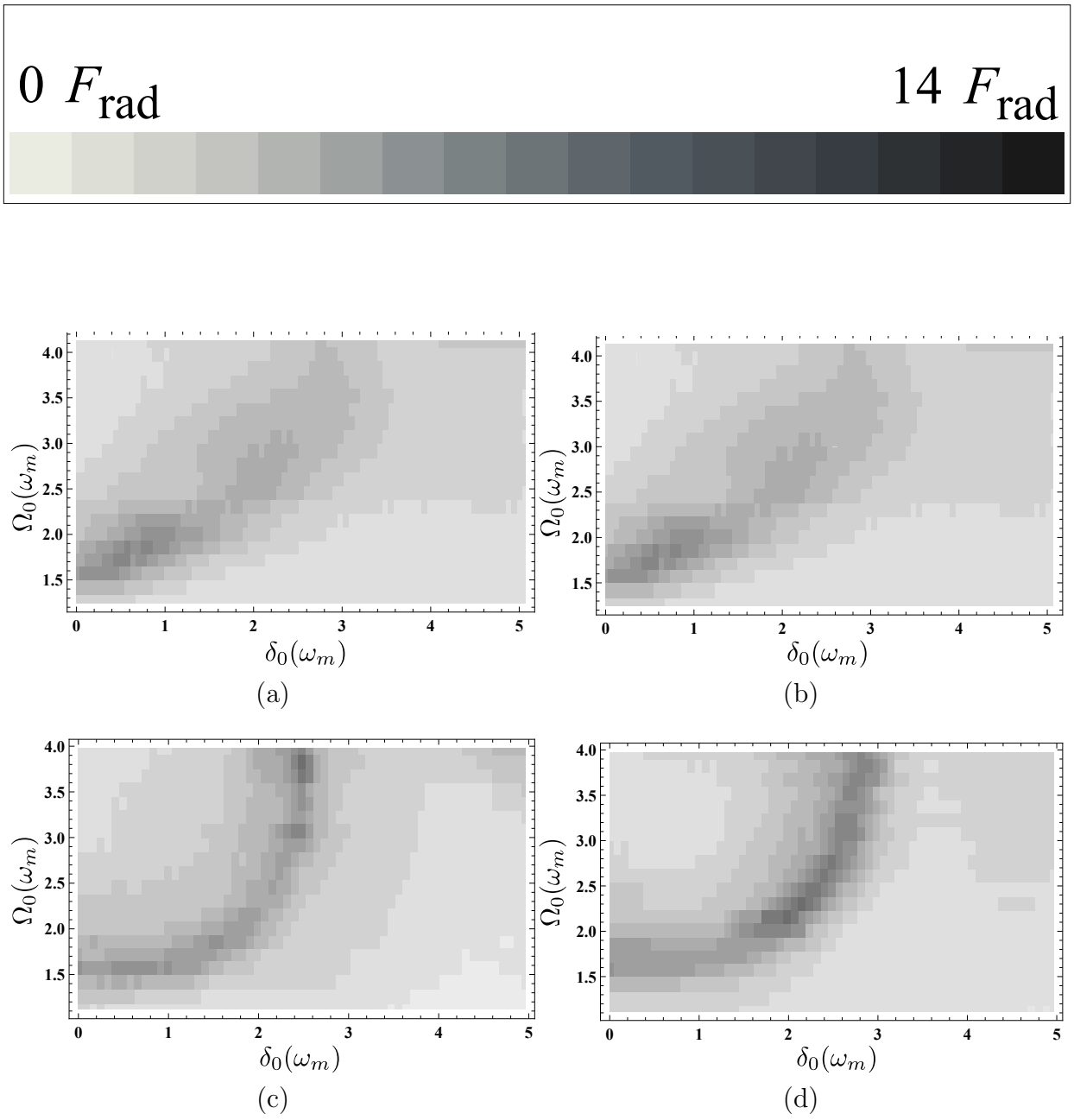

Figure 6.4: Relief plots of the force measured over the experimental parameters Ω_0 and δ_0. Lighter regions correspond to larger forces up to a maximum of $\sim 10 F_{rad}$. The top row portrays opposite frequency sweep directions (Down-Up and Up-Down respectively), and the bottom shows same frequency sweep directions (Down-Down and Up-Up respectively).

6.3 Force *vs.* Velocity

6.3.1 Fixed Velocity Measurements

This subsection describes the ARP force as a function of the atomic velocity simulated by using the apparent Doppler shift of detuned, chirped, counter-propagating laser pulses. The force at a particular atomic velocity (δ/k) to be measured was chosen by locking the diode laser at frequency δ from atomic resonance and using the frequency shift from an AOM to make optical beams with frequencies $\pm\delta$ as seen in Fig. 5.13. Thus $\pm\delta$ is the center of the frequency sweep of each optical beam, which is not related to the amplitude of the frequency sweep δ_0. A force map is made as described in the previous section and the process is repeated many times with different values of δ and different sweep protocols. From these measurements a force *vs.* velocity plot can be made for a particular sweep protocol, δ_0, and Ω_0.

Fig. 6.5 shows the ARP force as a function of atomic velocity for nearly the same values of δ_0 and Ω_0 but different signs of the frequency chirp. Fig. 6.5a has the sweep protocol Down-Down and a peak force of 12 F_{rad} at -0.1 δ_0/k (-50 m/s). Fig. 6.5b (Up-Up) shows similar properties except that it is peaked at +0.1 δ_0/k (+50 m/s). These velocities should be very well known as their uncertainties are tied to the uncertainty of the frequency of the RF signal driving the AOM's used to produce the separate optical beams. A force profile peaked at $v \neq 0$ is further confirmation that the frequency spectrum of the chirped pulses are not symmetric about atomic resonance as seen in Fig. 5.10c.

Though no single effect seems likely to explain these offsets from $v = 0$, nonlinear processes in phase modulation and optical amplification, as well as the Zeeman effect (Sec. 1.3) could offer a partial explanation. The RF fields applied to the phase modulators may induce nonlinear changes in the index of refraction causing deviations in the frequency sweep from

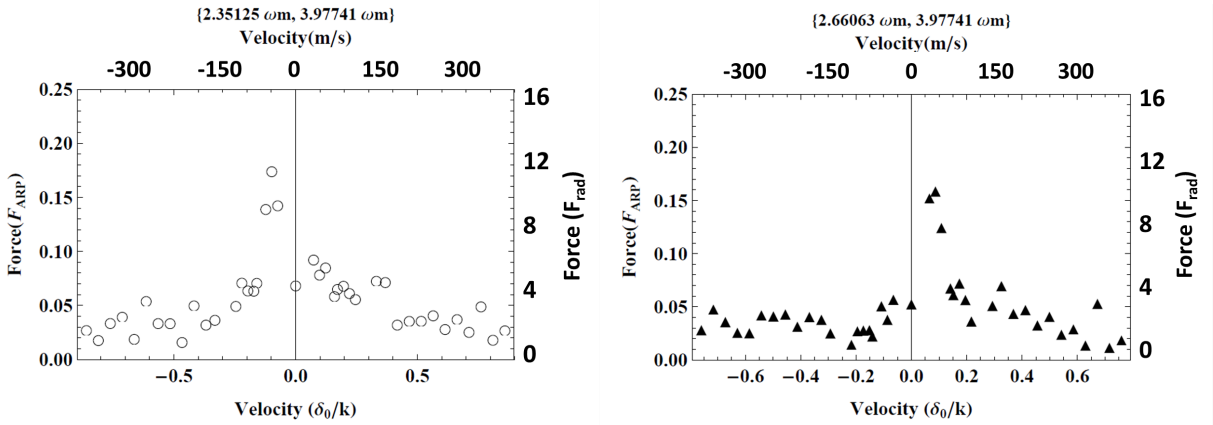

(a) (b)

Figure 6.5: ARP force as a function of simulated atomic velocity labeled by (δ_0, Ω_0). Plots (a) and (b) are frequency sweeps Down-Down and Up-Up respectively with each point corresponding to a single measurement. The maximum force measured is $\approx 12\ F_{rad}$ (75% of the maximum predicted force) and the distributions have an approximate FWHM of 150 m/s.

the desired half cosine shape. Each ARP beam is modulated using a separate phase modulator and these may have slightly different nonlinear characteristics. Also, nonlinearities in the optical amplifiers may change the characteristic frequency spectrum of the ARP beams if the intensity profiles are asymmetric. These nonlinearities are driven by the high optical intensity. Finally, the laser is locked to atomic resonance, not the frequency shifted (≈ 20 MHz) resonance in the interaction region with a magnetic field due to the Zeeman effect. This leaves a puzzle since each of these effects may partially contribute to the measured plots in Fig. 6.5, but none of these mechanisms depend on the sign of the frequency chirp.

Besides experimental "dirt" effects, another possible explanation could be spontaneous emission as seen in Fig. 2.8a. Atoms may undergo more or less spontaneous emission depending on their Doppler shift and the relative sign of the chirp. A brief discussion describing the dynamics of this process in the Bloch sphere picture is given in Sec. 2.3. The shift of the peak force in numerical and experimental plots (Fig. 2.8 and Fig. 6.5) is $\approx 0.1\ \delta_0/k$

though it should be mentioned the widths of these plots differ significantly. Spontaneous emission may be the origin of this velocity shift but either the numerical model is insufficient to describe experimental ARP or imperfections in the experimental setup may reconcile the large discrepancies between the two force *vs.* velocity distributions.

The magnitude and velocity range of the ARP force is much greater than that of the radiative force. The velocity range should increase with Ω_0 and δ_0 in the π-pulse regime. Seen in Fig. 6.7 is the average ARP force over a fixed velocity range ($\pm$380 m/s) as a function of sweep protocol and pulse parameters. Each of these plots has a roughly linear shape with approximately the same slope. The quantity $\sqrt{\Omega_0^2 + \delta_0^2}$ is a natural choice as a scaling factor for the width of the force *vs.* velocity distribution in the π-pulse regime as it is somewhat akin to a time-averaged generalized Rabi frequency. This is an oversimplification of the physics but seems to be a good rule of thumb in the non-adiabatic regime. In each plot of Fig. 6.7 there seems to be a slight saturation effect that may correspond to the change over to the adiabatic regime. When ARP is truly adiabatic it is typically δ_0 alone that acts as the scaling factor as in the simple picture given by Sec. 2.2.2.

6.3.2 Strong Forces Far From Zero Velocity

Beyond the pulse parameters that have a large force peaked near $v = 0$ there are many other combinations of δ_0 and Ω_0 which can lead to very interesting force *vs.* velocity profiles. Fig. 6.8 shows one of these interesting profiles that has a definite double peak structure where the peaks occur at approximately -80 m/s and +220 m/s (-0.12 δ_0/k and +0.27 δ_0/k respectively). Such structures occurred mostly for sweep directions Up-Up and Down-Down at the largest values of δ_0 and Ω_0 as seen in Figs. B.8-11. In numerical calculations the bimodal structure comes about when moving to the right of red curves shown in Fig. 6.6

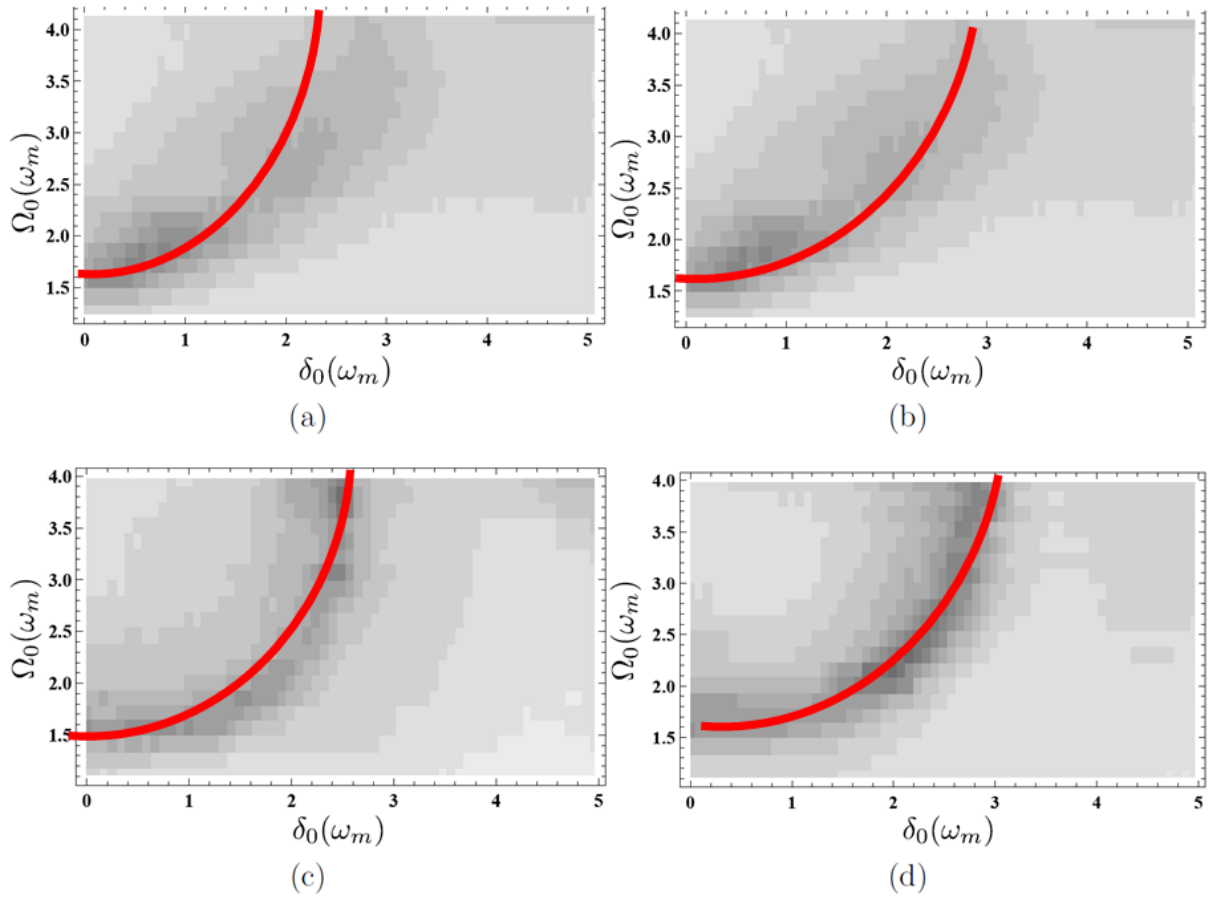

Figure 6.6: Approximate points used in Fig. 6.7 are shown by solid line for each sweep protocol.

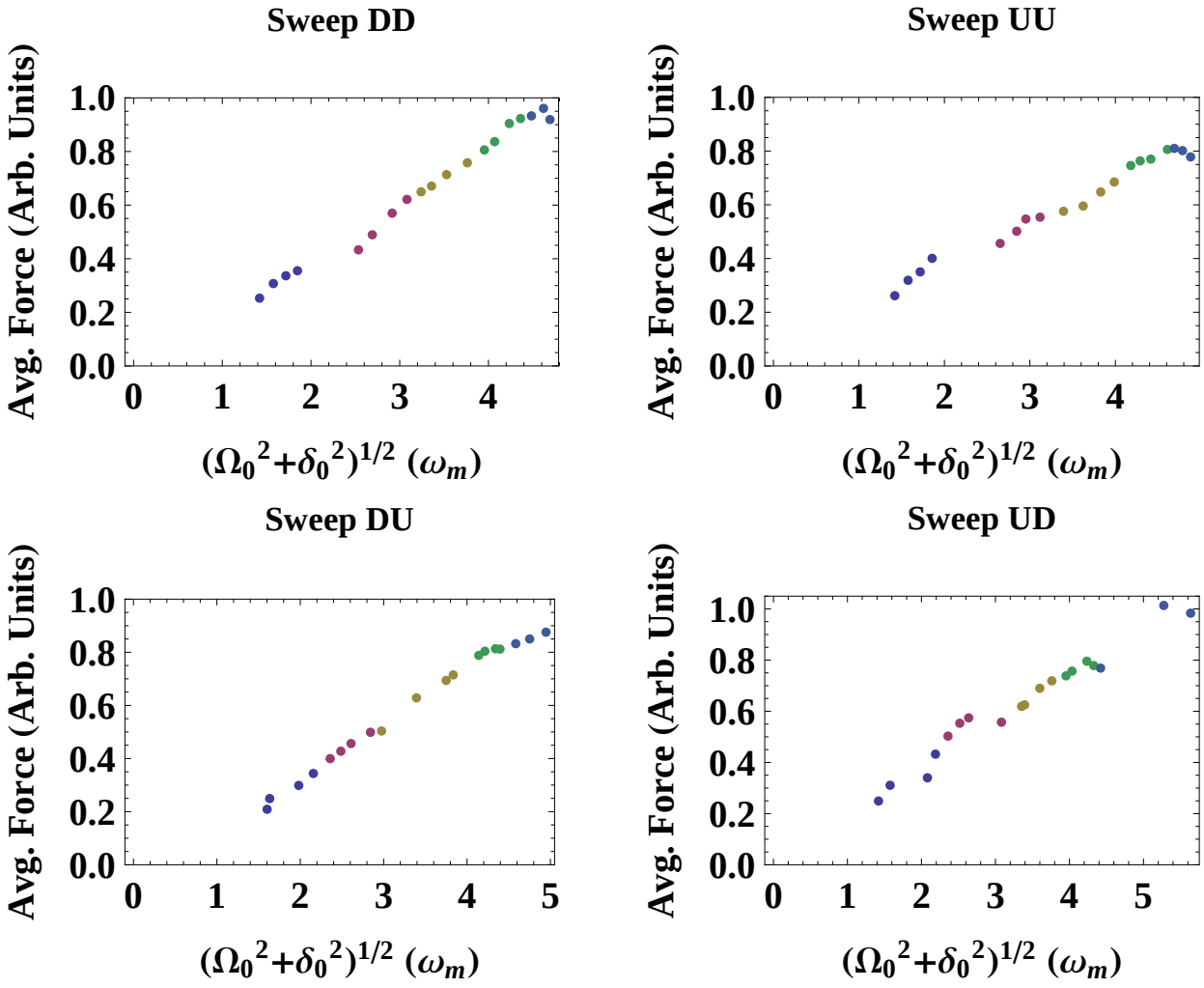

Figure 6.7: Average force integrated from -380 m/s to +380 m/s for each sweep protocol as a function of $\sqrt{\Omega_0^2 + \delta_0^2}$ (ω_m) for velocity distributions peaked near $v = 0$ (see Fig. 6.6).

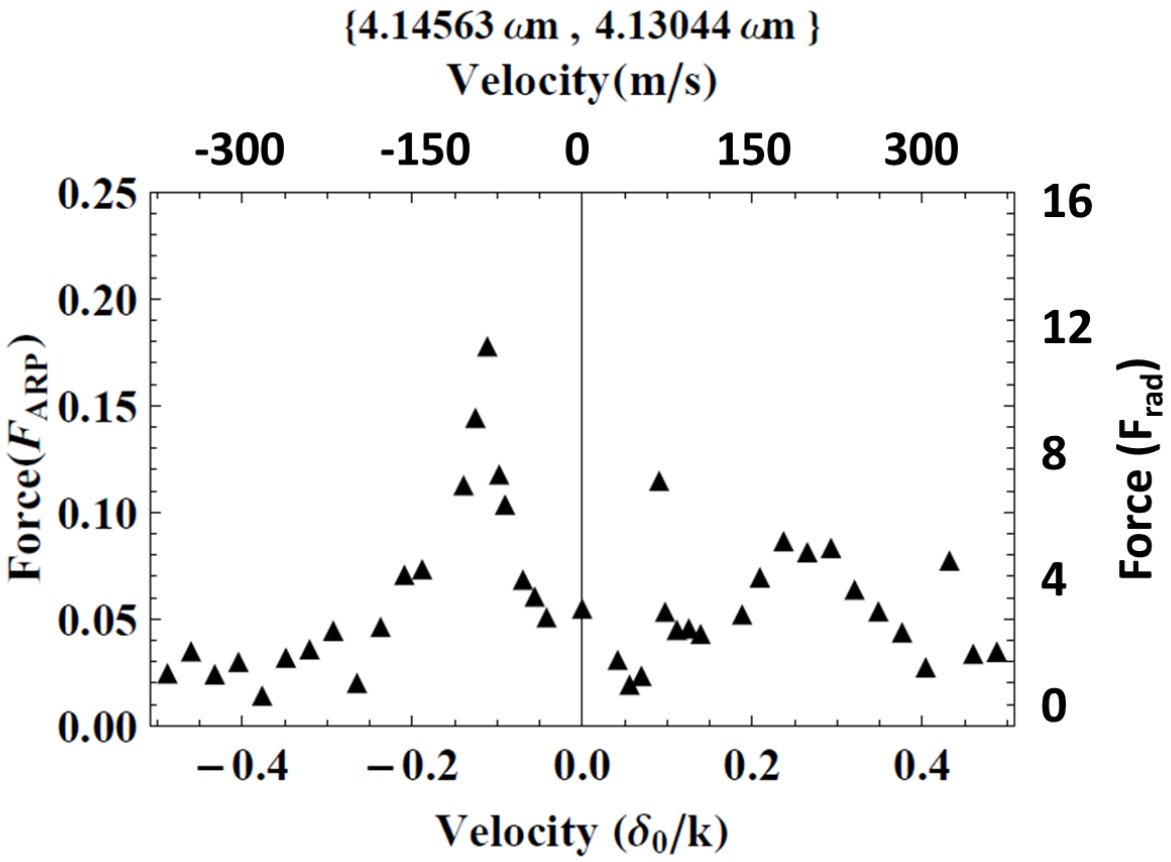

Figure 6.8: A measured force *vs.* velocity distribution with two distinct peaks.

(increasing δ_0). Starting from a force profile that has a single peak at $v = 0$, increasing δ_0 leads to a symmetric splitting of the distribution that grows larger. A small splitting in a numerical simulation can be seen in Fig. 2.5c.

6.3.3 Variable Velocity Measurements

The previous measurements of the velocity dependence of the ARP force took many weeks to produce just one force *vs.* velocity plot at a particular δ_0, Ω_0, and sweep protocol. The experiment needed to be modified so that these measurements could be made on a

much shorter time scale with many more data points. Details of the changes can be found in Fig. 5.12.

In the modified setup, a particular δ_0, Ω_0, and sweep protocol is chosen arbitrarily. Then the relative frequency of each diode laser is swept by ≈ 600 MHz in opposite directions by applying a slow, periodic, ramp voltage ($f = 0.4$ Hz) to the PZT of each diode's extended cavity mirror and the absolute frequency is measured via SAS of the $2^3S_1 \rightarrow 2^3P_2$ transition in He*. The absorption profile measured via SAS is only ≈ 25 MHz wide but this information, along with the linearity and periodicity of the frequency sweep, allows for accurate determination of the absolute frequency of each laser. At the same time the atomic beam deflection is recorded via the open source program VirtualDub for ~ 1 minute at a frame rate of 30 Hz. From measurements of the applied ramp signals, SAS, and atom deflection a plot like Fig. 6.9 can be created which shows the simulated velocity and ARP force as a function of video frame number. In this figure $v = (\delta_1 - \delta_2)/2k$ where δ_i is the detuning of each laser from atomic resonance. The process can then be repeated with new choices for δ_0 and Ω_0 to make more of these plots. Fig. 6.9 is an example of very preliminary data and it should be noted that more data will be taken in the future to clarify the meanings of these results.

From plots like Fig. 6.9 the force from each half period of the frequency sweep can be overlapped to make one of the plots seen in Fig. 6.10. A single point in one of these plots corresponds to ~ 10 force measurements in a single run located within an ≈ 8 m/s velocity bin. The peak force gets larger as both δ_0 and Ω_0 are increased which is consistent with previous measurements. However, these peak forces are smaller than the previous measurements by $\sim 50\%$. This may be attributable to the preliminary nature of these results as well as the additional technical complications present when using two separate diode lasers that are not locked to a frequency reference. The frequency of the diode lasers

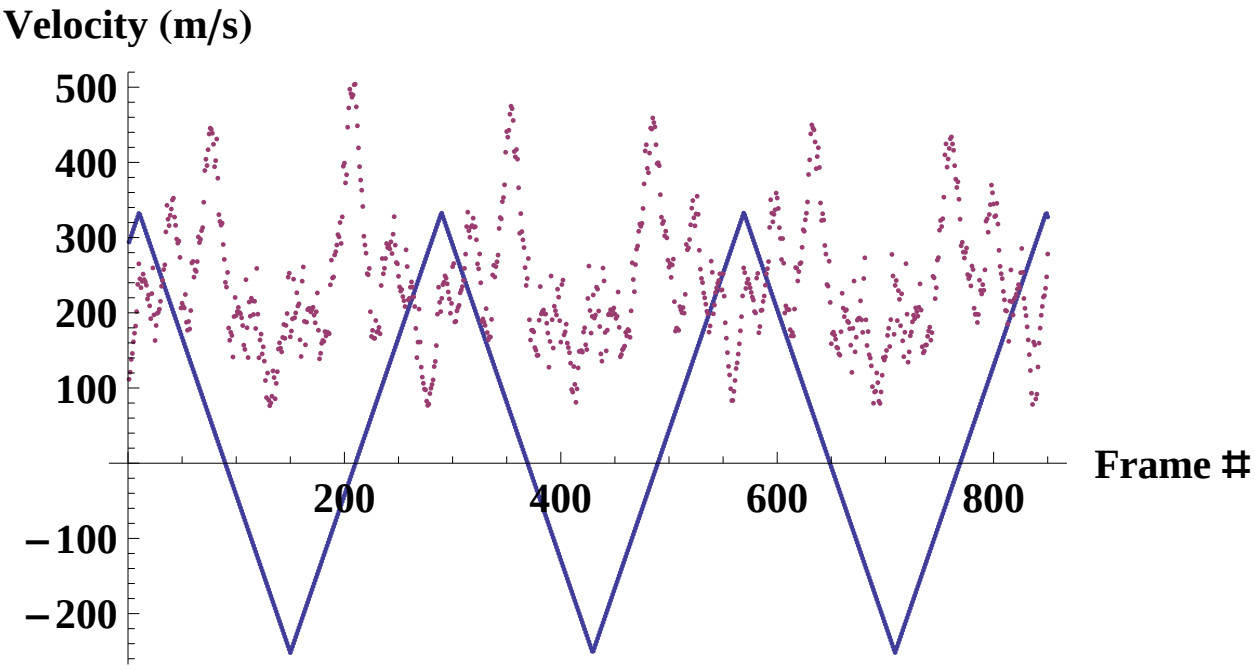

Figure 6.9: ARP force and simulated atomic velocity as a function of video frame number for sweeps Down-Down, $\delta_0 = 3.23\omega_m$ and $\Omega_0 = 3.61\omega_m$. The force and velocity are measured in arbitrary units and m/s respectively. The force minimums do not line up with the velocity extremes as perhaps expected in this figure. This is the result of a slight variation in the frame rate as data is collected and is corrected for in post-processing.

fluctuates by a few MHz on a short time scale due to mechanical vibrations and may drift up to 10 MHz over an entire sequence of measurements due to changes in the room temperature. Besides the magnitude of the forces, the shape of the force *vs.* velocity profiles provides a multitude of information.

The structure of the plots in Fig. 6.10 is quite varied which is interesting by itself. Fig. 6.10a shows the velocity dependence of the ARP force from a train of π-pulses yet the peak force is located at nearly $v = +130$ m/s. There is no simple explanation for why this may be but it may be related to nonlinear effects in the fiber amplifiers. Fig. 6.10b has a relatively broad central peak like that of Fig. 2.5c. While Fig. 6.10c looks very similar to Fig. 6.5b though not as strong. Fig. 6.10d has the largest central peak force but it also has

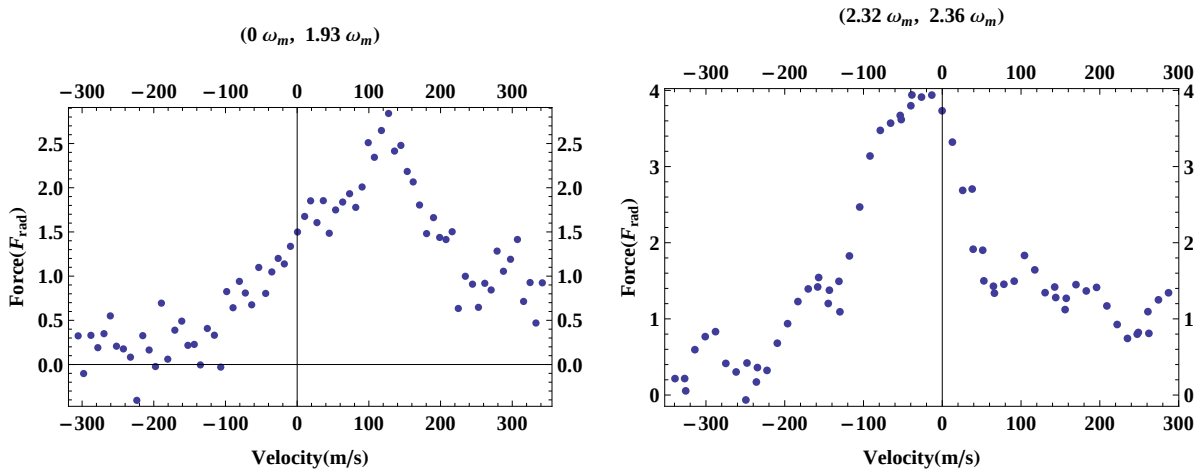

(a) (b) (c) (d)

Figure 6.10: Shown above are plots of the ARP force as a function of simulated atomic velocity labeled by the beam parameters used (δ_0 and Ω_0). Each point corresponds to an average of $\sim$ 10 force measurements located within a $\approx$ 8 m/s velocity bin. The vertical axes are not the same for each plot.

a very strong peak located at $\approx +190$ m/s with a hint of another peak at $\approx +320$ m/s. This may be the strongest side peak but there is clear evidence of modulation of the force profile in each of the plots. The origin of this modulation is a mystery at this time but it may be related to the narrow spikes seen in Fig. 2.4. The widths of the central peaks in each distribution are on the order of $100 - 200$ m/s (170 m/s $\approx 100\gamma/k \approx \omega_m/k$).

Chapter 7

Conclusions

We have experimentally observed very strong optical forces from periodic adiabatic rapid passage sequences resulting from counter-propagating, chirped, light pulses. The slightly smaller absolute value of the forces ($\leq$ 12 F_{rad}) measured relative to the theoretical expectation (16 F_{rad}) can be attributed mostly to the non-ideal pulse shape and nonlinearities of the phase modulator and fiber amplifier. The optical pulses were asymmetric and the tails extended longer than the 3.125 ns required for 25% duty cycle described in Fig. 2.2. Also, the amplitude modulators used in these experiments could only partially extinguish the light during the "dark time" of Fig. 2.2. A residual DC level of as much as 5% of the peak Rabi frequency $\sim$ 100 I_S was always present in each of the optical beams possibly disrupting the coherence of the ARP sequence. Nonlinearities in the phase modulation and fiber amplifiers may have also caused a degradation of the chirped pulse spectrum, leading to a smaller observed force. Despite these difficulties the forces measured were still much larger than the maximum radiative force and agree qualitatively with the theoretical and numerical predictions.

The ARP force is also very effective over a much larger velocity range than the radiative

force. We have mapped out the velocity dependence of the ARP force over a large parameter space including δ_0, Ω_0, and sweep protocol using two different methods. The first method enabled the study of the velocity dependence of the ARP force for many different values of δ_0 and Ω_0. While, the second method allowed us to measure the velocity dependence for a few beam parameters though with much greater resolution. Although the amplitudes and widths of the force *vs*. velocity distributions were not as large as expected from our numerical model, they are still very large when compared to radiative processes.

The numerical and experimental results presented in this dissertation prove that the ARP force has many significant advantages over other laser cooling techniques. The structure of the velocity dependence of the ARP force will continue to be studied in greater detail. Beyond studying the velocity dependence more carefully, there is significant interest in the prospects of creating even larger optical forces by temporally overlapping the ARP pulses [30]. There is also interest in using the ARP to slow an atomic beam of metastable helium. This would potentially be a proof of principle of ARP's ability to both slow and cool neutral atoms which has not been shown previously.

In the past it was difficult to create high intensity, chirped pulses with the high repetition rate required to produce large optical forces via ARP. So, large optical forces from periodic adiabatic rapid passage sequences have only been studied quite recently but it does shows significant potential.

Bibliography

[1] Wineland, D. and Dehmelt, H. *Bull. Am. Phys. Soc.* **20**, 637 (1975).

[2] Hänsch, T. and Schawlow, A. *Op. Comm.* **13**(1), 68–71 (1975).

[3] Wineland, D. and Itano, W. *Phys. Rev. A* **20**(4), 1521–1540 (1979).

[4] Wineland, D., Drullinger, R., and Walls, F. *Phys. Rev. Lett.* **40**, 1639–1642 (1978).

[5] Andreev, S., Balykin, V., Letokhov, V., and Minogin, V. *JETP* **34**, 442 (1981).

[6] Anderson, M., Ensher, J., Matthews, M., Wieman, C., and Cornell, E. *Science* **269**(5221), 198–201 (1995).

[7] Davis, K., Mewes, M.-O., Andrews, M., van Druten, M., Durfee, D., Kurn, D., and Ketterle, W. *Phys. Rev. Lett.* **75**, 3969 (1995).

[8] Williams, M., Chi, F., Cashen, M., and Metcalf, H. *Phys. Rev. A* **60**, R1763–R1766 (1999).

[9] Miao, X., Wertz, E., Cohen, M. G., and Metcalf, H. *Phys. Rev. A* **75**, 011402 (2007).

[10] Stack, D., Elgin, J., Anisimov, P. M., and Metcalf, H. *Phys. Rev. A* **84**, 013420 (2011).

[11] Milonni, P. and Eberly, J. *Lasers.* Wiley, New York, (1988).

[12] Metcalf, H. and van der Straten, P. *Laser Cooling and Trapping.* Springer, New York, (1999).

[13] Miao, X. *Optical Forces on Atoms with Periodic Adiabatic Rapid Passage Sequences.* PhD thesis, Stony Brook University, (2006).

[14] Allen, L. and Eberly, J. *Optical Resonance and Two-Level Atoms.* Dover, New York, (1987).

[15] Phillips, W. and Metcalf, H. *Phys. Rev. Lett.* **48**(9), 596–599 (1982).

[16] Minogin, V. and Serimaa, O. *Op. Comm.* **30**(3), 373 (1979).

[17] Aspect, A., Dalibard, J., Heidman, A., Salomon, C., and Cohen-Tannoudji, C. *Phys. Rev. Lett.* **57**(14), 1688 (1986).

[18] Kazantsev, A. and Krasnov, I. *ZHUETF* **95**(1), 104–113 (1989).

[19] Voitsekhovich, V., Danileiko, M., Negriiko, A., Romanenko, V., and Yatsenko, L. *PIZTEF* **49**(3), 138–140 (1989). [JETP Lett. **49**, 161-164, (1989)].

[20] Grimm, R., Ovchinnikov, Y., Sidorov, A., and Letokhov, V. *Phys. Rev. Lett.* **65**(12), 1415–1418 (1990).

[21] Voitsekhovich, V., Danileiko, M., and Negriiko, A. *ZHUETF* **99**(2), 393–410 (1991). [Sov. Phys. JETP **72**, 219-227, (1992)].

[22] Gupta, R., Xie, C., Padua, S., Batelaan, H., and Metcalf, H. *Phys. Rev. Lett.* **71**(19), 3087–3090 (1993).

[23] Söding, J., Grimm, R., Ovchinnikov, Y., Bouyer, P., and Salomon, C. *Phys. Rev. Lett.* **78**(8), 1420–1423 (1997).

[24] Grimm, R., Wasik, G., Söding, J., and Ovchinnikov, Y. In *Proceedings of the Fermi School CXXXI,* Aspect, A., Barletta, W., and Bonifacio, R., editors, 481 (IOS Press, Amsterdam, 1996).

[25] Goepfert, A., Bloch, I., Haubrich, D., Lison, F., Schütze, R., Wynands, R., and Meschede, D. *Phys. Rev. A* **56**(5), R3354–R3357 (1997).

[26] Reeves, J. *Neutral Atom Lithography Using the 389 nm Transition in Metastable Helium.* PhD thesis, Stony Brook University, (2010).

[27] Foot, C. *Atomic Physics.* Oxford University Press, New York, (2005).

[28] Abragam, A. *The Principles of Nuclear Magnetism.* Oxford Univ. Press, Oxford, (1961).

[29] Lu, T., Miao, X., and Metcalf, H. *Phys. Rev. A* **75**, 063422 (2007).

[30] Demeter, G., Djotyan, G. P., Sörlei, Z., and Bakos, J. S. *Phys. Rev. A* **74**, 013401 (2006).

[31] This can be found at http://www.math.unifi.it/ brugnano/BiM/index.html. It is written especially for stiff, ordinary differential equations and is quite fast and efficient.

[32] Lu, T., Miao, X., and Metcalf, H. *Phys. Rev. A* **71**, 061405 (2005).

[33] Kasevich, M. A., Riis, E., Chu, S., and DeVoe, R. G. *Phys. Rev. Lett.* **63**, 612–615 (1989).

[34] Clairon, A., Salomon, C., Guellati, S., and Phillips, W. D. *Europhys. Lett.* **16** (1991).

[35] Müller, H., Chiow, S.-W., Herrmann, S., Chu, S., and Chung, K.-Y. *Phys. Rev. Lett.* **100**, 031101 (2008).

[36] Durfee, D. S., Shaham, Y. K., and Kasevich, M. A. *Phys. Rev. Lett.* **97**, 240801 (2006).

[37] Pollock, S., Cotter, J. P., Laliotis, A., Ramirez-Martinez, F., and Hinds, E. A. *New J. Phys* **13**(043029) (2011).

[38] Lewoczko-Adamczyk, W. *Bose-Einstein Condensation in Microgravity.* PhD thesis, Universitt zu Berlin, (2009).

[39] Monroe, C., Swann, W., Robinson, H., and Wieman, C. *Phys. Rev. Lett.* **65**(13), 1571–1574 (1990).

[40] Gibble, K., Kasapi, S., and Chu, S. *Op. Lett.* **17**(7), 526–528 (1992).

[41] Lin, Z., Shimizu, K., Zhan, M., Shimizu, F., and Takuma, H. *Jap. J. Appl. Phys.* **30**, L1324–6 (1992).

[42] Chu, S., Hollberg, L., Bjorkholm, J., Cable, A., and Ashkin, A. *Phys. Rev. Lett.* **55**(1), 48–51 (1985).

[43] Prodan, J. and Phillips, W. *Progress in Quantum Electronics* **8**, 231–235 (1984).

[44] Kanzanstev, A. and Krasnov, I. *J. Opt. Soc. Am. B* **6**(2140) (1989).

[45] Liebisch, T., Blanshan, E., Donley, E., and Kitching, J. *Phy. Rev. A* **85**(013407) (2012).

[46] DeMille, D. *Phys. Rev. Lett.* **88**, 067901 (2002).

[47] Andre‘, A., DeMille, D., and Doyle, J., M. *Nature Phys.* **2**, 636 (2006).

[48] Góral, K., Santos, L., and Lewenstein, M. *Phys. Rev. Lett.* **88**, 170406 (2002).

[49] Micheli, A., Brennen, G., and Zoller, P. *Nature Phys.* **2**, 341 (2006).

[50] Barnett, R., Petrov, D., Lukin, M., and Demler, E. *Phys. Rev. Lett.* **96**, 190401 (2006).

[51] Hudson, J. J., Sauer, B. E., Tarbutt, M. R., and Hinds, E. A. *Phys. Rev. Lett.* **89**, 023003 (2002).

[52] DeMille, D., Cahn, S. B., Murphree, D., Rahmlow, D. A., and Kozlov, M. G. *Phys. Rev. Lett.* **100**, 023003 (2008).

[53] Vutha, A. C., Campbell, W. C., Gurevich, Y. V., Hutzler, N. R., Parsons, M., Patterson, D., Petrik, E., Spaun, B., Doyle, J. M., Gabrielse, G., and DeMille, D. *Jour. of Phy. B: AMO Phy.* **43**(7), 074007 (2010).

[54] Isaev, T. A., Hoekstra, S., and Berger, R. *Phys. Rev. A* **82**, 052521 (2010).

[55] Hudson, E. R., Ticknor, C., Sawyer, B. C., Taatjes, C. A., Lewandowski, H. J., Bochinski, J. R., Bohn, J. L., and Ye, J. *Phys. Rev. A* **73**, 063404 (2006).

[56] Flambaum, V. V. and Kozlov, M. G. *Phys. Rev. Lett.* **99**, 150801 (2007).

[57] Barry, J. F., Shuman, E. S., Norrgard, E. B., and DeMille, D. *Phys. Rev. Lett.* **108**, 103002 (2012).

[58] Hodgman, S. S., Dall, R. G., Byron, L. J., Baldwin, K. G. H., Buckman, S. J., and Truscott, A. G. *Phys. Rev. Lett.* **103**, 053002 (2009).

[59] Kawanaka, J., Hagiuda, M., Shimizu, K., Shimizu, F., and Takuma, H. *APPPB* **56**(1), 21–24 (1993).

[60] Mastwijk, H. *Cold Collisions of Metastable Helium Atoms*. PhD thesis, Utrecht University, (1997).

[61] Van Dyck, R. S., Johnson, C. E., and Shugart, H. A. *Phys. Rev. A* **4**, 1327–1336 (1971).

[62] Cashen, M. *Optical Forces on Atoms in Polychromatic Light Fields*. PhD thesis, Stony Brook University, (2002).

[63] Partlow, M. *Bichromatic Collimation to Make an Intense Helium Beam*. PhD thesis, Stony Brook University, (2004).

[64] Hooker, S. and Webb, C. *Laser Physics*. Oxford University Press, New York, (2010).

[65] Avila, C. Master's thesis, Stony Brook University, (1998).

[66] Wieman, C. and Hollberg, L. *Rev. Sci. Instrum.* **62**, 1–20 (1991).

[67] Prevedelli, M., Cancio, P., Giusfredi, G., Pavone, F., and Inguscio, M. *Opt. Comm.* **125**, 231–236 (1996).

[68] Demtröder, W. *Laser Spectroscopy - Basic Concepts and Instrumentation - 3rd Edition*. Springer-Verlag, Berlin, (2003).

[69] Yariv, A. *Optical Electronics*. HRW Saunders, Philadelphia, (1991).

[70] Nagourney, W. *Quantum Electronics for Atomic Physics*. Oxford University Press, New York, (2010).

[71] Yariv, A. *Optical Electronics in Modern Communications*. Oxford University Press, New York, (1997).

[72] Saleh, B. and Teich, M. *Photonics*. Wiley, Hoboken, (2007).

Appendix A

Code for Numerical Calculations

```
!author Daniel Stack and John Elgin
!date 1/24/2011

!description: Definition of Optical Bloch Equations to be solved
!using the BIM subroutine for a fixed Omega_0 and
!delta_0, varying atomic velocity, and random phase

Program force
  Implicit None

! Definition of Fundamental Constants
  double precision pi,lambda,k,hbar,gamma,wm,forfact,velfact
  parameter(pi=4.0*ATAN(1.0),lambda=1083.33E-9,hbar=1.054571E-34)
  parameter(k=2.0*pi/lambda,gamma=1.62E6*2*pi)
```

```
  parameter(wm=160E6*2*pi)        !Modulation Frequency
  parameter(velfact=gamma/k,forfact=hbar*k*gamma)

! Variables
  integer npulses          !Number of pulses
  integer npairs           !Number of pulse pairs
  integer phasepoints      !Number of phi_rel points
  double precision sweep   !Sweep Direction
  double precision d,              !Detuning
                   w,              !Rabi Frequency
                   d0,             !Detuning amplitude
                   w0,             !Peak Rabi frequency
                   minimum,        !minimum d0,w0
                   maximum,        !maximum d0,w0
                   vmin,   !Minimum velocity
                   vmax,   !Maximum velocity
                   dkv,            !Step size in Doppler shift
                   vstep,  !Step size in velocity
                   dopoff,         !Doppler offset
                   offset,         !Velocity offset
                   random,         !Random number
                   times   !Number of times to run program
  double precision :: tpulse = (1.0*pi/wm) !Single pulse duration
  double precision :: p = (4.0*pi/wm)     !Pulse pair sequence duration
```

```
************************************************************************
  !ODE solver parameters
  double precision :: rtol = 1.0E-5
  double precision :: atol = 1.0E-5
  integer i
  integer j
  integer l
  integer m
  integer neqn              !number of differential equations
  double precision h0       !initial step size for ODE solver
  integer lwork, liwork
  parameter(neqn=3)
  parameter(lwork=24+neqn*(48+2*neqn),liwork=37+neqn)
  double precision work(lwork)
  integer iwork(liwork)
  double precision rpar(10) !real parameters for the ODE solving
  integer ipar              !integer parameters for the ODE solving
  integer idid              !return code of the ODE solver
  external feval, jeval, solout
  integer ijac, mljac, mujac, iout
  double precision u(3)          !3rd component of Bloch vector
  double precision v,            !Velocity
                   dF,                 !Change in force
```

```
                tstart ,  !Start time
                tstop ,   !End time
                phi ,             !Phase of torque vector
                phistep ,         !Step-size for phase
                FF,               !Force
                term0             !u(3) at beginning of pulse

**************************************************************************
    Write(*,*) "How many phasepoints?"
    Read(*,*) phasepoints

    Write(*,*) "How many pulse pair interactions?"
    Read(*,*) npulses

    Write(*,*) "What is delta_0? (in units of wm)"
    Read(*,*) d
    d0 = d * wm

    Write(*,*) "What is omega_0? (in units of wm)"
    Read(*,*) w
    w0 = w * wm

    Write(*,*) "What is the minimum value of KV? (in units of gamma/k and if n
    Read(*,*) minimum
```

```
    vmin = minimum * velfact

    Write(*,*) "What is the maximum value of KV? (in units of gamma/k)"
    Read(*,*) maximum
    vmax = maximum * velfact

    Write(*,*) "Doppler Detuning offset, where should the curve be centered? (
    Read(*,*) offset
    dopoff = k*offset * velfact

    Write(*,*) "How many steps in KV?"
    Read(*,*) dkv
    vstep = (vmax-vmin)/dkv
    Write(*,*) "The step size of kv is", vstep/velfact ,"gamma/k"

    Write(*,*) "How many times?"
    Read(*,*) times
!*************************************************************
   do i = 1,14                    !use default parameters for work
   work(i) = 0.0
   end do
   idid = 0
   ijac = 0
   mljac = neqn
```

```
mujac = neqn
iout = 0

iwork(1) = 10E5   !max number of integration steps
iwork(2) = 4      !min order for ode solving process (between 4 and 12)
iwork(3) = 12     !max order for ode solving process (between min order and
iwork(4) = 10
!max number of blended iterations per integration step, method of order 4
iwork(5) = 12
!max number of blended iterations per integration step, method of order 6
iwork(6) = 14
!max number of blended iterations per integration step, method of order 8
iwork(7) = 16
!max number of blended iterations per integration step, method of order 10
iwork(8) = 18
!max number of blended iterations per integration step, method of order 12
*****************************************************************
    rpar(1) = gamma              !Decay rate of population
    rpar(2) = -gamma/2           !Decay rate of coherences
    rpar(3) = w0                 !w0
    rpar(4) = d0/wm              !d0/wm
    rpar(5) = 0.0                !k*v
    rpar(6) = 0.0                !Phase
    rpar(7) = wm                          !Modulation frequency
```

```
    rpar(8) = dopoff              !Doppler offset
    rpar(9) = 0.0                 !Pulse number in sequence

    npairs = 4*npulses          !Pulses per sequence
    term0 = -1.0                          !r3 of Bloch vector

    open(unit=88, file='singlepointrpUU.dat')  !Save file
*****************************************************************
npairs = 4*npulses
term0 = -1.0
phistep=2.0*pi/(phasepoints)            !Step-size for phi_rel


do j=1, phasepoints, 1                          !Phase loop
    phi = phistep*j
    rpar(6) = phi

  do l=1, dkv+1, 1                              !Velocity loop
     v = vmin +(l-1)*vstep
     rpar(5) = k*v

        dF = 0.0                                !Initial conditions
        tstart = 0.0
        FF = 0.0
```

```
 h0 = tpulse/100.0

do m = 1, times

 !initial Bloch vector
 u(1) = 0.0
 u(2) = 0.0
 u(3) = -1.0

 do i = 1, npairs
   tstop = tstart + tpulse

      !Call random phase
       rpar(9) = real(i)
   call init_random_seed
   If (mod(i,4) .eq. 1) then
      call random_number(random)
      rpar(10) = mod(random*2*pi,2*pi)
   End If

      !OBE solver
  call bim(neqn,feval,tstart,tstop,u,h0,rtol,atol,jeval,ijac,&
   mljac,mujac,work,lwork,iwork,liwork,rpar,ipar,iout,idid)
```

```
            If (idid.ne.0) then
                write(*,*) 'ERROR: returned idid=', idid
            End if

               !Force calculation
            If (mod(i,4) .eq. 1) Then
                dF = (u(3)-term0)*hbar*k/(2.0*tpulse)
            Else if (mod(i,4) .eq. 2) Then
                dF = -(u(3)-term0)*hbar*k/(2.0*tpulse)
            Else
                dF = 0
            End If

           FF = FF+dF
           term0=u(3)     !New initial r3

        End do
        End do

!Write results to file
write(88,9999) phi, v/(velfact), FF/(2.0*npulses*forfact*times)

    End do
  End do
```

```
    9999 format(3F20.5)
    stop
End
***************************************************************************

!Subroutine to produce random number

SUBROUTINE init_random_seed()
  INTEGER :: i, n, clock
  INTEGER, DIMENSION(:), ALLOCATABLE :: seed

  CALL RANDOM_SEED(size = n)
   ALLOCATE(seed(n))

  CALL SYSTEM_CLOCK(COUNT=clock)

   seed = clock + 37 * (/ (i - 1, i = 1, n) /)
   CALL RANDOM_SEED(PUT = seed)

   DEALLOCATE(seed)
END SUBROUTINE

!Subroutine implements Optical Bloch Equations (OBEs)
```

```
subroutine feval(neqn,t,u,du,ierr,rpar,ipar)
      integer neqn,ierr,ipar
      double precision t,u(neqn),du(neqn),rpar(10),a,b

      rpar(1) = gamma          !Decay rate of population
      rpar(2) = -gamma/2       !Decay rate of coherences
      rpar(3) = w0             !w0
      rpar(4) = d0/wm          !d0/wm
      rpar(5) = 0.0            !k*v
      rpar(6) = 0.0            !Phase
      rpar(7) = wm                    !Modulation frequency
      rpar(8) = dopoff         !Doppler offset
      rpar(9) = 0.0            !Pulse number in sequence

!First Pulse
 If (mod(idint(rpar(9)),4) .eq. 1) Then

!Omega_real
 a = dabs(rpar(3)*dsin(rpar(7)*t))*dsin(-rpar(4)*dsin(rpar(7)*t)+(rpar(5)
-rpar(8))*t+rpar(6)/2 +rpar(10))

!Omega_imaginary
  b = dabs(rpar(3)*dsin(rpar(7)*t))*dcos(-rpar(4)*dsin(rpar(7)*t)+(rpar(5)
-rpar(8))*t+rpar(6)/2 +rpar(10))
```

```
!Second Pulse
Else If (mod(idint(rpar(9)),4) .eq. 2) Then

!Omega_real
a = dabs(rpar(3)*dsin(rpar(7)*t))*dsin(rpar(4)*dsin(rpar(7)*t)-(rpar(5)
-rpar(8))*t-rpar(6)/2 +rpar(10))

!Omega_imaginary
b = dabs(rpar(3)*dsin(rpar(7)*t))*dcos(rpar(4)*dsin(rpar(7)*t)-(rpar(5)
-rpar(8))*t-rpar(6)/2 +rpar(10))

!Dead time
Else
   a = 0
   b = 0
 End If

!OBE's
   du(1) = rpar(2)*u(1) - a*u(3)
   du(2) = rpar(2)*u(2) - b*u(3)
   du(3) = a*u(1) + b*u(2) - rpar(1)*(u(3)+1.0)

 return
```

```
end

! Subroutine for evaluating the Jacobian of the function
! Just Dummy, since Jacobian is calculated numerically
subroutine jeval (neqn,t,y,jac,ldim,ierr,rpar,ipar)
        integer neqn,ldim,ierr,ipar
        double precision t,y(neqn),jac(ldim,neqn),rpar

        return
end

!Subroutine for output after each step
!Just Dummy, since no output after each step
subroutine solout(m,t,y,f,k,ord,irtrn)
        integer m,k,ord,irtrn
        double precision t(k),y(m,k),f(m,k)

        return
end
```

Appendix B

Force Maps and Force vs kv Plots

B.1 Same Sweep Direction Velocity Dependence

Figure B.1: Legend for Appendix B force maps.

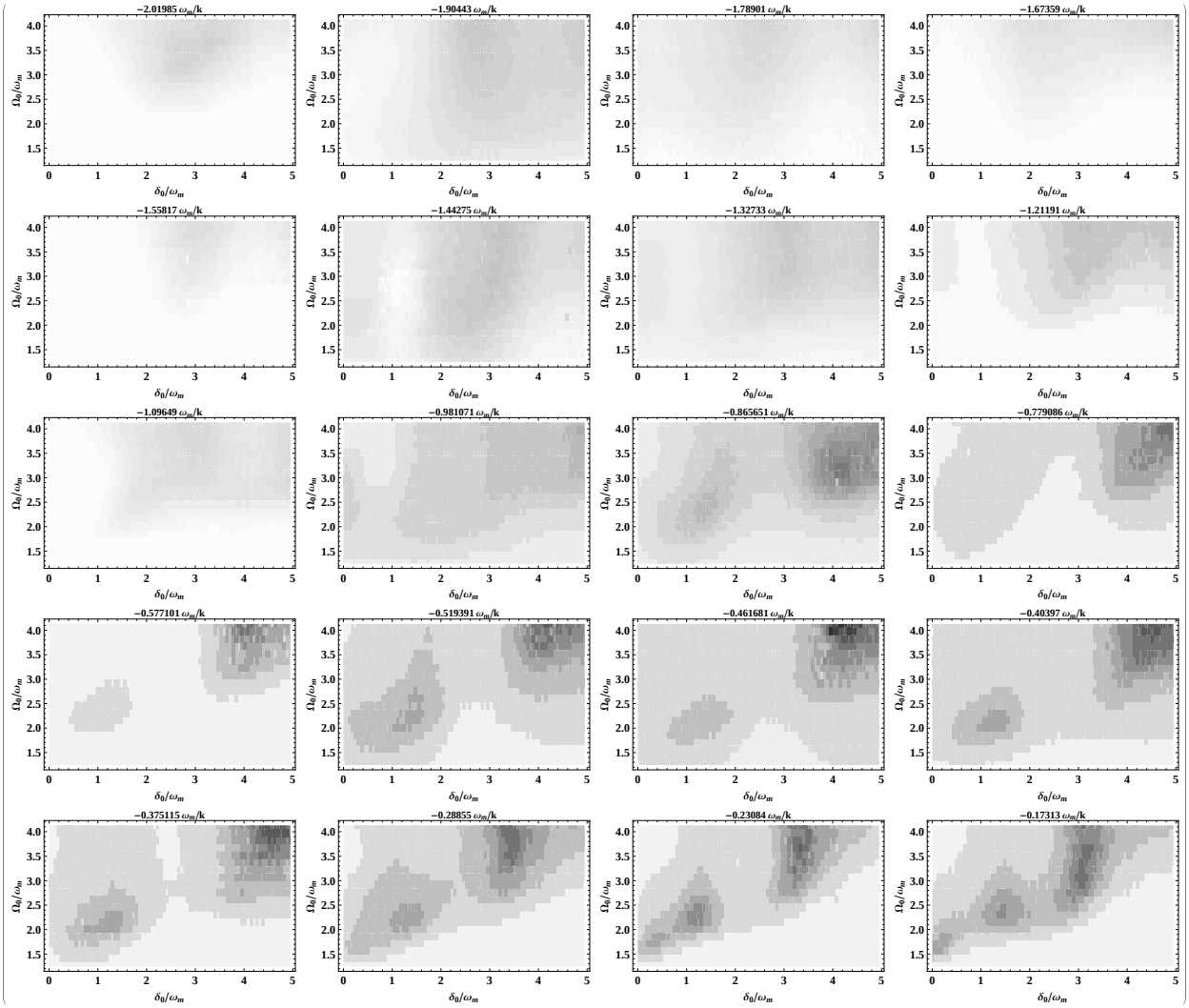

Figure B.2: Force maps for $v < 0$ and sweep directions Up-Up. Plots are labeled with the simulated atomic velocity in units of ω_m/k ($\omega_m/k \approx 170$ m/s)

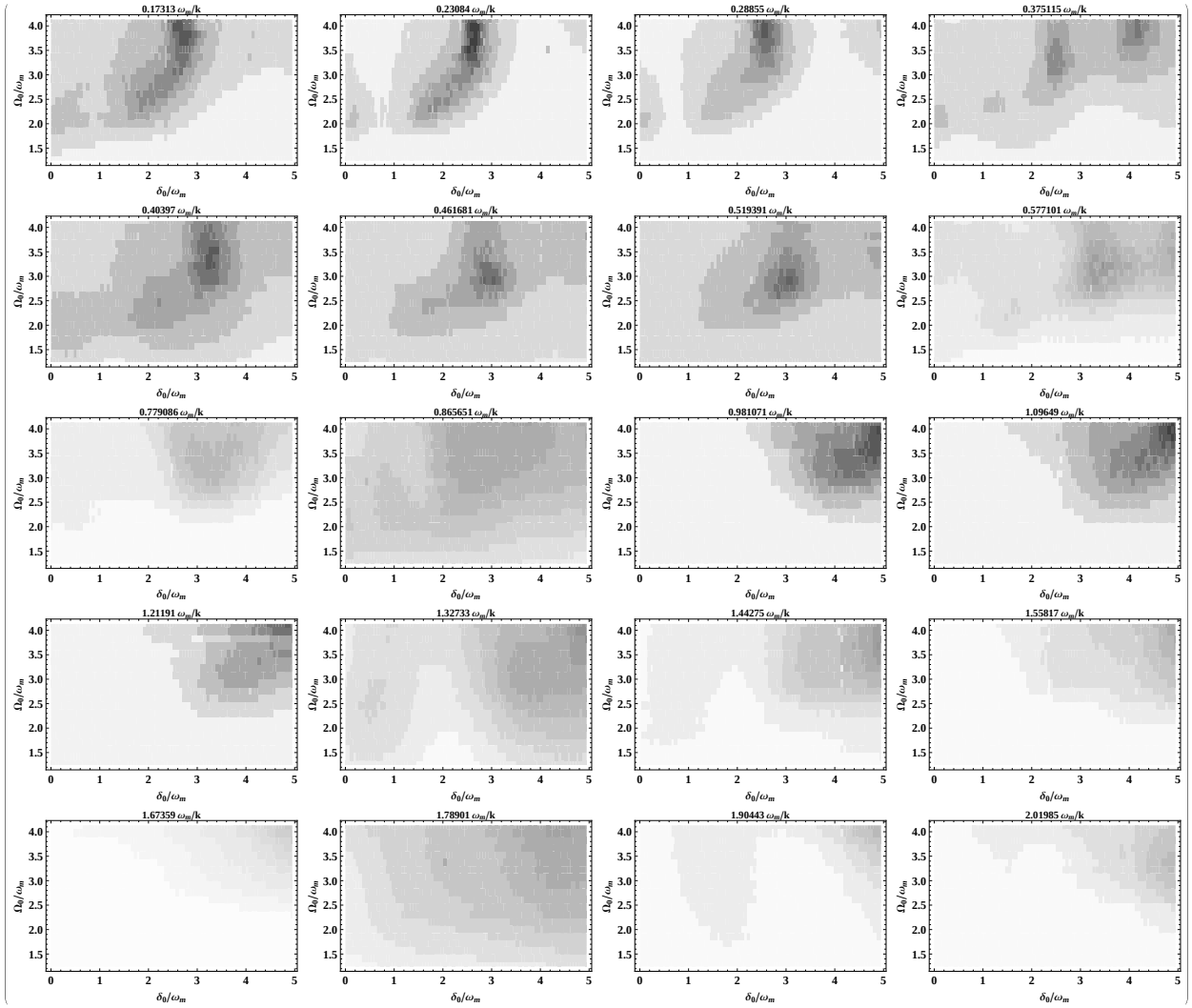

Figure B.3: Force maps for $v > 0$ and sweep directions Up-Up. Plots are labeled with the simulated atomic velocity in units of ω_m/k ($\omega_m/k \approx 170$ m/s)

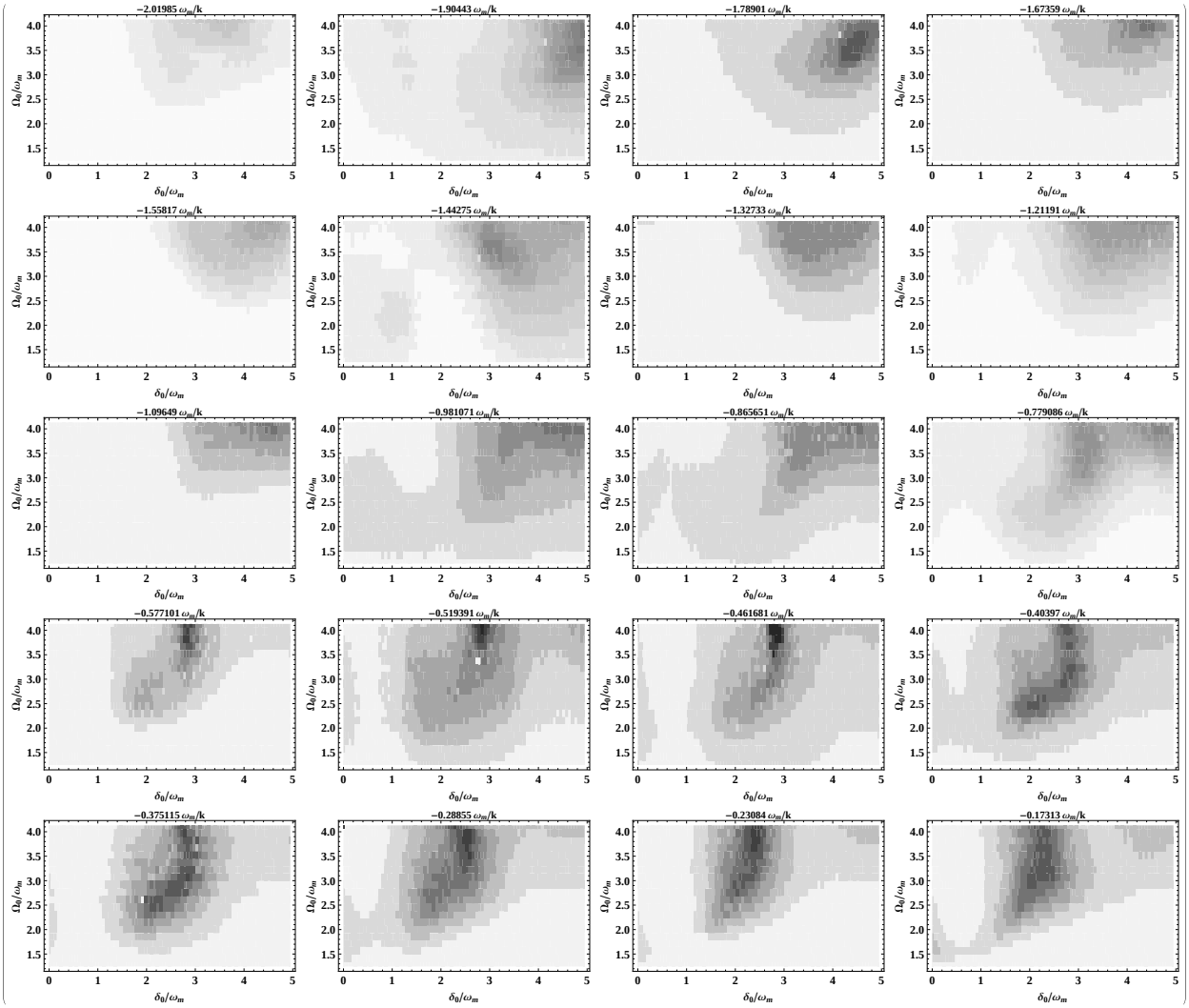

Figure B.4: Force maps for $v < 0$ and sweep directions Down-Down. Plots are labeled with the simulated atomic velocity in units of ω_m/k ($\omega_m/k \approx 170$ m/s)

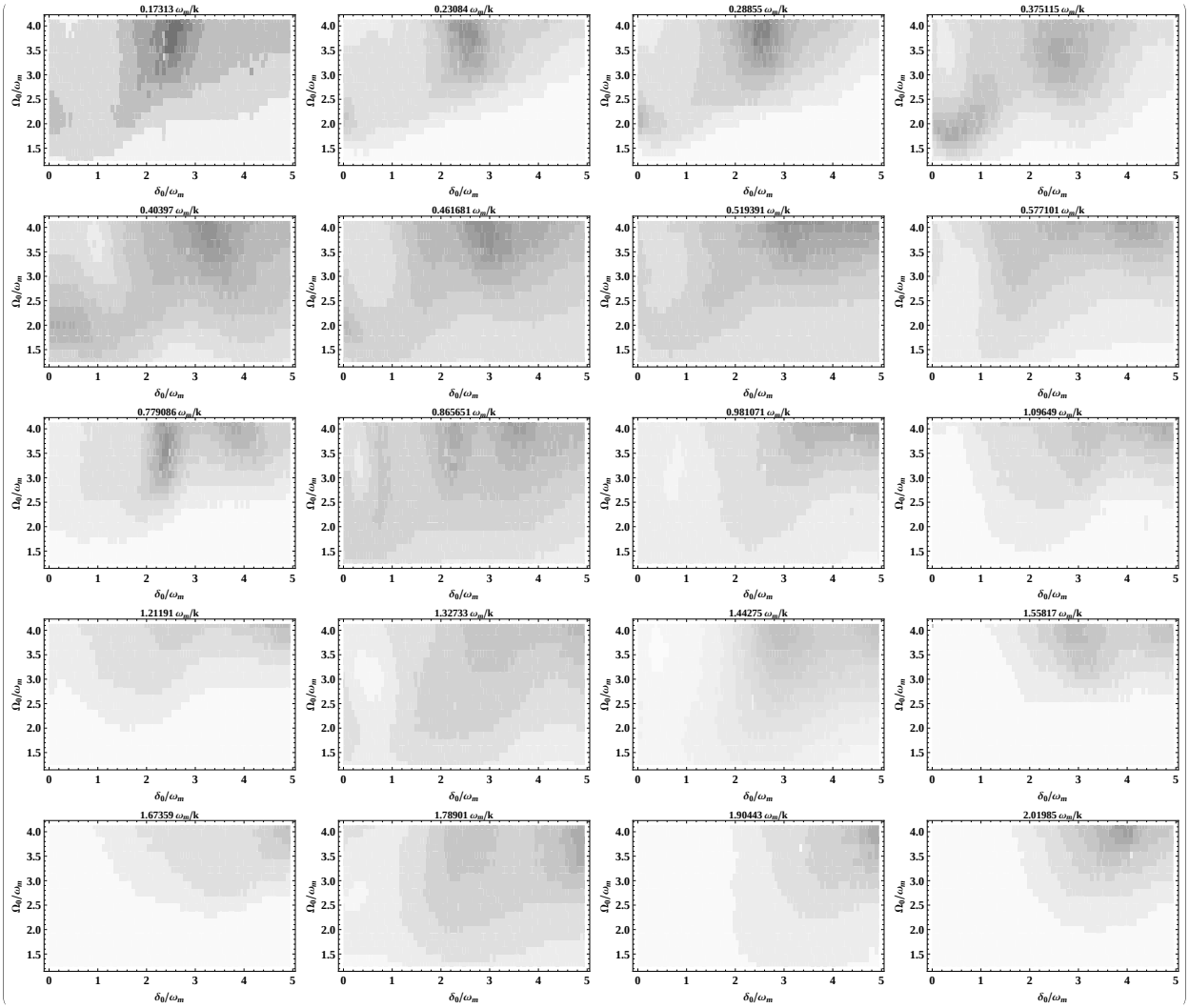

Figure B.5: Force maps for $v > 0$ and sweep directions Down-Down. Plots are labeled with the simulated atomic velocity in units of ω_m/k ($\omega_m/k \approx 170$ m/s)

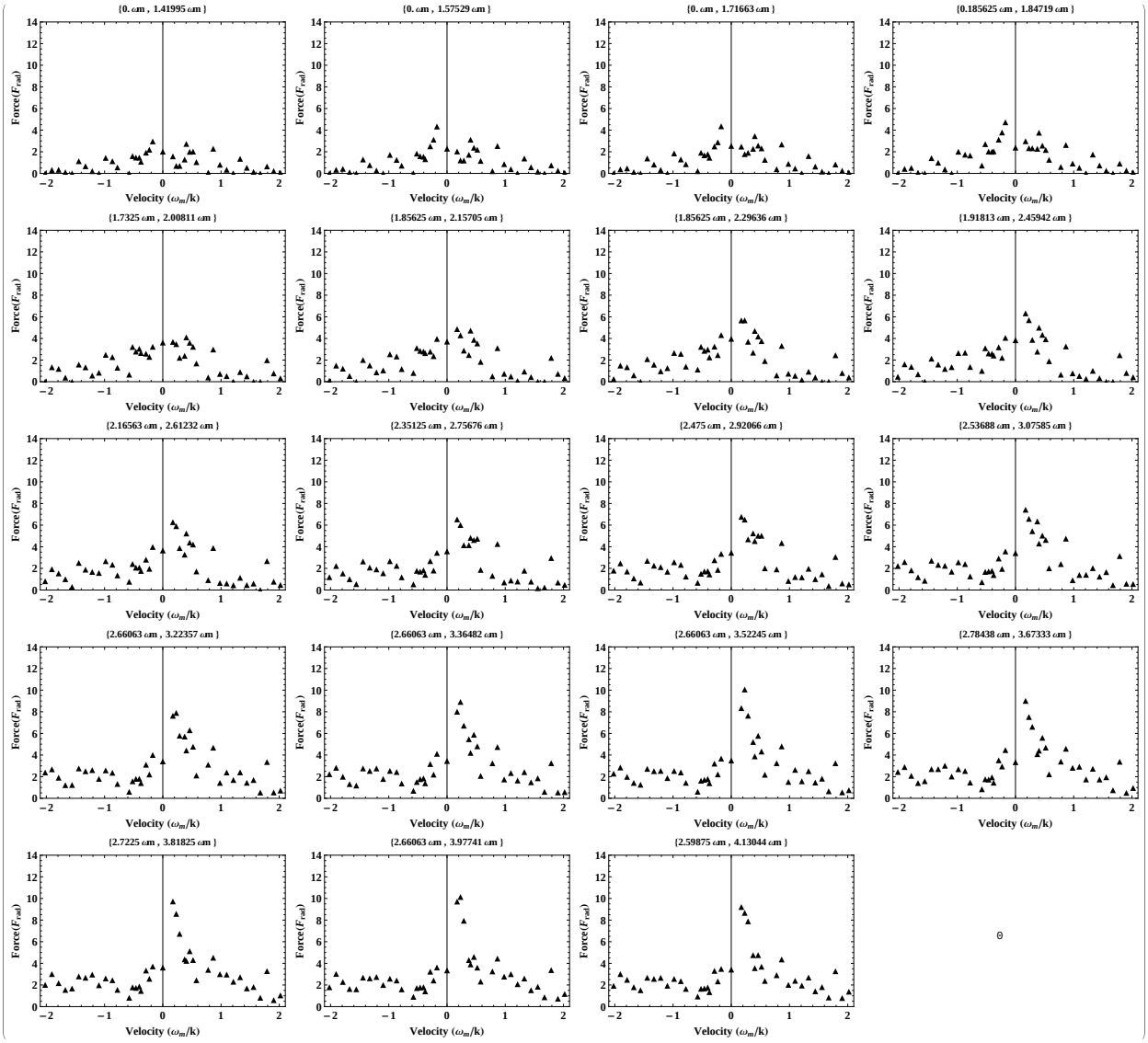

Figure B.6: Force *vs* velocity plots for sweep UU peaked near v = 0. Plots are labeled by $\{\delta_0, \Omega_0\}$.

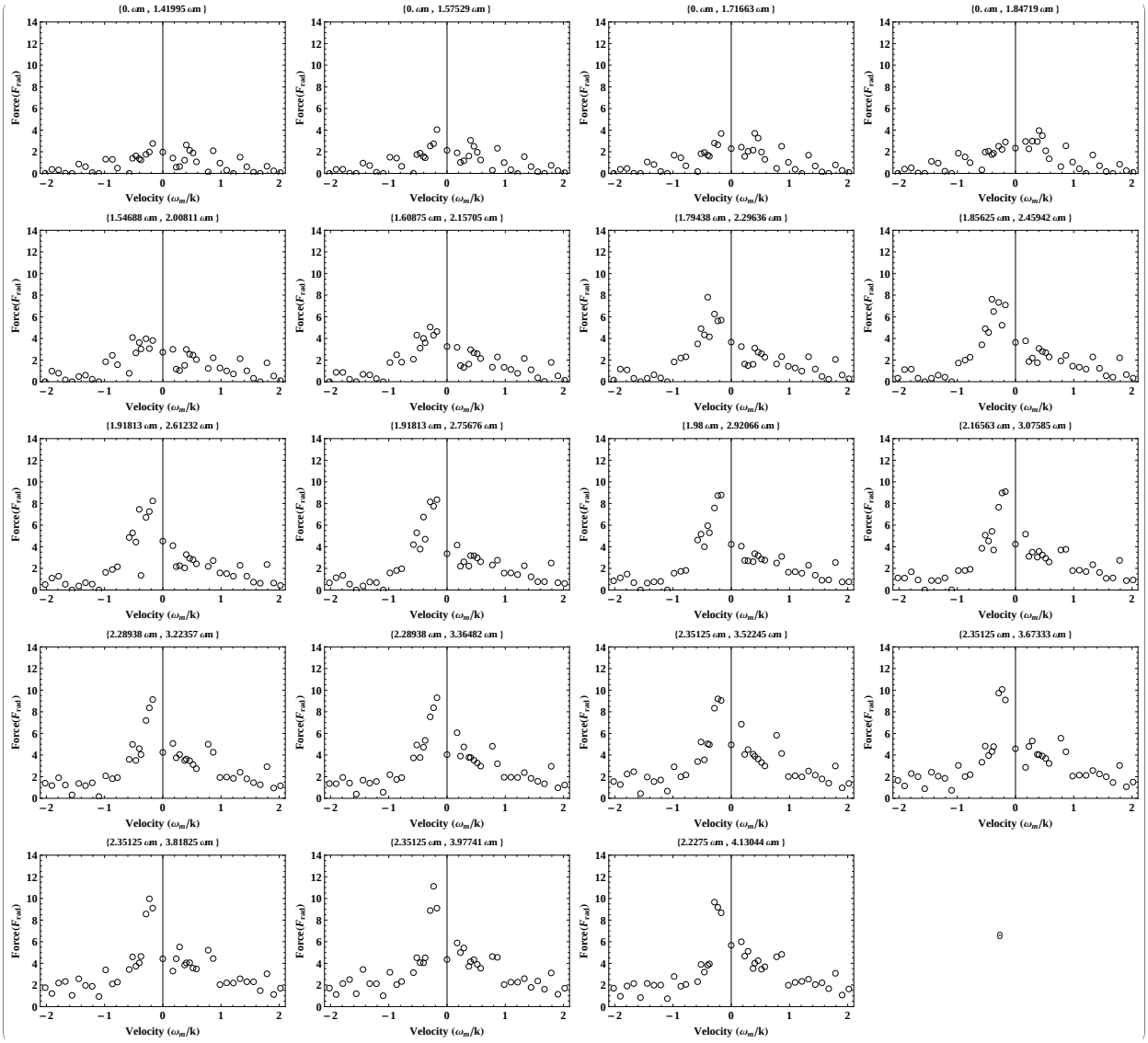

Figure B.7: Force *vs* velocity plots for sweep DD peaked near v = 0. Plots are labeled by $\{\delta_0, \Omega_0\}$.

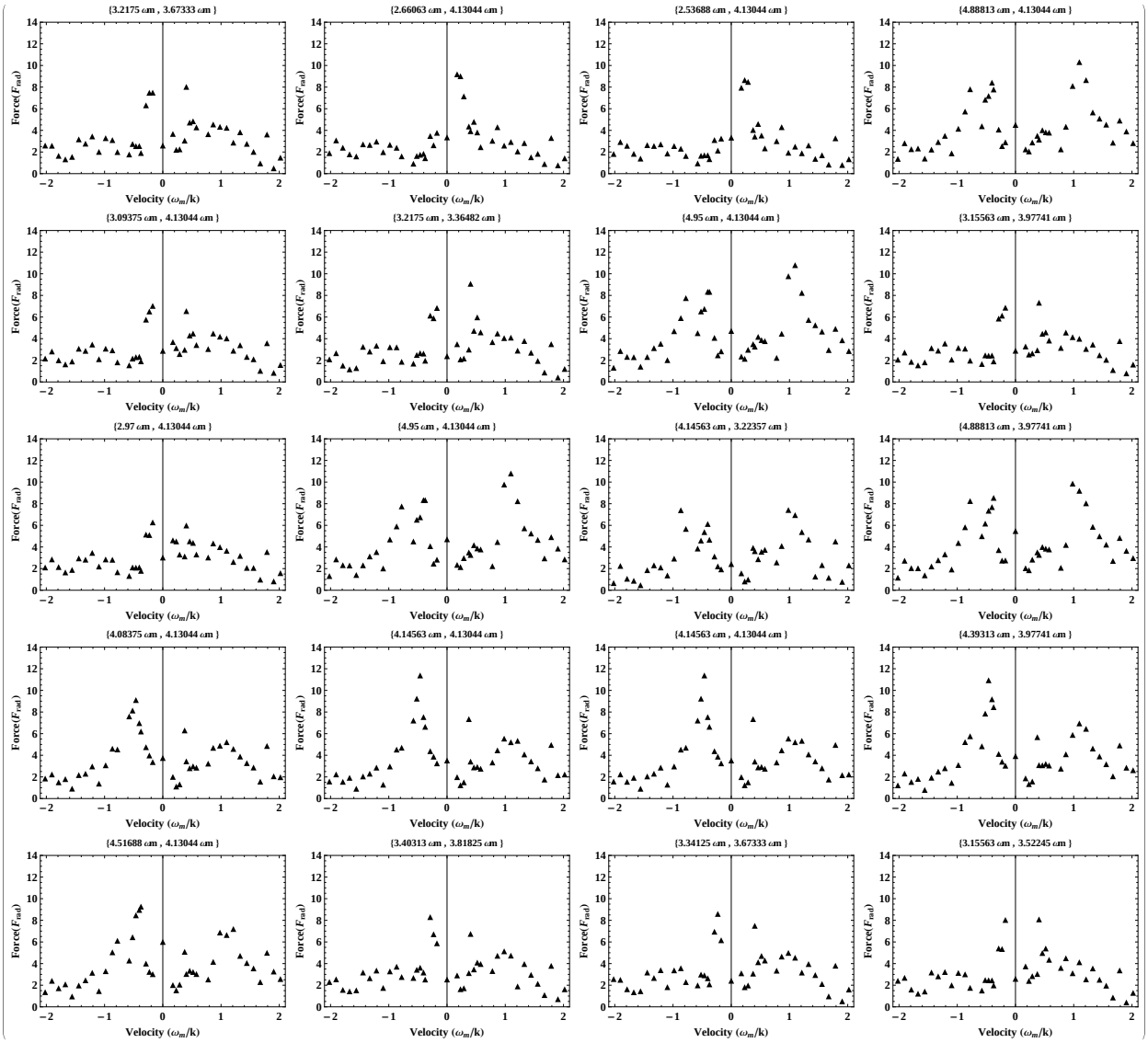

Figure B.8: Selected force *vs* velocity plots for sweep UU. Plots are labeled by $\{\delta_0, \Omega_0\}$.

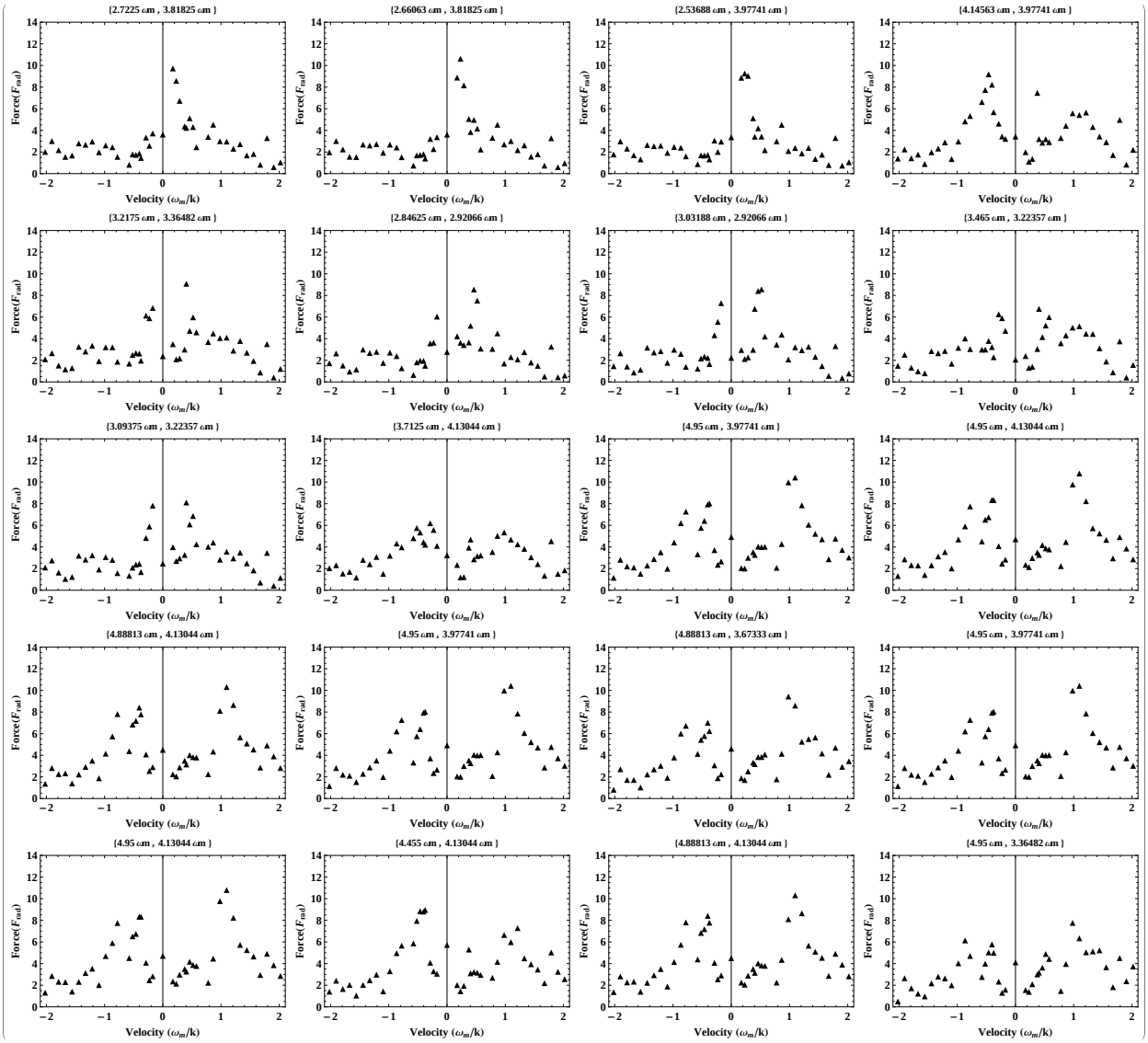

Figure B.9: Selected force *vs* velocity plots for sweep UU. Plots are labeled by $\{\delta_0, \Omega_0\}$.

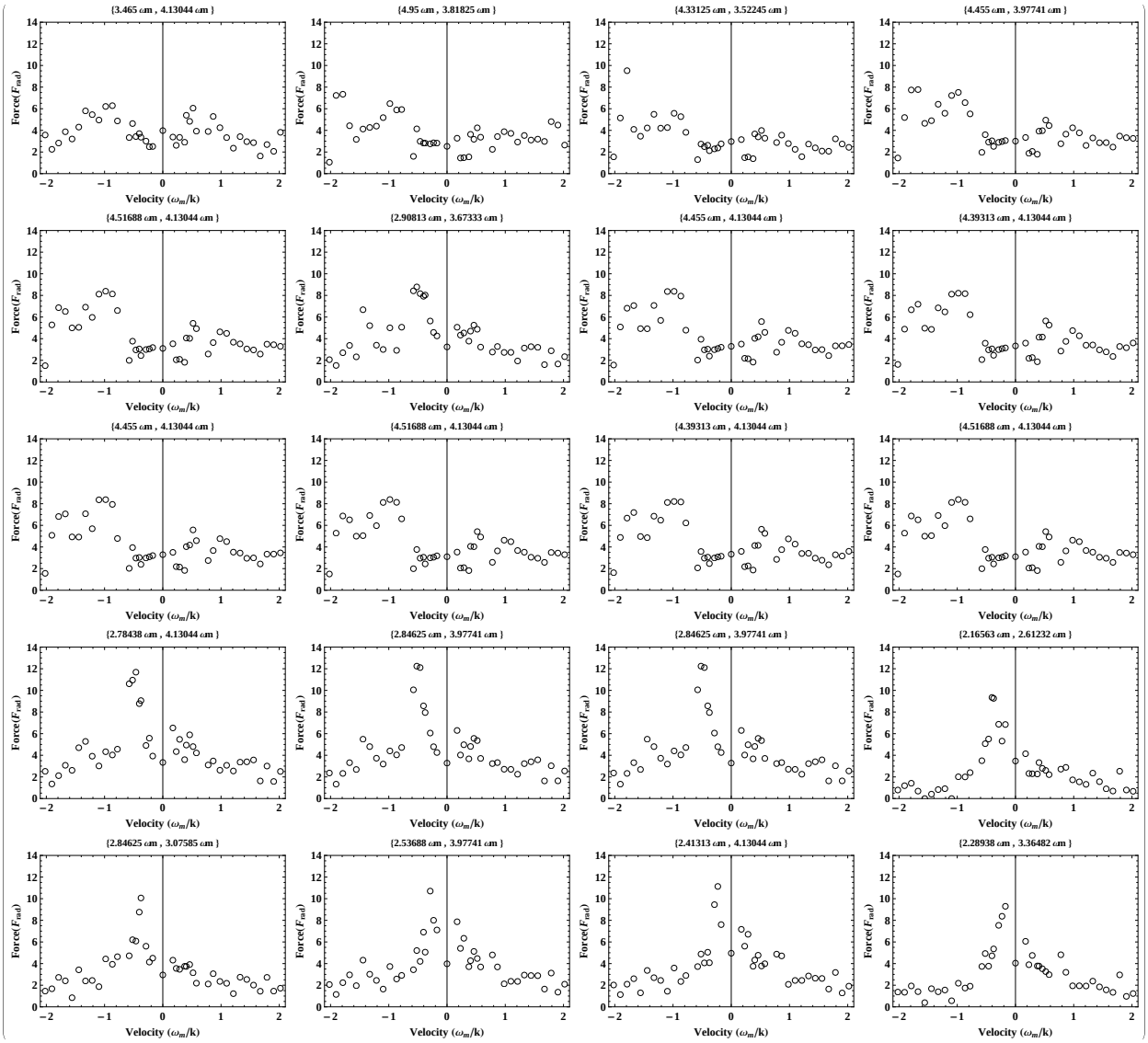

Figure B.10: Selected force *vs* velocity plots for sweep DD. Plots are labeled by $\{\delta_0, \Omega_0\}$.

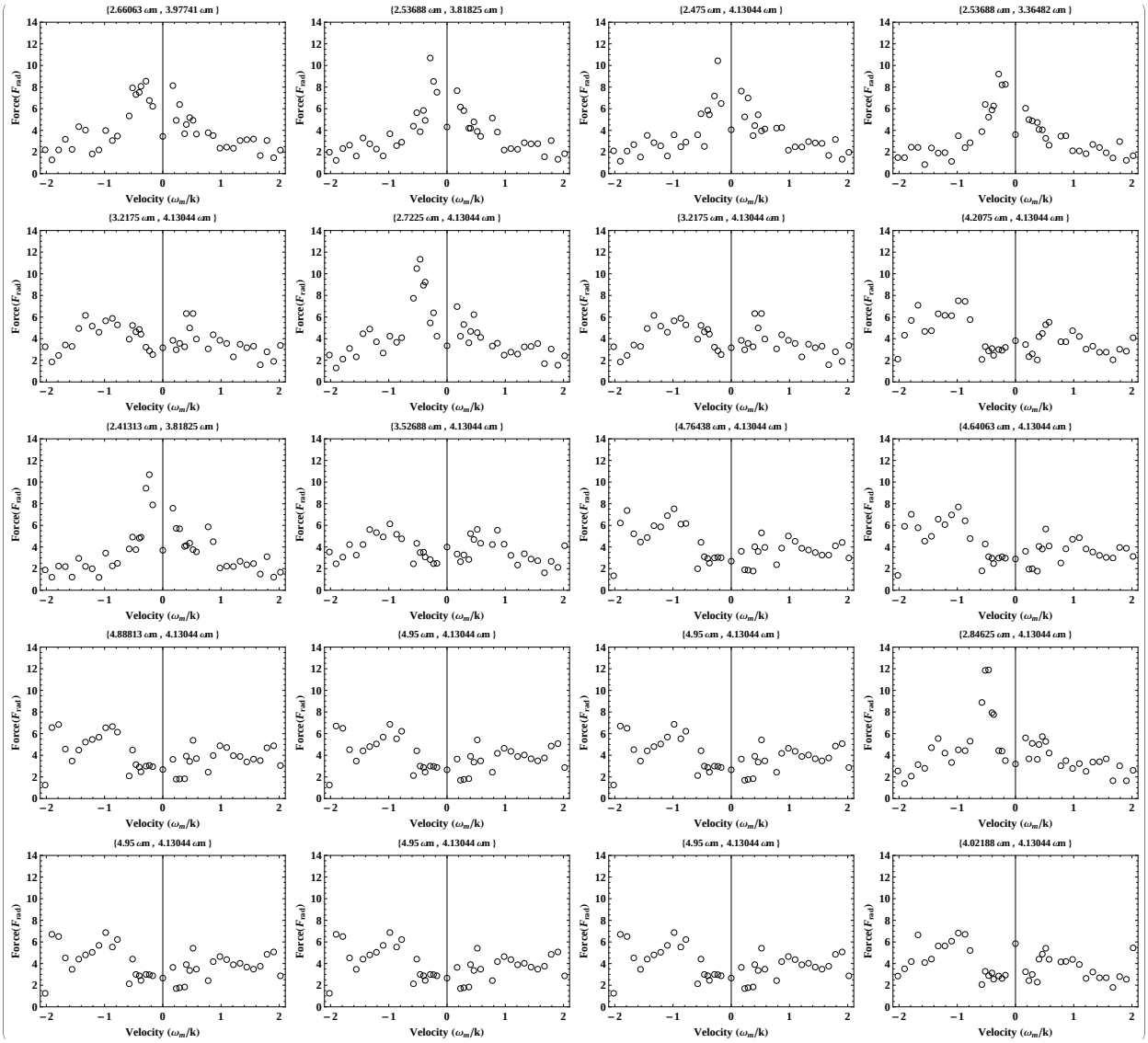

Figure B.11: Selected force *vs* velocity plots for sweep DD. Plots are labeled by $\{\delta_0, \Omega_0\}$.

B.2 Opposite Sweep Direction Velocity Dependence

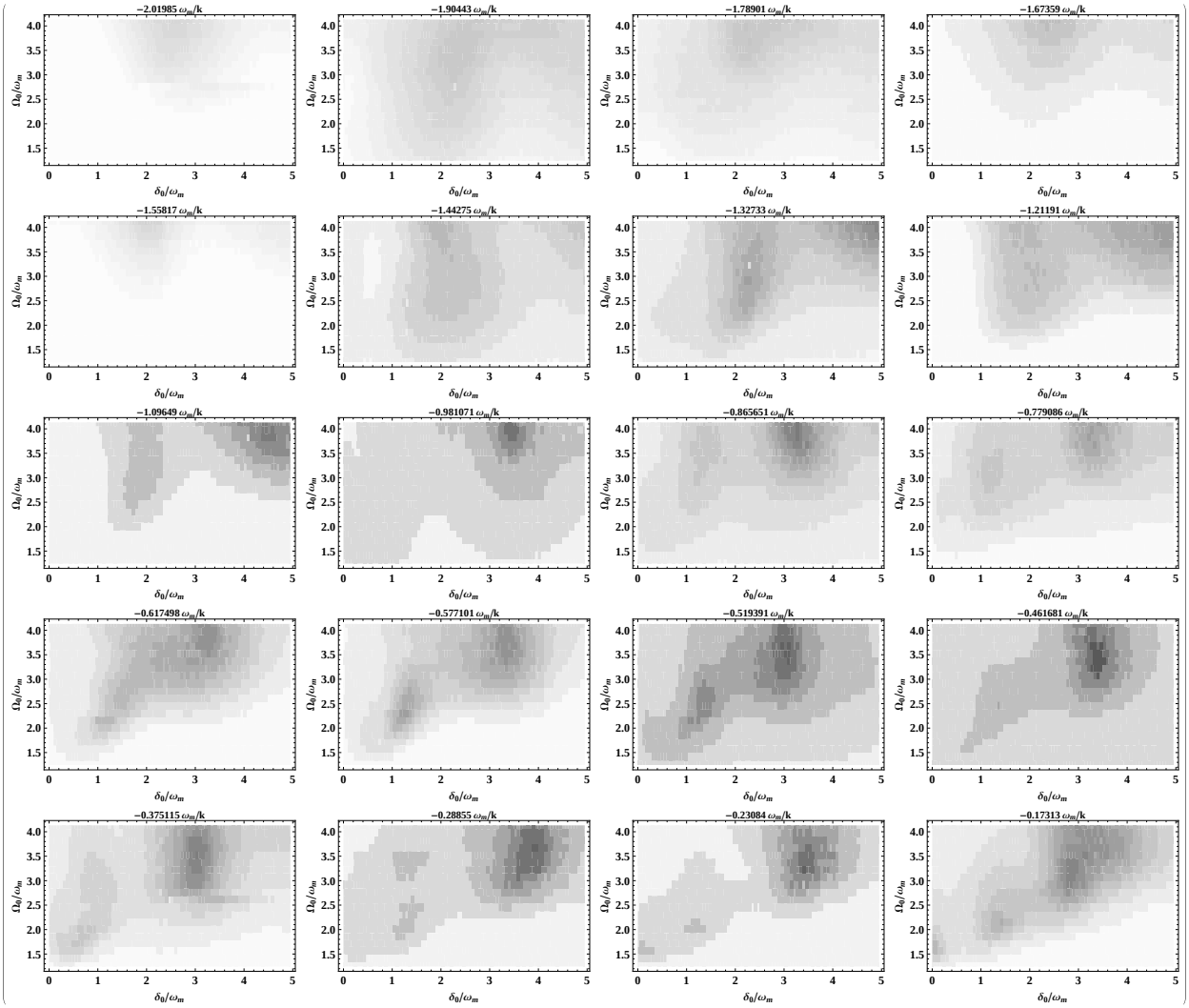

Figure B.12: Force maps for $v < 0$ and sweep directions Up-Down. Plots are labeled with the simulated atomic velocity in units of ω_m/k ($\omega_m/k \approx 170$ m/s)

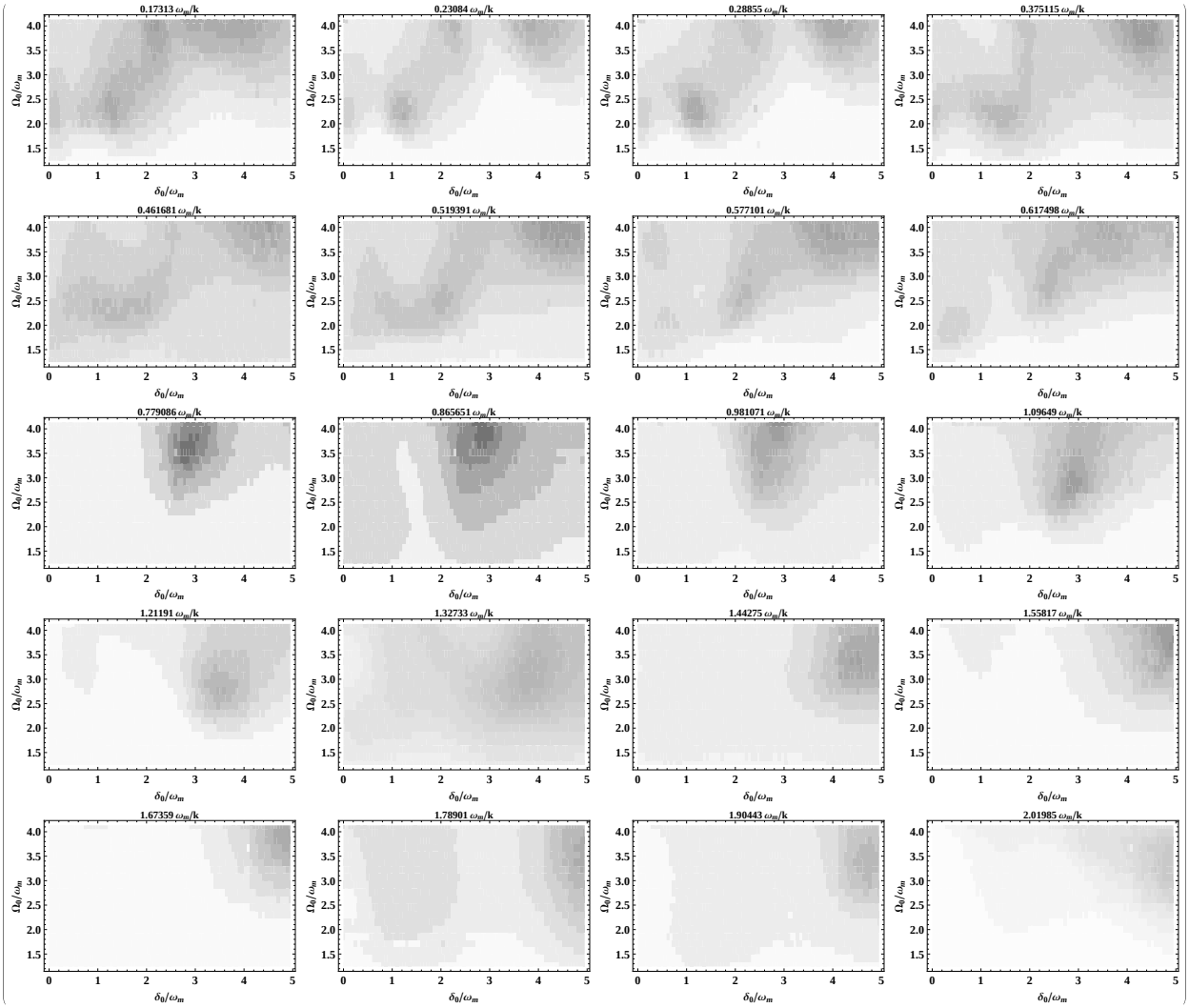

Figure B.13: Force maps for $v > 0$ and sweep directions Up-Down. Plots are labeled with the simulated atomic velocity in units of ω_m/k ($\omega_m/k \approx 170$ m/s)

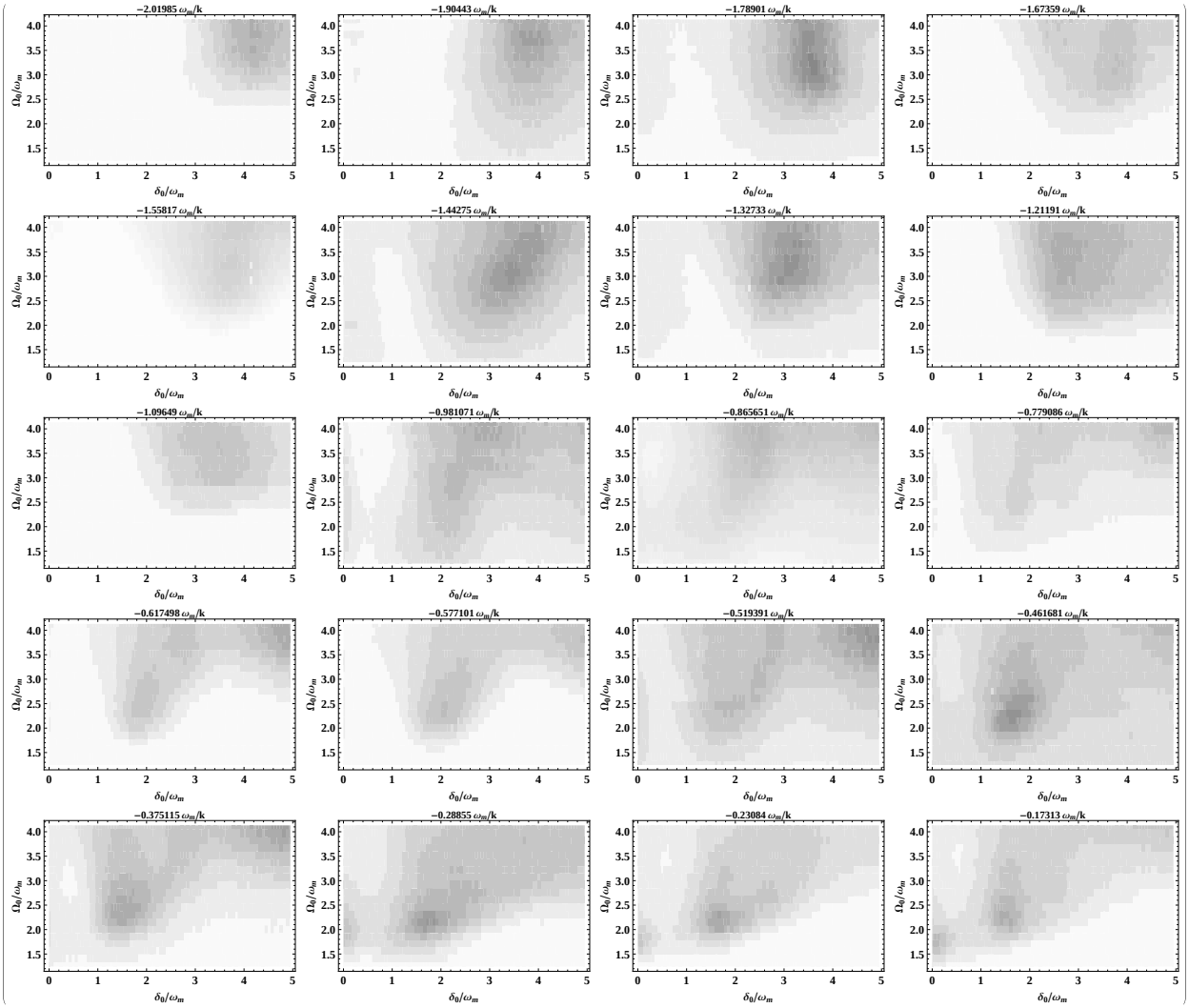

Figure B.14: Force maps for $v < 0$ and sweep directions Down-Up. Plots are labeled with the simulated atomic velocity in units of ω_m/k ($\omega_m/k \approx 170$ m/s)

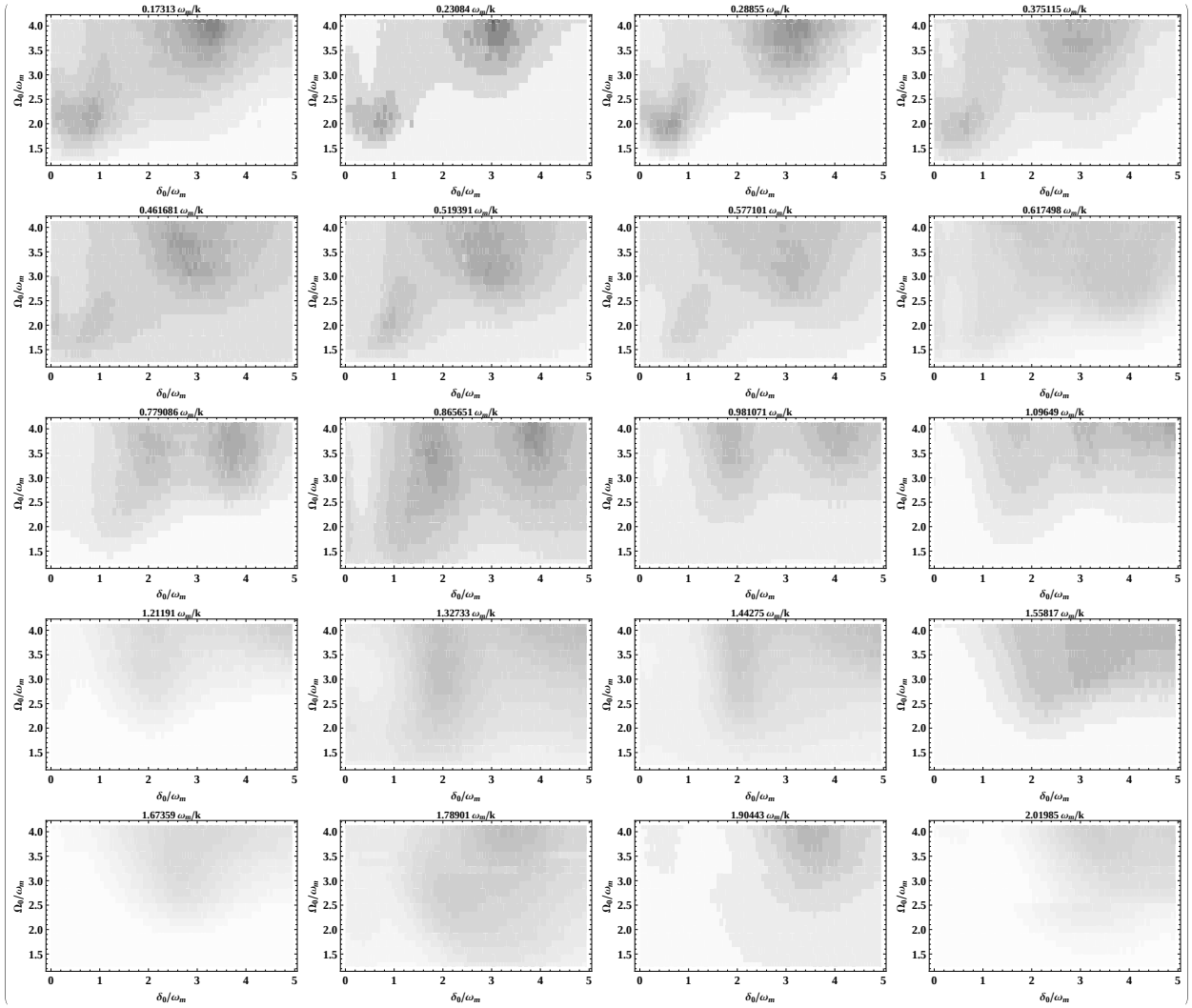

Figure B.15: Force maps for $v > 0$ and sweep directions Down-Up. Plots are labeled with the simulated atomic velocity in units of ω_m/k ($\omega_m/k \approx 170$ m/s)

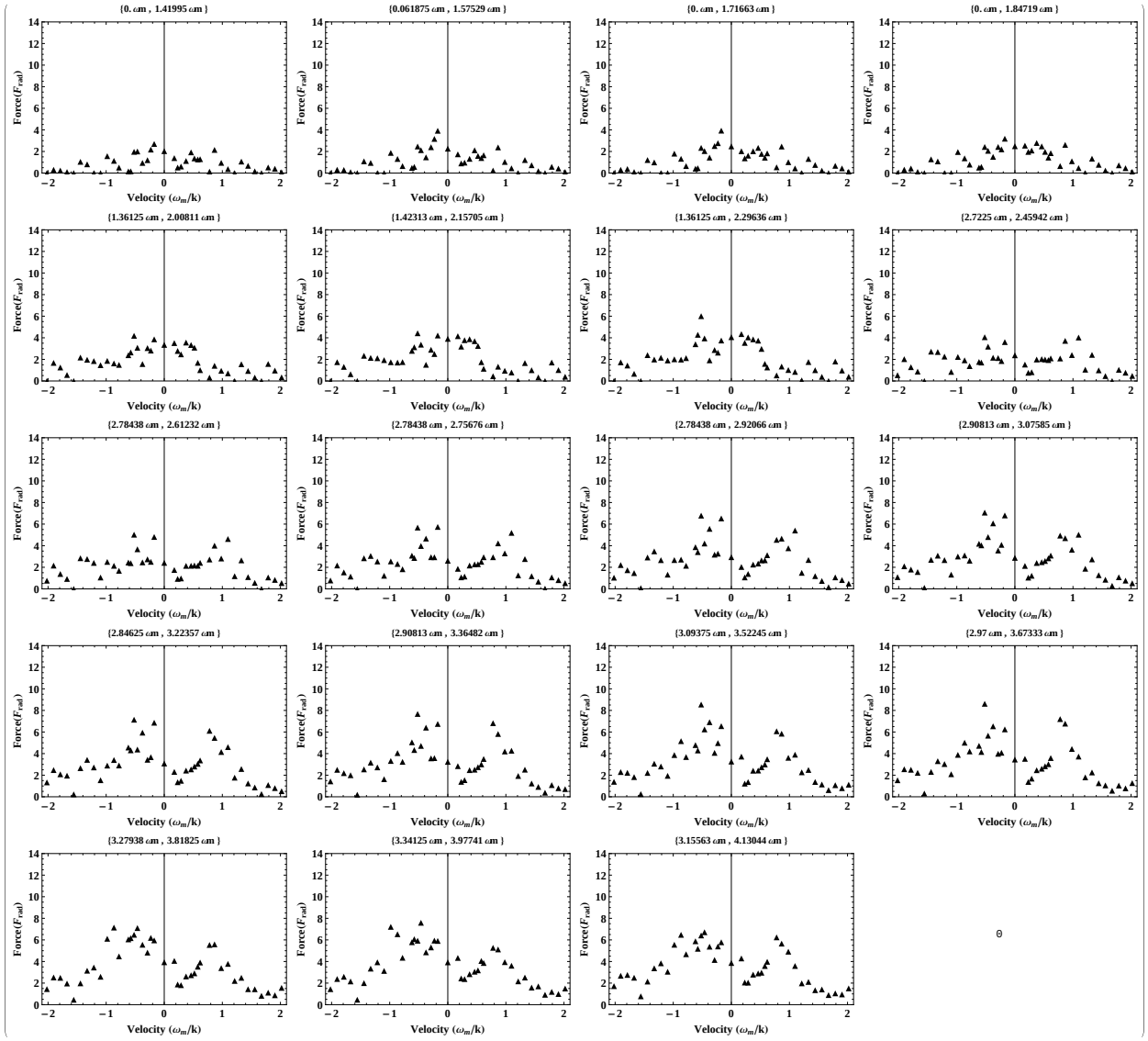

Figure B.16: Force *vs* velocity plots for sweep UD peaked near v = 0. Plots are labeled by $\{\delta_0, \Omega_0\}$.

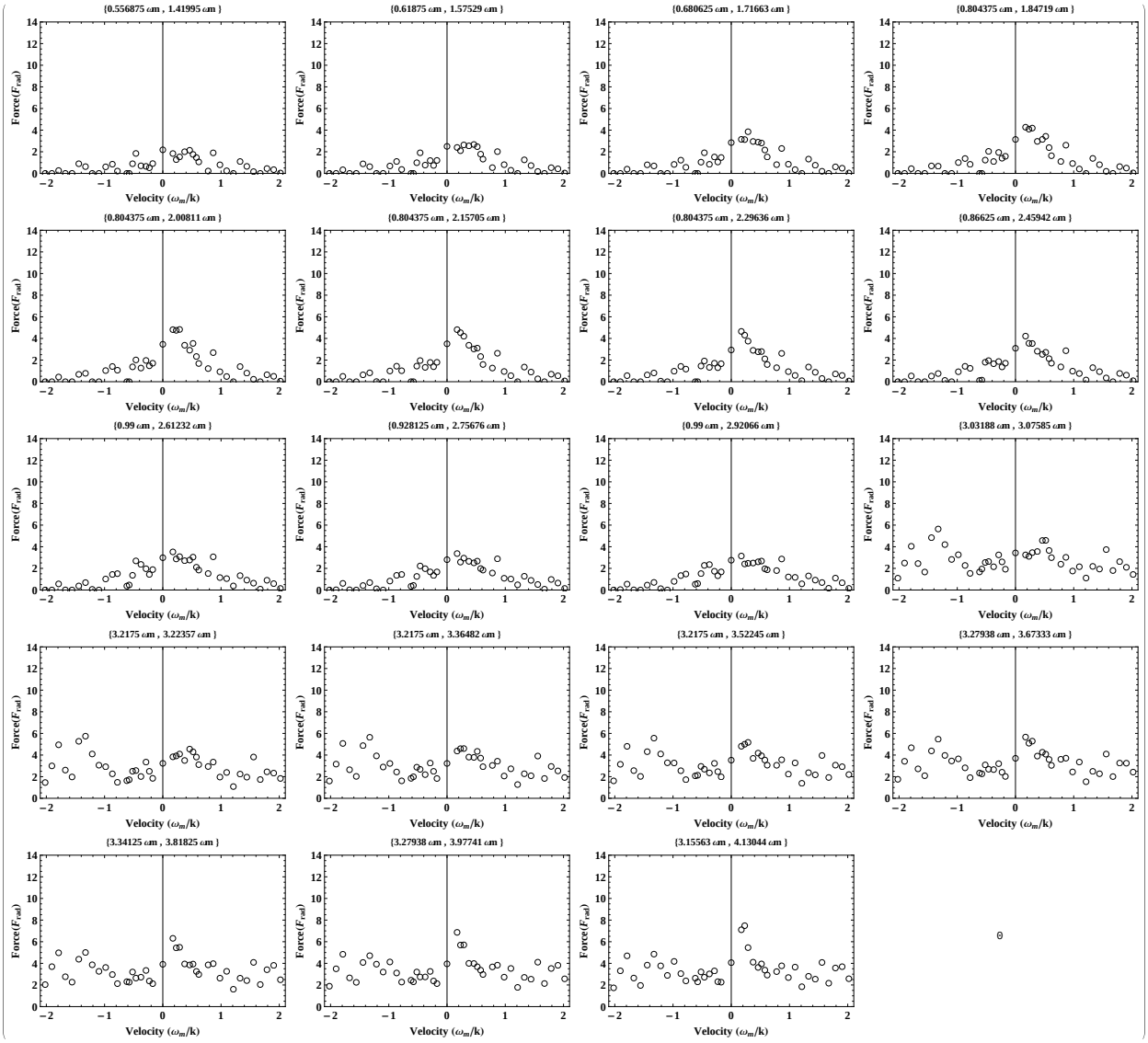

Figure B.17: Force *vs* velocity plots for sweep DU peaked near v = 0. Plots are labeled by $\{\delta_0, \Omega_0\}$.

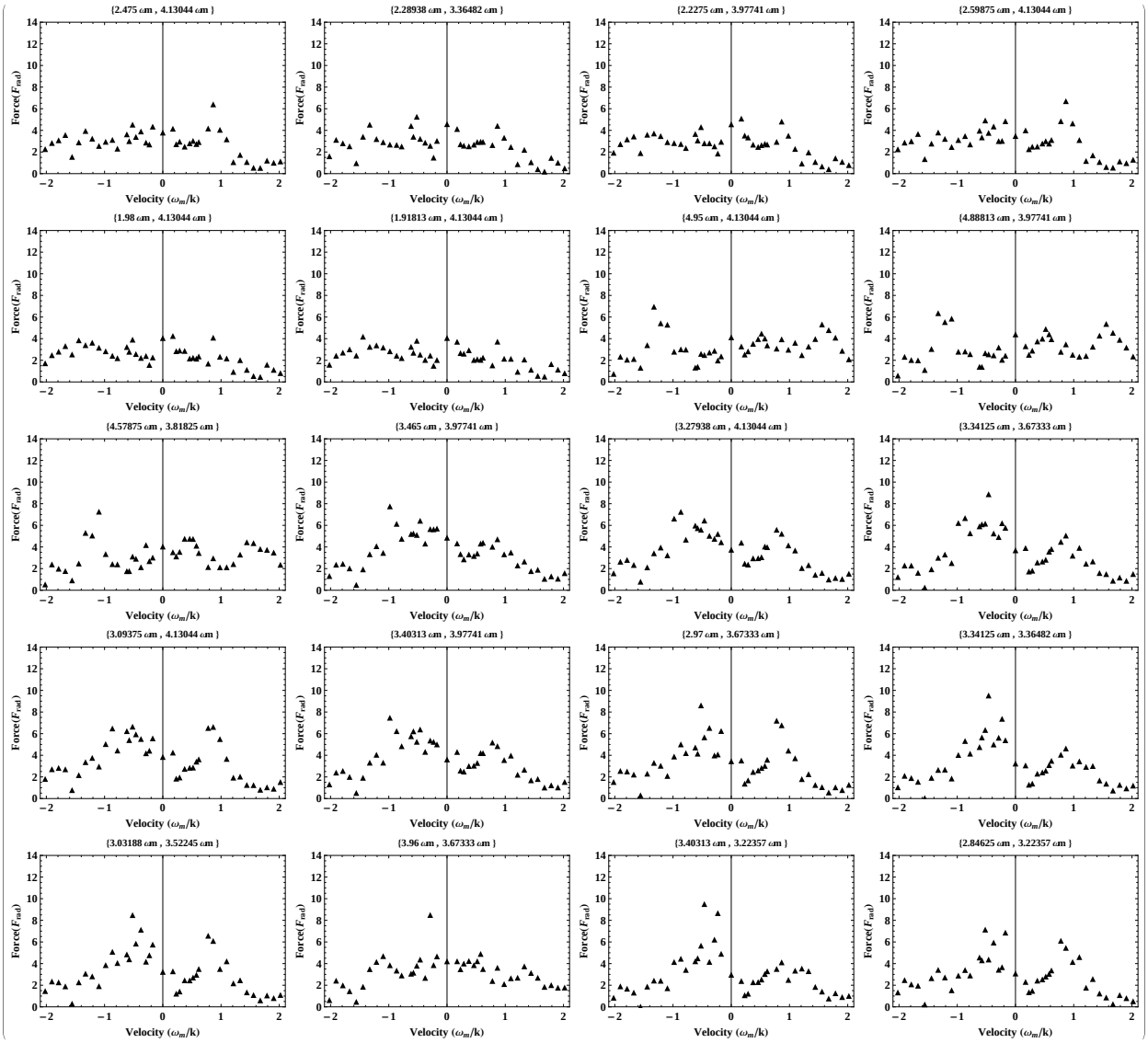

Figure B.18: Selected force *vs* velocity plots for sweep UD. Plots are labeled by $\{\delta_0, \Omega_0\}$.

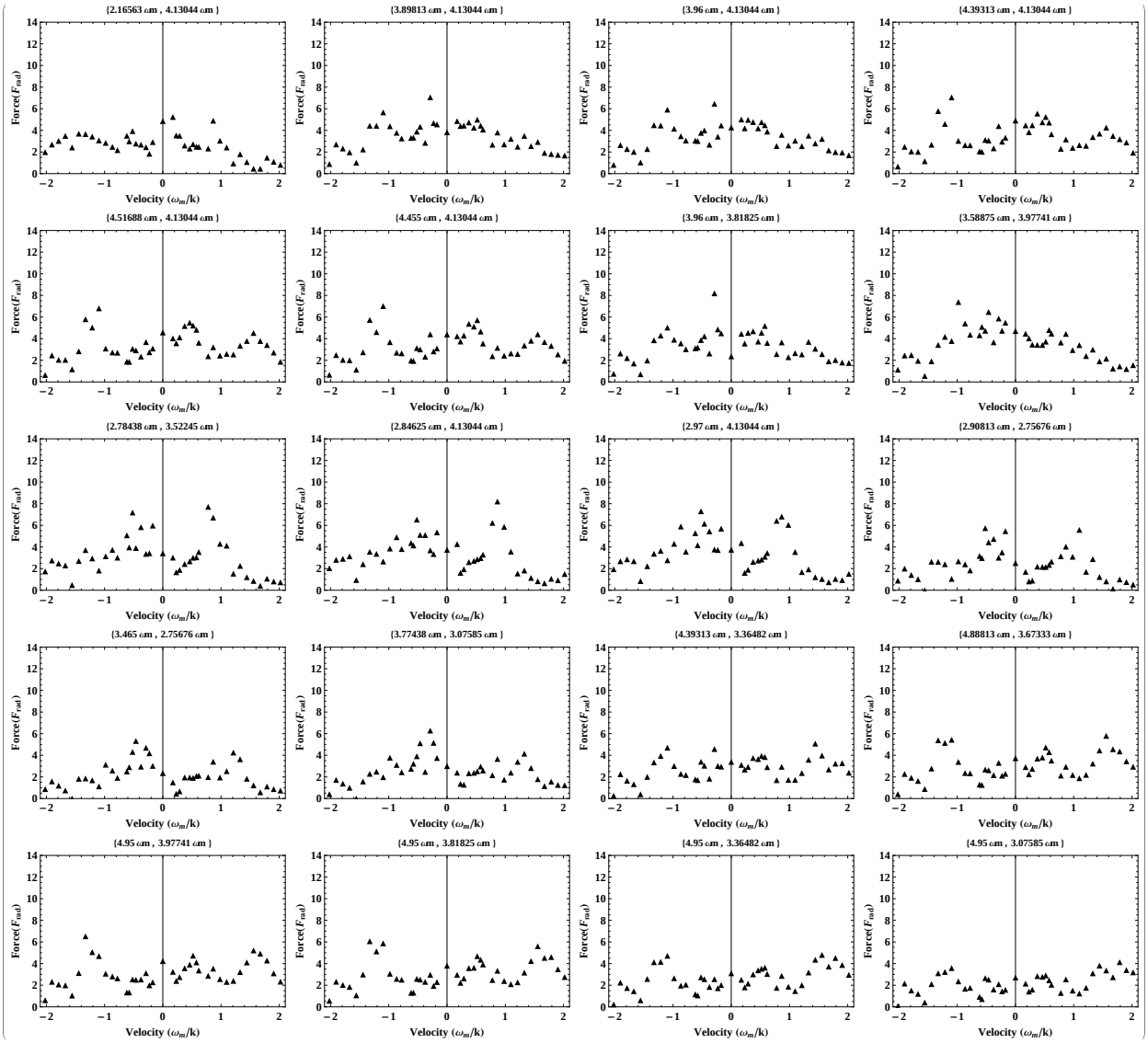

Figure B.19: Selected force *vs* velocity plots for sweep UD. Plots are labeled by $\{\delta_0, \Omega_0\}$.

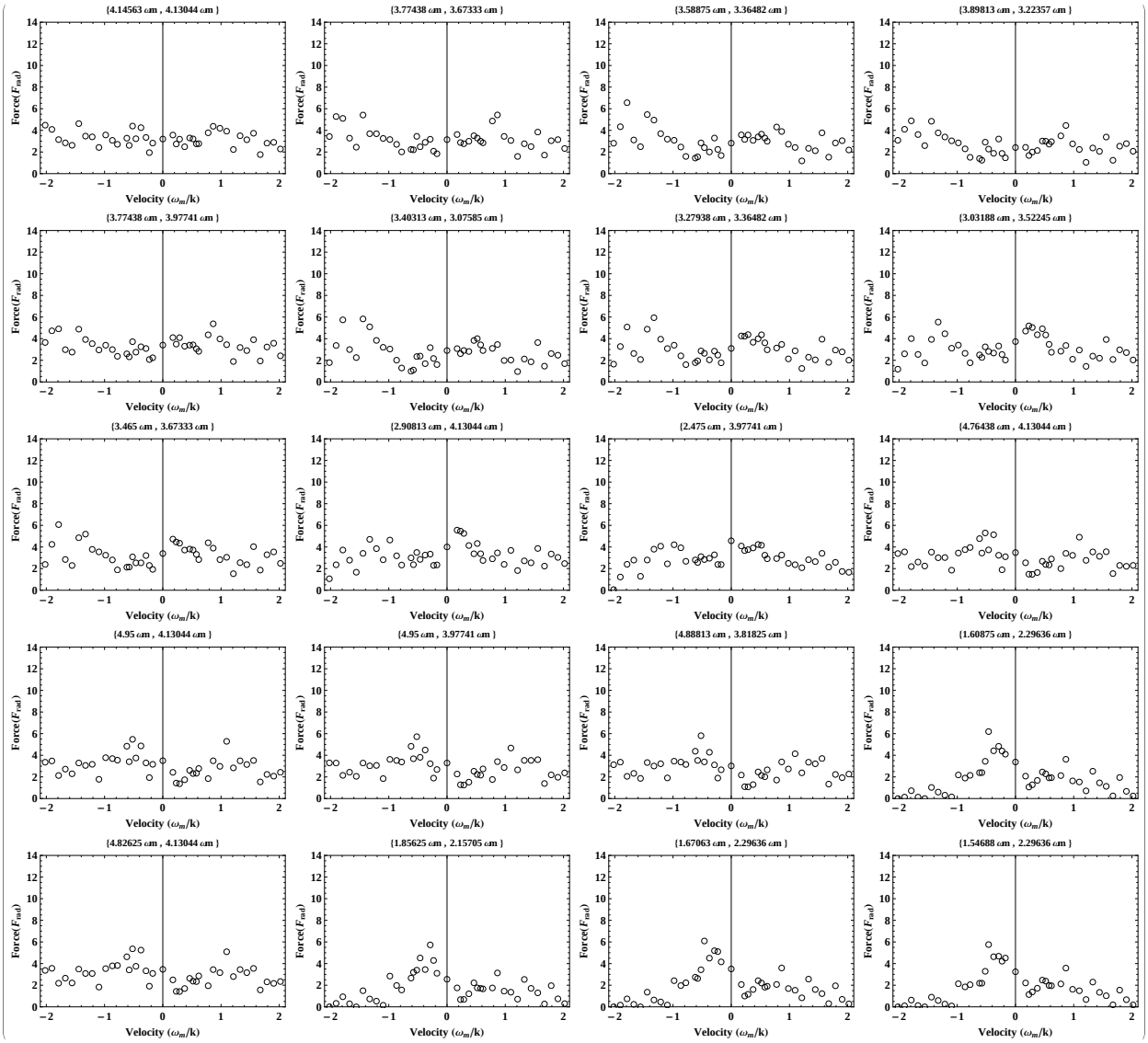

Figure B.20: Selected force *vs* velocity plots for sweep DU. Plots are labeled by $\{\delta_0, \Omega_0\}$.

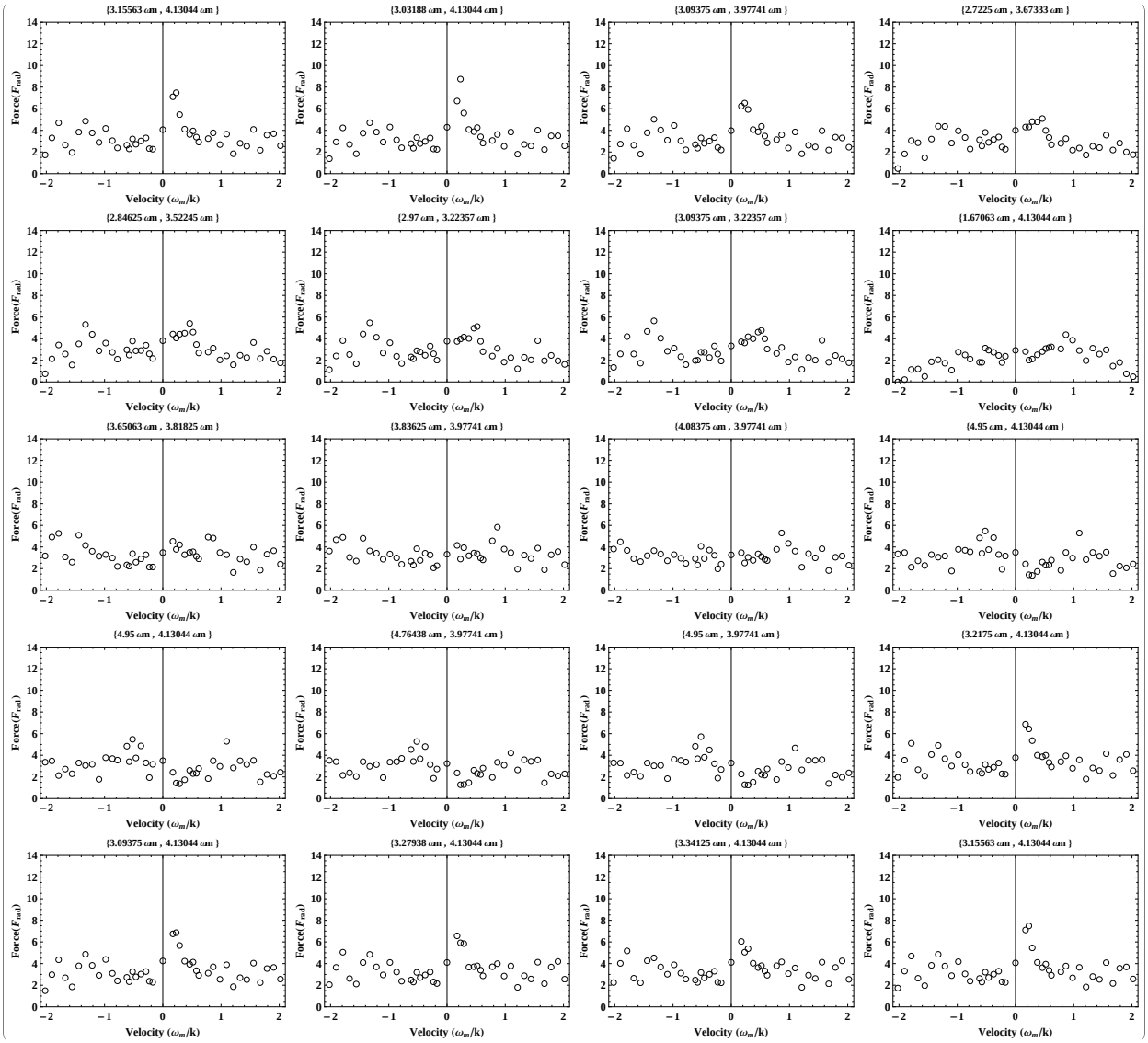

Figure B.21: Selected force *vs* velocity plots for sweep DU. Plots are labeled by $\{\delta_0, \Omega_0\}$.